University of Warwick institutional repository: http://go.warwick.ac.uk/wrap

A Thesis Submitted for the Degree of PhD at the University of Warwick

http://go.warwick.ac.uk/wrap/77689

This thesis is made available online and is protected by original copyright.

Please scroll down to view the document itself.

Please refer to the repository record for this item for information to help you to cite it. Our policy information is available from the repository home page.

Explosive condensation in symmetric mass transport models

by

Yu-Xi Chau

Thesis

Submitted to the University of Warwick

for the degree of

Doctor of Philosophy

Centre for Complexity Science and Mathematics Institute

June 2015

THE UNIVERSITY OF
WARWICK

Contents

Acknowledgments

Firstly, I would like to thank my supervisor Stefan Grosskinsky for his continuous support, gratitude and patience throughout the duration of my study. He has always been a great teacher, and his intellect, enthusiasm, warmth and humour will be missed. His door is always open, and I really enjoyed many of our conversations.

I would also like thank my second supervisor Colm Connaughton, who has always been encouraging, welcoming and friendly. My supervisors make my time in the Complexity DTC very pleasurable and memorable. I owe a lot to the Complexity DTC, for their understanding and help throughout my PhD studies, especially Prof. Robert MacKay and Prof. Robin Ball. And to Complexity DTC administrators Monica de Lucena, Phil Richardson, Jen Bowskill, Heather Robson and Deborah Walker for their assistance and resourcefulness. I am also very grateful for my fellow students in the DTC, having always been supportive at an intellectual level. I would like to thank especially Anas Rana, Dominic Kerr, Anthony Woolcock, Mike Maitland and Arran Tamsett for the countless discussions we have had over the years.

My time in graduate school has been a time of great emotional and spiritual journey, and I would thank all my friends for their support outside my studies. Especially my mentors Elaine Tang and Chernise Neo for their invitations and challenges. Martine Barons and Phil Richardson for their spiritual guidance inside the Complexity DTC. Also members of the Westwood Church, especially Peter Findley, Pinmei Huang, Caroline Howarth and Oliver Howarth, for the community, conversations and good food.

Finally, I would like to thank my family, especially my parents and brother for their constant support. Also, I am forever in debt to Helen Miu for her patience and looking after me so amiably from almost 6,000 miles away.

Declarations

This work has been composed by myself and has not been submitted to other degree or professional qualification.

- The novel and original contributions of this thesis are presented in Chapters 4 to 6.
- Results in Chapter 4 are published [1] in November 2015.

Abstract

Condensation is an emergent phenomenon in complex systems that is observed in both physical and social sciences, from granular polydisperse spheres to macroeconomic studies. The critical behaviour of condensation in such systems is of continual interest in research. In this thesis we study this in the context of interacting particle systems, in particular the recently introduced explosive condensation process.

We firstly provide a review of the mathematical foundations of interacting particle systems from the aspects of Markov processes. This includes the formulation of factorised hop rates, stationary product measures, the equivalence of ensembles and how these properties are related to condensation. Subsequently, we give a review of key interacting particle systems of interest, namely the zero-range process, inclusion process and the explosive condensation process. We then introduce two models that have similar stationary weights scaling as the explosive condensation process and include them in our study in the thermodynamic limit.

The density and the maximum site occupation are derived under the stationary distribution, and from this we are able to identify the choice of parameters that could lead to a phase transition. Exact results for these models using the generator are difficult to obtain. For the main results of this study, we therefore analyse the formation of condensate using a heuristic approach. The microscopic interactions leading to the formation of an explosive condensate are structurally studied, and this leads to a comprehensive model with a timescale analysis. The time to condensation is shown to vanish as the thermodynamic limit is reached, depending on the choice of parameter values.

Throughout the thesis, theoretical results are supported by Monte Carlo simulation and numerical calculations where appropriate. A modification of the conventional Gillespie algorithm is proposed. The new algorithm improves efficiencies but is also able to preserve key stochastic properties, and is used throughout the simulation of the main findings.

Notation

Below are some important notations used throughout the thesis, listed in chronological order of introduction:

Λ	Countable lattice (p. 5)
X_Λ	State space $X_\Lambda = \mathbb{N}^\Lambda$ (p. 5)
L	Size of countable lattice (p. 5)
$\eta = (\eta_x)_{x \in \Lambda_L}$	Full configuration (p. 5)
η_x	(p. 5)
N	Total number of particles in system, i.e. $\sum_{x \in \Lambda} \eta_x = N$ (p. 5)
$c(\eta, \eta')$	Transition rate from configuration η to η' (p. 5)
η^{xy}	New configuration after a particle is moved from site $x \to y$ in η (p. 5)
$\mathcal{L}$	Generator (p. 6)
$f(\eta)$	An observable over configuration η (p. 6)
$\mathbb{R}$	Real numbers (p. 6)
$\mathbb{E}$	Expected value of (p. 6)
x, y	Typical lattice sites (p. 6)
$p(x, y)$	Adjacency matrix (p. 7)
$u(n), v(n)$	Factorised hop rates of transition rate (p. 7)
ϕ	System fugacity (p. 8)
z	Partition function (p. 8)

W	Stationary weights (p. 8)
$R(\phi)$	Average number of particles per site (p. 8)
σ^2	Second moment of the system (p. 9)
k_∞	The ∞ denotes k in long relaxation times, or $t \rightarrow \infty$ (p. 9)
ρ_c	Critical density (p. 10)
d	Diffusive parameter (p. 17)
T_{SS}	Time for the system to reach stationarity (p. 20)
$\eta_{\max}$	Occupancy of the highest occupied site in the system (p. 28)
$G(L, S_c)$	Denoting the Erdős-Rẽnyi graph, where $S_c = (1/L \sum_{x,y\in\Lambda} p(x,y)$ (p. 34)
$c(\eta_x, \eta_y)$	Another form for transition rates, which depends on the local configuration η_x, η_y (p. 46)
m_c	Critical occupancy number (p. 49)
τ_{step}	Time for an entire cluster to move one lattice space (p. 53)
$v(m) = 1/\langle\tau_{\mathrm{step}}\rangle$	Average velocity for an entire cluster to move one lattice space (p. 54)
Δm	The transfer of mass from the smaller to the larger cluster when two clusters collide (p. 58)
p_{split}	Probability of a cluster to spontaneously split up into two separate clusters in opposed to moving to a neighbouring site. (p. 87)
$r_{\mathrm{split}} = v(m)p_{\mathrm{split}}$	The rate of a split (p. 88)
N_{br}	Total number of clusters breaking up in the timescale when a system reaches stationarity (p. 89)
Ω	Total number of steps for a system to reach stationarity (p. 94)

Below are suffixes used throughout the thesis, that is related to either the graph, model or a process:

$\square_{\mathrm{Wa}}$	relating to the model with rates (3.2)
$\square_{\mathrm{mod}}$	relating to the "modified" model with rates (3.3)
$\square_{\mathrm{gen}}$	relating to the "generalised" model with rates (6.1)
$\square_{\mathrm{sym}}$	relating to cases on a symmetric graph
$\square_{\mathrm{asym}}$	relating to cases on a totally asymmetric graph
$\square_{\mathrm{Nu}}$	relating to the cluster nucleation phase
$\square_{\mathrm{Co}}$	relating to the cluster coarsening phase

Chapter 1

Introduction

Statistical mechanics provides a qualitative connection between macroscopic physical laws and microscopic rules of interactions for large physical systems using statistical methods. The origin of statistical mechanics is in thermodynamics, where a class of continuous physical measures can be explained by atomic interactions using probabilistic arguments. Extremely large system sizes of the order of 10^{23} particles lead to very small fluctuations around the typical behaviour, which can be derived in a thermodynamic scaling limit. Since its early development, statistical mechanics has become a convenient mathematical tool that is used for systems with a large number of interacting components, not constrained to physical models only. Examples include traffic flow, economics, crowd dynamics, etc. In theory, a microscopic description of such systems is deterministic, but impractical due the number of degrees of freedom. Due to the robustness of the system on a macroscopic scale with respect to noise, it is often sufficient to approximate the microscopic behaviour in terms of randomness with a postulated probability distribution.

With a probabilistic description, the system is characterised by the expected values of certain observables, which correspond to the microscopic state space measurable functions. For systems in equilibrium in the thermodynamic limit, where the size is very large, these observables can be calculated by a small number of macroscopic system parameters, such as density, temperature and pressure. One area that is particularly studied is the ability of the system to exhibit phase transitions, where qualitative changes in the typical behaviour of observables occur when some parameters are varied. In such cases, abrupt transitions of some macroscopic observables can be observed.

For systems with many identical components which are in equilibrium with the surroundings, the stationary long-time behaviour is described by an energy function or the Hamiltonian. In this scenario the typical value of macroscopic observables is given by the expected values under the relevant stationary measure. Such systems have been extensively studied in the physical literature, since the work of Boltzmann, and there is now a well developed mathematical theory [2, 3]. There is also a well developed mathematical understanding of phase transitions in such systems in terms of Gibbs measures [4].

Although there are few general physical laws that apply to non-equilibrium systems, insights can be drawn by studying interacting particle systems. They consists of particles on a lattice, where the exchange of particles between sites is given by rates that depend on the system configuration. Mathematically they can be regarded as continuous-time Markov process on a discrete state space. The rules of interactions can be altered to represent any microscopic phenomena of interest. These models have been popular in various fields, such as physics, chemistry, biology, social sciences, etc. The underlying process may be defined in terms of discrete particles on some lattice, for example cellular growth of cells on a 2-dimensional surface. Naturally, a phenomenological description is used to describe these interacting particle models, in the sense that they serve as an approximation to their true underlying microscopic dynamics. Therefore, interacting particle systems may be regarded as mesoscopic models. These models are popular in physics and mathematics because of their broad application and rich non-trivial characteristics despite their simplistic set-up.

A particularly well studied model encompassing these characteristics is the zero-range process, which is used to explain physical systems such as polydisperse spheres, quantum gravity and traffic jams [5]. There is no restriction on the number of particles on each site, and the transition rate is dependent on the occupancy of the departure site only. Despite its seemingly simple set-up, it displays non-trivial behaviour even in a one-dimensional geometry. A natural progression from the zero-range model is models with transition rates that depend on the occupancies of both the departure and receiving sites. These give rise to increasing research interest for new models such as the inclusion process, and more recently, the explosive condensation process [6]. Condensation occurs when a positive fraction of the mass of the system is concentrated on one lattice site. This can occur for both inhomogeneous and homogeneous graphs. We are particularly interested in the homogeneous cases of explosive condensation in this study, and we focus on the cases where the overall mass of the system is a conserved quantity. Explosive condensation is a phenomena observed in some condensation models, where the time to reach the condensate goes to zero as the system size L diverges. This is seemingly counter-intuitive as it implies that stationarity is reached instantly if the system size is infinitely large.

To clarify the ideas mentioned above, we describe a social science analogy of phase transition in condensation as an example, with one that concerns the trading of wealth in an agrarian society. Land is the primary source of wealth in agricultural societies, and is usually conserved. Therefore wealth is largely conserved over long timescales in ancient societies. Agents are able to exchange wealth as part of the normal economic activity, where interactions are biased under the frameworks of information economics. This rule of exchange is embedded in a global redistribution of wealth in the form of poll tax. A defining feature is when systems transit from a relatively equal distribution to a phase of great wealth disparities. It is observed as a historical phenomenon that great wealth disparity is always the stationary state for relatively prosperous closed societies. Primitive societies are known to exist for centuries with a largely intact "fluid state" of wealth. At some critical density, when overall wealth in the society increases, huge wealth disparities would be observed. The Matthew principle states that the greater wealth in the system, the faster the speed of wealth condensation [7, 8]. In this situation, wealth is divided between a ubiquitous fluid state and a condensate.

In Chapter 2 we summarise the results from existing literature on interacting particle systems, introducing the concepts of generators and stationary product measures. Several models are reviewed to discuss recent areas of research interest. Models that are similar to the explosive condensation model are introduced in Chapter 3 and we attempt to retrieve meaningful results from the generator. In Chapter 4, we study the dynamics of models introduced in the previous Chapter heuristically in the thermodynamic limit. This gives rise to a comprehensive explanation of the formation of the explosive condensate, where distinctive stages of cluster interactions are studied. The nucleation and coarsening driven model in Chapter 4 also leads to a simpler explanation for previous studies [6]. In Chapter 5, we discuss numerical methods for this study. An algorithm that improves numerical efficiency yet preserving stochastic properties is introduced. Two variants of the model studied in Chapter 4 are introduced in Chapter 6, which extend this study to inhomogeneous graphs and extreme range of certain parameters. The main novel contributions of this thesis are presented in Chapter 4 with extensions in Chapters 5 and 6.

Chapter 2

Interacting Particle Systems

2.1 Introduction

Interacting particle systems (IPS) were originally studied as a branch of probability theory [9, 10], but have since grown and developed rapidly, establishing connections with applications in physics, biology and social sciences [5]. The original motivation for IPS came from statistical mechanics. The objective was to describe and analyse stochastic models for the temporal evolution of systems with classical Gibbs states as their equilibrium measures [11] [12]. In particular, it was hoped that the study of IPS would lead to a better understanding of the phenomenon of phase transitions.

Through the works of Liggett [13] and Dobrushin [11], foundations of IPS were studied in the early 1970s. The introduction of IPS is a natural extension of the established theory of Markov processes. A typical set-up of IPS consists of having a finite or infinite number of particles on a lattice, with some interaction rules outlining how particles are transferred between sites. The interaction between particles implies that the system is more complex than simple independent particles, and has to be described on a very high dimensional state space.

Interacting particle systems have since developed and became an independent study area that connects the mathematical description of different physical systems; such as neural networks [14], tumour growth [15], spread of infection [16], wealth distribution models [17], traffic jams [18, 19] population ecology [20], behavioural systems [21, 22] and many others. This involves using different types of transition rates on different graphs. A review of models relevant to this thesis can be found in Sec. 2.3. Even though the set up is generally simple, a rich complex behaviour can be seen already in one-dimensional systems.

In this chapter, the ideas for the foundations of IPS are described and a brief discussion of its mathematical foundations is outlined and organized as follows: definitions provided in this chapter in Sec. 2.2 will be used throughout this thesis. A standard formulation of an IPS using the generator, definition of transition rates as factorized hop rates are introduced in Sec. 2.2.1 - 2.2.3. Selected models that have attracted recent research attention are summarised in Sec. 2.3. These include the classic zero-range process and the more recently introduced inclusion process and explosive condensation process.

2.2 Definitions

A detailed description of the notation and definitions used throughout this study are provided in this section. The notation used in this work are largely taken from Chleboun and Grosskinsky [23], Grosskinsky, Schütz and Spohn [24] and also more distantly from Liggett [13].

Essentially, interacting particle systems are a class of continuous-time Markov processes on discrete state spaces with states given by particle configurations on a lattice or general graph. Systems with both infinite and finite lattice sizes are possible, but this study focuses on closed finite systems and their scaling behaviour. The dynamics of these processes are typically characterized by infinitesimal transition rates at which transitions between states occur.

The state space $X_\Lambda = \mathbb{N}^\Lambda$ contains all possible particle configurations, where Λ denotes a countable lattice that can be finite or infinitely large. As this study focuses on finite systems, usually $\Lambda_L = \{1, 2, ..., L\}$ is finite and L denotes its finite size. In this study, we restrict the lattice to being one-dimensional. The configuration of the system is given by $\eta = (\eta_x)_{x\in\Lambda}$, such that $\eta_x \in \mathbb{N}$ denotes the number of particles at site x . The total number of particles on a finite system is therefore $N = \sum_{x\in\Lambda} \eta_x$.

We focus on local jumps, where a single particle changes location, and denote by η^{xy} the resulting configuration after a jump from x to $y \in \Lambda$, where

$$\eta_z^{xy} := \eta_z - \delta_{z,x} + \delta_{z,y} \ , \tag{2.1}$$

and δ is the Kronecker delta function and all $x, y, z \in X$. Site x can be regarded as the departure site and site y is the receiving site. Note that such transitions only occur if site x has non-zero mass prior to an interaction.

The interaction of the particle system is characterized by transition rates $c(\eta, \eta')$ for the transition from one configuration to another. These infinitesimal transition rates are used to define the generator of the process (see Sec. 2.2.1), which uniquely characterises the time evolution using Markov semigroups and the Hille-Yosida theorem. In the following we give a short account of these tools, and for a rigorous mathematical formulation of these tools see Chapters I and II of [10].

2.2.1 Generator

The transition rate of a system is given by $c(\eta, \eta') \geq 0$ which, for all $\eta, \eta' \in X$, describes the rate at which the system changes from the current state η to a new state η'. The generator $\mathcal{L}$ operating on a general observable $f : X_\Lambda \to \mathbb{R}$ is defined as

$$\mathcal{L}f(\eta) = \sum_{\eta' \in X} c(\eta, \eta')(f(\eta') - f(\eta)) , \tag{2.2}$$

with the convention $c(\eta, \eta) = 0$ for all $\eta \in X$. The observable $f(\eta)$ can be any physical property derived from the configuration, such as the average number of particles, the second moment of the configuration, etc. The dynamics on a finite lattice Λ_L are defined by the generator, in the sense that

$$\frac{d}{dt}\mathbb{E}[f(\eta)] = \mathbb{E}[\mathcal{L}f(\eta)]. \tag{2.3}$$

This becomes a very convenient tool for studying Interacting Particle Systems, where the time evolution of any observable of interest can be expressed as a differential equation. This form is equivalent to the description of the master equation for the IPS. Denoting the probability distribution on X_Λ at time t by $\overline{p}_t[\eta]$, the master equation is given by

$$\frac{d}{dt}\overline{p}_t[\eta] = \sum_{\eta \in X} (\overline{p}_t[\eta] c(\eta, \eta') - \overline{p}_t[\eta'] c(\eta', \eta)) , \tag{2.4}$$

which displays gain and loss terms on the right-hand side and follows from Eq. (2.3) by using the indicator function $f = \delta_\eta$. However, it is convenient to use the generator because its set up allows us to write down a time-dependent relationship for any designated set of observables, rather than the general distribution of the configuration. Note that the process is derived from the generator by constructing a Markov semigroup and closing it using the Hille-Yosida theorem, for which the rigorous mathematical formulation can be found in Chapters I and II of [10].

2.2.2 Factorized hop rate

From this point onwards, we deviate from the general IPS set-up and focus on a set of formulation of the model that has attracted great research attention for the past years (see e.g. [23] and references therein). For pairwise interactions, the most common form for interacting particle systems is when the rates of interaction are dependent on the mass of the departing site x and the receiving site y . We introduce the factorized hop rates, which for this type of interactions are written as a factorized form

$$c(\eta, \eta^{xy}) = u(\eta_x)v(\eta_y)p(x, y) \,, \tag{2.5}$$

where $u(\eta_x)$ and $v(\eta_y)$ represent the independent contributions from the occupancies of the departure and receiving sites, respectively. $p(x, y)$ is the adjacency matrix depicting the connectivity on the graph Λ. The factorized hop rates must satisfy

$$\begin{aligned} u(n) &= 0 \qquad \text{if and only if } n = 0, \\ v(n) &> 0 \qquad \text{for all } n \geq 0 \,. \end{aligned} \tag{2.6}$$

The reason why factorized hop rates attracted so much interest in interacting particle systems research is because of its simplicity and the rich behaviour it demonstrates. It has also been established that systems with factorized hop rates have stationary product measures, as outlined in the following sections.

The adjacency matrix is given by the transition rates of a single random walker on Λ where $p(x, y) \geq 0$ and $p(x, x) = 0$. Note that only irreducible cases are studied to avoid hidden conservation laws in this thesis. Throughout this thesis, we focus on two specific cases of the adjacency matrix in the literature, namely the totally asymmetric graph and the symmetric graph in one dimension. For the totally asymmetric graph,

$$p(x, y) = \begin{cases} 1 \,, & \text{for } y = x + 1 \\ 0 \,, & \text{otherwise} \,, \end{cases} \tag{2.7}$$

and for the nearest neighbour symmetric graph,

$$p(x, y) = \begin{cases} 1 \,, & \text{for } |x - y| = 1 \\ 0 \,, & \text{otherwise} \,. \end{cases} \tag{2.8}$$

The generator in (2.2) is now rewritten as

$$\mathcal{L}f(\eta) = \sum_{x,y\in\Lambda} p(x, y)u(\eta_x)v(\eta_y)(f(\eta^{xy}) - f(\eta)) \,, \tag{2.9}$$

which is its full form. Under this specific framework of interacting particle systems listed above, several examples are reviewed later in this chapter and they are

- zero-range process (ZRP): $u(n)$ arbitrary, $v(n) = 1$ (see Sec. 2.3.1, with a brief discussion for its mapping onto the exclusion process),
- inclusion process (IP): $u(n) = n$, $v(n) = d + n$, $d > 0$ (see Sec. 2.3.2), and

- explosive condensation process (ECP): $u(n) = v(n) - v(0)$, where $v(n) = (d+n)^\gamma$, and $d, \gamma > 0$ (see Sec. 2.3.3).

Note that the interaction of particles are characterized by the above generator. Focusing on the scaling properties of finite systems in the thermodynamic limit, N is the total number of particles in this system, when for $L \to \infty$ and $N \to \infty$, the density $\rho = N/L$ is fixed.

2.2.3 Stationary Product Measure and Condensation

A stationary distribution for the process is a probability distribution which is invariant under the dynamics, where the distribution of the measure at time t converges to when $t \to \infty$. A measure ν on X is stationary if and only if $\nu(\mathcal{L}f) = 0$ for all observables, for a proof of this property, see Chapter 2 in [10]. If a system has translation invariant stationary product measure, it will be written as

$$\nu_\phi^L[\eta] = \prod_{x \in \Lambda_L} \nu_\phi(\eta_x) , \tag{2.10}$$

defined by product densities w.r.t. the product counting measure $d\eta$ on X_Λ, where the fugacity $\phi \geq 0$ is a parameter that controls the density of the system and will be made clear with the derivation below. The marginals therefore have the form

$$\nu_\phi(n) = \frac{1}{z(\phi)} W(n) \phi^n . \tag{2.11}$$

It should be noted in the totally asymmetric and symmetric cases, $p(x, y)$ is translation invariant. Since it is assumed that $p(x, y)$ is irreducible, on finite lattices Λ, this is in fact unique up to normalization and strictly positive. The composition of the weights is determined by the independent contributions of the factorized hop rates. $W(n)$ is written as

$$W(n) = \prod_{k=1}^{n} \frac{v(k-1)}{u(k)} , \tag{2.12}$$

which contains the factorised form of the rates as illustrated in (2.5). The normalization $z(\phi)$ is a partition function and has the form

$$z(\phi) = \sum_{n=0}^{\infty} W(n) \phi^n . \tag{2.13}$$

The density of the distribution is given by

$$R(\phi) = \langle \eta_x \rangle_\phi = \sum_{k=0}^{\infty} k \nu_\phi[k] = \frac{1}{z(\phi)} \sum_{n=0}^{\infty} n W(n) (\lambda \phi)^n \ , \tag{2.14}$$

which is a strictly monotonically increasing function with $R(0) = 0$. For systems with conserved mass, the measures are therefore indexed by a fugacity parameter $\phi \geq 0$ controlling the average number of particles per site.

Moment Generating Function

Since the partition function $z(\phi)$ is a moment generating function, (2.14) can also be written as

$$\frac{\partial \log z(\phi)}{\partial \phi} = \frac{1}{z(\phi)} \sum_{n=0}^{\infty} \lambda^n n \phi^{n-1} W(n) \ . \tag{2.15}$$

From (2.15), (2.14) is written as

$$R(\phi) = \phi \frac{\partial}{\partial \phi} \log z(\phi) \ . \tag{2.16}$$

Throughout this study, the second moment is measured as a physical quantity and it can be derived in a similar fashion. This is further explained in Sec. 3.3. The second moment at the steady state as $t \to \infty$ is given by

$$\langle \sigma^2_\infty(\phi) \rangle = \frac{1}{z(\phi)} \sum_{n=0}^{\infty} n^2 W(n) (\lambda \phi)^n \ , \tag{2.17}$$

and similarly the second moment depicted in (2.17) can be written conveniently as the moment generator form

$$\langle \sigma^2_\infty \rangle = \phi \partial_\phi \left(\phi \partial_\phi \log z(\phi) \right) \ . \tag{2.18}$$

Although it may not be clear why we want to obtain a prediction of the second moment, this will become an important property in studying the dynamics of the Explosive Condensation Process, which is the focus of this thesis. The convenience of being able to determine the second moment of the stationary distribution allows us to estimate important scaling properties.

Radius of Convergence

The existence of the product measure (2.10) requires $z(\phi) < \infty$, and we denote by

$$D_\phi^\Lambda = \{\phi \geq 0 : z(\phi) < \infty \text{ for all } x \in \Lambda\} \tag{2.19}$$

the domain of definition. Since $z(\phi)$ is a power series in ϕ, the domain is actually of the form

$$D_\phi^\Lambda = [0, \phi) \quad \text{or } [0, \phi_c]\,, \tag{2.20}$$

where

$$\phi_c = \left(\lambda \lim_{n\to\infty} \sup W(n)^{1/n}\right)^{-1}\,. \tag{2.21}$$

is the radius of convergence of $z(\phi)$.

The Particle density ρ has the range $[0, \rho_c)$ or $[0, \rho_c]$, with $\rho(0) = 0$ and $\rho_c = \lim_{\phi \nearrow \phi_c} R(\phi)$ the critical density. $\phi \to R(\phi)$ is strictly increasing. The inverse of R is denoted by $\phi(\rho)$ on the range $[0, \rho_c)$. If $\phi_c = \infty$, then $\rho_c = \infty$. Whereas if $\phi_c < \infty$, both $\rho_c = \infty$ and $\rho_c < \infty$ are possible. In the second case, $z(\phi_c) < \infty$ and ν_{ϕ_c} is a well defined probability measure with $\langle \eta_x \rangle_{\nu_{\phi_c}} = \rho_c$. So $\phi(\rho)$ is given by

$$\phi(\rho) = \begin{cases} \text{inverse of } R(\phi)\,, & \text{for } \rho < \rho_c \\ \phi_c\,, & \text{for } \rho \geq \rho_c \end{cases}\,. \tag{2.22}$$

System with Conserved Mass

We are interested in understanding how condensation occurs in systems with fixed size and mass. For a system with system size L and total mass $N \geq 0$, the new state space will be

$$X_{L,N} = \left\{\eta \in X_\Lambda \,\middle|\, \sum_{x\in\Lambda} \eta_x = N\right\}\,, \tag{2.23}$$

on which the system is a finite state irreducible Markov process. The ergodicity of the process means there exists a unique stationary measure that belongs to the canonical ensemble. This stationary measure is written as

$$\pi_N^L[\eta] := \nu_\phi \left[\eta \,\middle|\, \sum_{x\in\Lambda} \eta_x = N\right] = \frac{1}{z(L,N)} \prod_{x\in\Lambda_L} W(\eta_x)\delta\left(\sum_{x\in\Lambda} \eta_x - N\right)\,, \tag{2.24}$$

where the canonical partition function is the finite sum

$$z(L,N) = \sum_{\eta\in X_L} \prod_{x\in\Lambda_L} W(\eta_x)\,. \tag{2.25}$$

Equivalence of ensembles

The process is ergodic on the finite set $X_{L,N}$, and $\pi_{L,N}$ is the unique stationary distribution. Condensation can then be understood in terms of the equivalence of canonical and grand-canonical ensembles in the thermodynamic limit with density $\rho \geq 0$. The stationary distribution in the canonical ensemble can be written as

$$\pi_{L,N} \to \begin{cases} \nu_{\phi}, & R(\phi) = \rho \leq \rho_c \\ \nu_{\phi_c}, & \rho \geq \rho_c \end{cases} \text{, as } N, L \to \infty \text{ , } N/L \to \rho. \tag{2.26}$$

The physical interpretation is that a condensation transition is said to occur when a non-zero fraction of all the particles accumulates on a single site. In a homogeneous lattice, the system separates into a homogeneous background (fluid phase) with density ρ_c and a condensate (condensed phase), where the excess particles accumulate on a single randomly located lattice site. This transition has been established on a rigorous level in a series of papers [25, 24, 26] for models with stationary product measures in the thermodynamic limit.

By the choice of jump rates, the grand canonical single site partition function turns out to converge on the boundary of its domain, and its first derivative is finite. This implies that the average density under the grand canonical measure is increasing on $(0, \phi_c]$ and $\rho_c = R(\phi_c) < \infty$. So the grand canonical measures only exist for densities up to and including ρ_c. The product stationary distributions do not exist with higher average density. The grand canonical measure with average density ρ_c is referred to as the critical measure.

Since $R(\phi)$ is strictly increasing it is invertible. It has been shown [24] that the relative entropies between the grand canonical and the canonical probability distributions converges, hence implying weak convergence of the canonical measure to the grand canonical measure. This result implies that below the ρ_c, the canonical measure converges locally to the grand canonical measures as $L \to \infty$. Above the critical density, the canonical measures converge locally to a product of the critical grand canonical marginals with density ρ_c, and the excess mass accumulates on a vanishing volume fraction.

In the thermodynamic limit, a sketch of the relationship between ρ and ϕ is provided in Fig. 2.1. ϕ_c denotes the radius of convergence, such that a solution for ρ_c exists for $\phi \in [0, \phi_c)$, which corresponds to $\rho \in [0, \rho_c)$. For densities above ρ_c, there is no finite solution and this indicates condensation.

Using properties of the stationary distribution, it allows us to calculate the system's physical properties in the thermodynamic limit in the grand canonical ensemble. We introduce certain criteria for which the process exhibits stationary product measures,

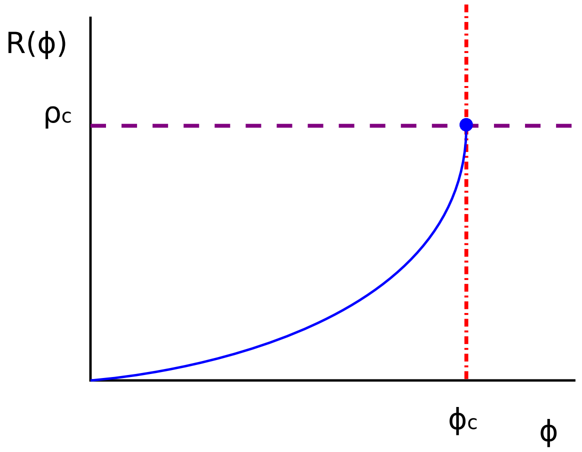

Figure 2.1: Sketch of $R(\phi)$ against ϕ for a model with condensation behaviour. The blue line indicates the mapping of density on fugacity ϕ. There is a unique value $R(\phi) < \infty$ for each fugacity $\phi \leq \phi_c$ and the system splits into a homogeneous fluid state and a condensate for $\rho > \rho_c$.

Criteria for stationary product measures

The properties derived from the grand canonical ensemble and canonical ensemble stationary measures all depend on the assumption that stationary product measures exist for the model of study. The sufficient conditions of a model that has stationary product measures are found in Theorem 2.2.1; for the proof of this theorem, see results in [23] and [27, 28, 29, 30].

Theorem 2.2.1. *Processes with generator* (2.9) *have stationary product measures of the form* (2.10) *provided that one of the following conditions holds:*

1. $v(n) \equiv 1$ *for all* $n \geq 0$

2. *The* $p(x, y)$ *fulfil the detailed balance relation:*

$$p(x, y) - p(y, x) = 0 \quad \textit{for all} \quad x, y \in \Lambda$$

   In this case the dynamics for (2.9)*are in fact reversible.*

3. *Incoming and outgoing rates p are the same for each site, such that:*

$$\sum_{y \in \Lambda} p(x, y) = \sum_{y \in \Lambda} p(y, x) \quad \textit{for all} \quad x, y \in \Lambda \tag{2.27}$$

and u and v fulfil:

$$u(n)v(m) - u(m)v(n) = v(0)(u(n) - u(m)) \quad \textit{for all} \quad m, n \geq 0 \tag{2.28}$$

The first condition takes $v(n) = 1$ but can be replaced by an arbitrary positive constant, and together with condition 3, they are known from the literature of zero-range models [9, 31, 32]. An example of the proof for the detailed balance relationship in 2 can be found in [33]. In homogeneous cases, all rates in symmetric graphs would satisfy condition 2, as the detailed balance relationship is satisfied, while for asymmetric cases and $v(n) \neq 1$, condition 3 has to be satisfied.

2.3 Examples of IPS models

In this section, we provide a review for common interacting particle systems that have attracted attention in recent years. We are particularly interested in cases with homogeneous graphs and where phase transitions are observed.

2.3.1 Zero-Range Process

The zero-range process (ZRP) is one of the earliest interacting particle systems proposed, where the transition rate is a function of the departure site occupation number only. ZRP is introduced by Spitzer [9] as an example of an interacting Markov process. The ZRP's popularity is marked by its rich non-trivial properties despite being a seemingly simple model. The ZRP is found to exhibit steady state phase-transition in its one-dimensional form. Having factorized hop rates, the ZRP has been studied in the realms of non-equilibrium statistical mechanics [31, 10, 34], including the role of conservation laws, the range of interactions, constraints in the dynamics and disorder all within the framework of an exactly solvable steady state [5, 35].

For its applications and a more comprehensive review refer to [36, 5]. Findings for the zero-range process can be applied to understanding condensation phenomena in a variety of non-equilibrium systems. The process continues to be of interest; recent work on variations of the model includes mechanisms leading to more than one condensate [37, 38, 39], or the effects of memory in the dynamics [40].

The ZRP has applications to a number of physical models, including the repton model of polymer dynamics with periodic boundary conditions [41]; a model of sandpile dynamics [42]; the backgammon model [43] for glassy dynamics due to entropic barriers; the drop-push model for the dynamics of a fluid moving through backbends in a porous medium [44]; microscopic models of step flow growth [45, 46], a bosonic lattice gas [47], traffic jam models [18], and the list goes on.

Definition

There is no restriction on the number of particles on each site, in this sense the zero-range process is a bosonic lattice gas [47]. The local state space will therefore be $\mathbb{N} = \{0, 1, ...\}$. We focus on finite translation invariant lattices with periodic boundary conditions. The state of the system, occupancy numbers all follow the definitions in Sec. 2.2.

Particles jump on the lattice at a rate that depends only on the occupation number of the departure site, hence the name "Zero-range" is given. A particle jumps off site $x \in \Lambda_L$ after a certain exponential waiting time given by rates $u(\eta_x)$ and $v(\eta_y) = 1$. This moves to a target site y with adjacency matrix

$$p(x, y) = q(y - x) \text{ for all } x, y \in \Lambda_L \, . \tag{2.29}$$

$q(n)$ also has the restriction that $q(0) = 0$ and has a finite rate, and note that it is normalized

$$\sum_{y \in \Lambda_L} q(y) = 1 \text{ and } q(z) = 0 \text{ if } |z| > r \text{ for some } r > 0 \, , \tag{2.30}$$

where r is independent of the system size L. This process is irreducible such that every particle can reach any site with positive probability. A useful property of the zero range process is that it can be mapped to an asymmetric exclusion process. This will be further explained later on in this section. The transition rate for the ZRP is given by

$$c(\eta, \eta^{xy}) = g(\eta_x) q(y - x) \, , \tag{2.31}$$

and the generator form of the ZRP is

$$\mathcal{L} f(\eta) = \sum_{x,y \in \Lambda} g(\eta_x) q(y - x)(f(\eta^{xy}) - f(\eta)) \, . \tag{2.32}$$

For example, if $g(k) = k$, for all k then the zero-range process reduces to the superposition of independent random walkers on Λ. If $g(k) = 1$ for all $k > 0$ then the zero-range process reduces to a system of L queues with mean-one exponential random times of service.

Stationary measure

The stationary measure of the zero-range process is derived in previous studies[31, 9, 36]. We focus on the thermodynamic limit $L \to \infty$, $N = L\rho \to \infty$ with fixed proportion of particles. In the canonical ensemble, the distribution of states is given by

$$\pi_N^L[\eta] := \frac{1}{z(L,N)} \prod_{x\in\Lambda_L} W(\eta_x)\delta(\sum_{x\in\Lambda} \eta_x = N)\,. \tag{2.33}$$

The canonical partition function is written as the finite sum

$$z(L,N) = \sum_{\eta\in X_{L,N}} \prod_{x\in\Lambda_L} W(n)\,. \tag{2.34}$$

The weights can be written in a recursive form encoding the factorised rates of a interacting particle system, as outlined in (2.12). Therefore, the stationary weight of ZRP can be written as

$$W(n) = \prod_{k=1}^{n} g(k)^{-1}, n > 0\,. \tag{2.35}$$

From the stationary weights, the average current is given by a ratio of partition functions

$$j_L^{\mathrm{can}}(N/L) := \pi_N^L(g(\eta_x)) = \frac{z(L,N-1)}{z(L,N)}\,, \tag{2.36}$$

for which the results would depend on the choice of g.

Condensation in ZRP

It has been shown that condensation can occur in a homogeneous zero-range process if the hop rates $g(n)$ decay slowly enough with the number of particles n. A prototype model with rates

$$g(n) = 1 + \frac{b}{n^\gamma} \text{ for } n = 1, 2, ... \tag{2.37}$$

has been introduced in [36], where condensation occurs for parameter values $\gamma \in (0,1)$, $b > 0$ or $\gamma = 1$, and $b > 2$. If the particle density ρ exceeds a critical density ρ_c, the system phase separates into a homogeneous background and a condensate. The transition has been established on a rigorous level in a series of papers [25, 26, 24] in the thermodynamic limit. Dynamical aspects of the transition such as equilibration and coarsening [48, 24] and the stationary dynamics of the condensate [49] are well understood heuristically.

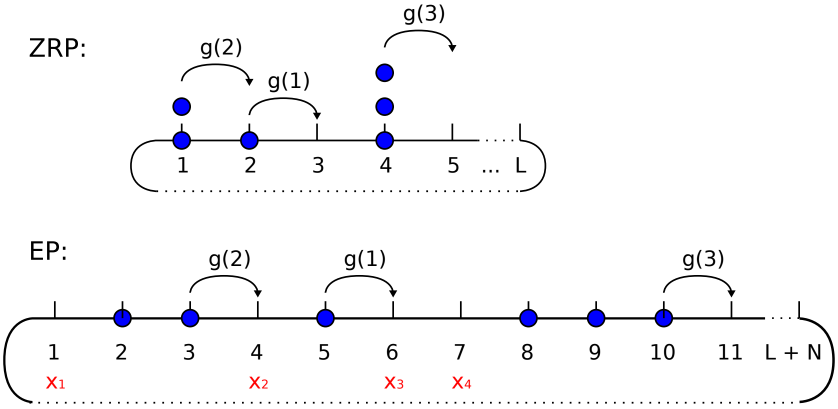

Figure 2.2: Equivalence between the zero range process and the exclusion process. The top is an example of the zero range process and the bottom the exclusion process. The translation between the two is illustrated in the text.

Mapping to the exclusion Process

An interesting property of the ZRP is that it can be mapped to the exclusion process, which is a fermionic model. In the exclusion process, the lattice sites are either occupied by a single particle or are vacant. The general rule of the mapping is illustrated in Fig. 2.2. We consider the general form of the exclusion process [13] such that rates are dependent on the overall configuration. The local state space of the exclusion process is $E = \{0, 1\}$, where the site is either occupied or vacant. Transition of particles only occurs when the receiving site is vacant.

If the size of the lattice for the ZRP is L, then the lattice size of the exclusion process is $L + N$, such that the state space is

$$X^{\text{EP}}_{L+N} = \left\{\eta = (\eta_x)_{x\in\Lambda^{\text{EP}}_{L+N}} : \eta_x \in \{0, 1\}\right\} = \{0, 1\}^{\Lambda^{\text{EP}}_{L+N}} , \tag{2.38}$$

where N is the number of particles in both processes and is conserved. In the exclusion process' mapping of the zero range process, each site on the zero-range process lattice would be represented by a vacant spot in the state space. The occupancy of a site in the zero range process represents the number of consecutive non-vacant sites in the exclusion process. A transition only occurs in the rightmost particle of a chain of particles, where the rate is dictated by waiting times given by a function of the departure site. For the totally asymmetric case, the generator of the exclusion process is as

$$\mathcal{L}f(\eta) = \sum_{x\in\Lambda}(\eta_x(1 - \eta_{x+1}) + (f(\eta^{x\to x+1}) - f(\eta)) . \tag{2.39}$$

2.3.2 Inclusion Process (IP)

The distinctive feature of the ZRP is that its rates depend only on the occupancy of the departing site. A natural progression to consider is a model with transition rate that is dependent on both the departure and receiving site occupancies. This is synonymous to physical systems, where there is a repulsive and attractive term.

The inclusion process is first introduced in [50, 51] as a dual process to the Brownian energy process in 2007. The IP can also be regarded loosely as a bosonic counterpart of the exclusion process, as there are no restrictions on the number of particles on lattice sites.

The IP is a simple interactive particle model that has received considerable attention in the last years. The properties of IP on a general graph have been studied in [50, 51, 52]. However, there are two cases of IP that have been specifically studied, namely the nearest neighbour symmetric inclusion process (SIP) and the totally asymmetric inclusion process (TASIP). The correlation inequalities in the SIP and the asymmetric inclusion process are analysed in [52, 53]. The inclusion process is demonstrated to have stationary product measures under general conditions in [33], where condensation occurs when diffusivity goes to zero [33, 54]. In contrast to the ZRP, in the IP and related models condensates are mobile on the coarsening time scale. Although coarsening behaviour is studied heuristically in ZRP [36, 48, 24, 49, 5] and related models [55, 27, 56], the IP are different as coarsening is driven by condensate motion and interaction [57, 23].

Definition

We follow the state space and configuration set up as described in Sec. 2.2, where a connected, translational invariant, lattice Λ_L of L sites with periodic boundaries is used. The local state space for the process is the same as for the zero-range process, namely $\mathbb{N}$, so that the full state space on a system of size L is $X_L = \mathbb{N}^{\Lambda_L}$. Particles diffuse on the lattice independently (performing independent random walks) with diffusion constant d which could depend on the size of the system. In addition to the diffusive dynamics particles also attract each other, every particle at site x attracts all particles at site y with rate $p(x, y)$. This is the so-called 'inclusion' attraction. The transition rate of the inclusion process is given by

$$c(\eta, \eta^{xy}) = \eta_x(\eta_y + d)p(x, y) , \tag{2.40}$$

where the generator is written as

$$\mathcal{L}f(\eta) = \sum_{x,y\in\Lambda_L} \eta_x(d + \eta_y)p(x, y)(f(\eta^{xy}) - f(\eta)) . \tag{2.41}$$

A schematic view for TASIP is presented in Fig. 2.3. Note that the generator is used

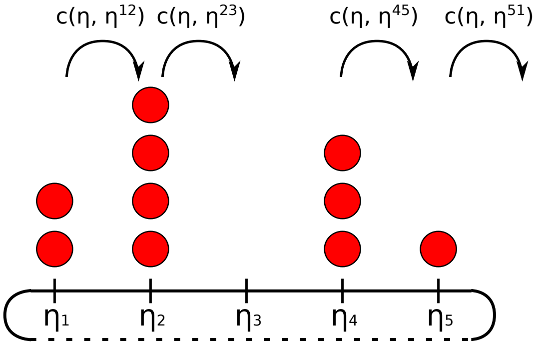

Figure 2.3: Schematic view of TASIP on periodic boundary condition. Particles are able to jump to the right only. The dynamics of the model is characterized by (2.41). Transition rates are dependent on both departing and receiving sites.

as an example in Sec. 3.3.1 to provide an exact solution on observables in the next Chapter in Sec. 3.3.1.

Stationary Measure

Stationary product measures for the SIP were derived in [50, 51] and extended in [33, 23] to more general spatial rates, including TASIP. The translational invariant systems have homogeneous product measures

$$\nu_\phi^L[d\eta] = \prod_{x\in\Lambda_L} \nu_\phi d\eta \quad \text{where} \quad \nu_\phi[\eta] = \frac{1}{z(\phi)} W(n)\phi^n \, , \tag{2.42}$$

where ν_ϕ^L is the product density with respect to product counting measure $d\eta$. $\phi \geq 0$ is the fugacity parameter controlling the particle density. The composition of the weight of IP is determined by the contributions of the factorised components of the rates, as outlined in Sec. 2.2.3, and we write this as

$$W(n+1) = \frac{d+n}{n+1} W(n) \, . \tag{2.43}$$

The recursive format of (2.43) can be simplified by collecting the successive products of the weights. The weight of IP can be written in the form of (2.12) and the weight becomes

$$W(n) = \frac{\Gamma(d+n)}{n!\Gamma(d)} \, . \tag{2.44}$$

The partition function is written as

$$z(\phi) = \sum_{k=0}^{\infty} W(k)\phi^k = (1-\phi)^{-d}. \tag{2.45}$$

The partition function diverges as $\phi \nearrow 1$, the measures exist for all $\phi \in [0, 1)$ and constitute the grand canonical ensemble. The average particle density is a function of ϕ, and is given by

$$R(\phi) = \sum_{k=0}^{\infty} k\nu_\phi(k) = \phi\partial_\phi \log_z(\phi) = \frac{d\phi}{1-\phi} . \tag{2.46}$$

For the TASIP the average stationary current is given by the average jump rate off a site, which also determines the corresponding diffusivity for the symmetric system. Under the grand canonical ensemble this is given by

$$j^{gc}(\phi) = \mathbb{E}[\eta_x(d + \eta_{x+1})] = R(\phi)(R(\phi) + d) , \tag{2.47}$$

depending only on the particle density and d.

Condensation in IP

For fixed L and d, the range of densities is $R(0, 1) = [0, \infty)$ and the process does not exhibit condensation in the usual sense of zero-range processes or in related models, where the range is bounded as explained in Chapter 2.3.3. But it has been established in [33] [58] that in the thermodynamic limit with vanishing diffusion rate

$$L, N \to \infty, d \to 0 \text{ such that } \frac{N}{L} \to \rho > 0 \text{ and } dL \to 0 , \tag{2.48}$$

such that $R(0, 1) = [0, \rho_c)$. Contrary to ZRP, the condensate in IP is mobile. It has been identified that the stages to condensation can be divided into four regimes. Namely the nucleation stage, coarsening stage, saturation regime and stationary regime. For $d \to 0$, coarsening behaviour dominates and hence drives the formation of the condensate.

Significance of the Inclusion Process

The IP is a relatively recent model in IPS literature, yet it has demonstrated that condensation can be achieved with spatial homogeneity. The physical interpretation is that, as the diffusive rates are so small compared to the rates of exchange between clusters, small clusters are able to gain mass and a condensate is formed. This leads to questions on whether other models can achieve condensation but with higher diffusive rates, but with a stronger dependency on the mass of the attractive and repulsive sites. This motivation leads to the

Explosive Condensation Process.

2.3.3 Explosive Condensation Process (ECP)

A spin-off version of the IP is the explosive condensation process, which is first introduced in [6] and further studied in [59]. The motivation of this model is to introduce a novel mechanism of non-equilibrium condensation, where aggregation of particles speeds up in time as a result of increasing exchange rate of particles. The ECP has stationary product measures, where the rates are carefully chosen such that $W(n) \sim n^{-\gamma}$ and $\gamma > 2$. In this case, condensation can be achieved, and interesting condensation behaviours might result from this set up. A heuristic study of the formation of the condensate reveals "explosive condensation" for the totally asymmetric case, where the time to condensate $\langle T_{\mathrm{SS}} \rangle$ goes to zero in the thermodynamic limit $L \to \infty$ as is explained in detail in Section 3. Similar to the dynamic properties of condensation in IP, the formation of a condensate is dependent on dynamics of various stages of system evolution.

Definition

A totally-asymmetric one dimensional lattice with periodic boundary conditions is considered, where hop rates occur with rates $u(m, n) \sim (mn)^{\gamma}$, where m and n are the occupancy of the departure and receiving sites, and $\gamma > 2$. The formation of a condensate occurs extremely quickly so that it is termed *explosive* and has interesting scaling properties. Following the definitions outlined in Sec. 2.2. the transition rates of the ECP are given by

$$c(\eta, \eta^{xy}) = ((\eta_x + d)^{\gamma} - d^{\gamma})(\eta_y + d)^{\gamma} \text{ for } \gamma > 2\,. \tag{2.49}$$

Note that if $\gamma = 1$, the ECP becomes the IP. The generator of the ECP is given by

$$\mathcal{L}(f(\eta)) = \sum_{x \in \Lambda_L} p(x, y)((\eta_x + d)^{\gamma} - d^{\gamma})(\eta_y + d)^{\gamma}[f(\eta^x y) - f(\eta)]\,. \tag{2.50}$$

In [6, 59], only the totally asymmetric case is studied, so $p(x, y)\delta_{y,x+1}$. Similar models to the ECP are studied in this thesis; for a derivation of the stationary product measure of a variant of the ECP that encompasses it, see Sec. 3.4.1.

Explosive condensation in ECP

Condensation is observed in ECP, with the rate of mass accumulation increasing as a site gains mass. A heuristic analysis of the formation of the condensate has been studied for the totally asymmetric case. The condensation of ZRP and ECP is compared in [59], where a completely different mechanism of condensation can be observed. The scaling of the time to condensate is reported to be decreasing with system size $\langle T_{\mathrm{SS}} \rangle = C(c_2 + c_3 \ln L)^{1-\gamma}$. This allows us to arrive at the counter-intuitive conclusion that $T_{\mathrm{SS}} \to 0$ for $L \to \infty$.

Chapter 3

Condensation in Interacting Particle Systems

3.1 Introduction

In Chapter 2, we have provided a definition for IPS and introduced common analytical tools for such systems. A review of key models are also presented, including a discussion on recent developments of systems that demonstrate the phenomena of explosive condensation. In this chapter, we will focus on the general properties of condensation and explosive condensation models.

Condensation is commonly used to depict the transition of gas to its liquid phase on surfaces. However, in the realms of statistical physics, condensation describes a very different process albeit conceptual similarities can be drawn. In non-equilibrium statistical systems, condensation generally means a concentration of system mass on some local space. The most famous example of condensation in physical systems is the Bose-Einstein condensate, where a positive fraction of all particles present in the system assumes the lowest energy state on the momentum space. Other physical examples include the modelling of polydisperse hard spheres [60], complex network hub formations [61] and quantum gravity [62]. This type of condensation also extends far into realms of social science models, such as traffic jam models [19, 18], crowd dynamics and wealth distribution [63].

While condensation behaviours for homogeneous mass interaction models have been studied for continuous state spaces [51, 64, 28], in this study we focus on models with discrete state spaces. For the model with particles on discrete state space with no confinements on mass per site, and mass is conserved with thermodynamic limit $N \to \infty$, $L \to \infty$ $N/L \to \rho$, condensation means the manifestation of a fraction of system mass on small volume fraction, typically a single lattice site.

There are many reasons for why condensation occurs. Condensation in interacting particle systems was originally studied [65, 66, 67, 68] mostly for spatially inhomogeneous cases, where geometric set-up of the graphs can lead to the formation of condensates on designated localized sites. In such geometries, specific sites might have high incoming rates and slow exit rates, such that a substantial mass can be "stuck" locally in the stationary state. Contrary to a spatially inhomogeneous geometry, increasing attention has been given to condensation with spatial homogeneity [69, 36] in recent years. In these cases, condensation dynamics are driven by particle interactions. Typically, rates are multiplicative such that interactions between large clusters are more frequent than interactions between smaller clusters. In these cases, large clusters are formed and eventually dominate to become the condensate. Contrary to the spatial inhomogeneous cases, the site on which the condensate is formed is distributed uniformly on the lattice due to the symmetric nature of the models.

For both spatially inhomogeneous and homogeneous cases, a rigorous framework has been formulated for behaviour of such models with stationary product measures [67, 68, 70]. It has been shown that in the spatially homogeneous case, by carefully choosing the rates of a model such that the weight functions of the stationary product measures have interesting asymptotic properties, condensation behaviour can be observed [6, 59]. Under such a framework, interacting particle models are demonstrated to have stationary product measures under certain conditions (see Sec. 2.2.3), and with the properties of stationary product measures, the phase transition in condensation behaviour can be studied. Condensation occurs when the system density exceeds some critical density ρ_c. At condensation, the mass of the system is separated into a condensate and a fluid phase, where the fluid phase is distributed according to the maximal invariant measure. The condensate consists of the "excess mass" $(\rho - \rho_c)L$ of the system concentrated on a single site. The generator can be used to derive useful and simple results that describe the condensation of the system. The description of condensation up to this point is for a general class of models, where there is no definite characterization on how a condensate forms.

In this thesis, we are interested in the ECP model and its variants, of which the formation of its condensate is deemed to be "explosive". Broadly speaking, "explosive condensation" is a phenomenon caused by the increase in speeds of interaction during particle assimilation due to multiplicative rates. The average time to condensation $\langle T_{\mathrm{SS}} \rangle$ for this model scales very counter-intuitively and implies $T_{\mathrm{SS}} \to 0$ for $L \to \infty$.

This Chapter is organized as follows. We propose two models in Sec. 3.2 that exhibit "explosive condensation", where one of them is a generalized form of the model proposed in [6] and the other is chosen with similar scaling behaviour in the stationary product measure. The relationship between stationary product measures and condensation is discussed in Sec. 3.2.1. Certain physical observables for studying the formation of condensates are introduced in Sec. 3.3, which would serve as tools for the microscopic study of the models in Chapter 4. Solving for these observables from the generator is attempted, and they are compared to results from the inclusion process. The regimes where the system transitions into condensation for the said models are discussed in Sec. 2.2.3, where numerical results are compared with these findings.

3.2 The model and its variations

We narrow down from the broad definition of interacting particle systems to specific cases of interest. For a continuous-time Markov process on a discrete one-dimensional lattice, where models are characterized by their rates in the generator, we follow the definition of the state space and interacting rules as described in Sec. 2.2. The models introduced in this section take inspiration from the mass transport model proposed by Waclaw and Evans [6] and outlined in Sec. 2.3.3. The model is characterized by the following rates

$$c(\eta, \eta^{xy}) = ((\eta_x + d)^\gamma - d^\gamma)(\eta_y + d)^\gamma p(x, y) \quad \text{, where } \gamma > 2, d > 0 \ . \tag{3.1}$$

Here d and γ are model parameters that are unchanged during the interaction. The model characterized by rates (3.1) has factorized rates in the form of (2.5) and also has stationary product measures, which is further explored in Sec. 2.2.3. Insights into "explosive dynamics" are drawn from this specific model. We are interested in understanding how properties of the Waclaw and Evans' model might lead to the phenomena of explosive condensation. To do this, we start from writing down a general form of the model and study why certain parameters would lead to explosive condensation. Instead of having the same non-linearity term γ, we propose a variation where the non-linear terms are separately introduced as γ_1 and γ_2. The modified model has rates

$$c(\eta, \eta^{xy}) = ((\eta_x + d)^{\gamma_1} - d^{\gamma_1})(\eta_y + d)^{\gamma_2} p(x, y) \quad , \tag{3.2}$$

where $\gamma_1, \gamma_2 > 0$, $d > 0$. Both totally asymmetric and symmetric cases of (3.2) will be studied. Note that the inclusion process (IP) can be retrospectively regarded as a special form of (3.2) where $\gamma_1 = \gamma_2 = 1$.

Bearing the non-linear properties of Eq. (3.2) in mind, we invent another model with similar γ_1 and γ_2 scaling that also has stationary product measures (see criteria for stationary product measures in Sec. 2.2.3). The purpose of introducing another model of a similar nature is to better understand the properties of explosive condensation, especially how the diffusive term d would influence the stationary state of the system. The rates of the new model is given as

$$c(\eta, \eta^{xy}) = (\eta_x^{\gamma_1})(\eta_y^{\gamma_2} + d)p(x, y) \; . \tag{3.3}$$

Note that for $\gamma_1 \neq \gamma_2$ the above models only have stationary product measures for symmetric $p(x, y)$, and not for homogeneous asymmetric dynamics.

Range of parameters used in simulation

Before illustrating the schematics of condensation, we briefly outline the reasoning behind the choice of the range of parameters in our example plots throughout this chapter, for which a detailed reasoning will be elaborated in Chapter 4 and 5. For the explosive condensation models, the key parameters are:

- γ: The non-linear factor is taken to be $\gamma > 2$, as this is the regime where condensation is to occur (see Sec. 3.4.1). Saying of which, a high γ would lead to an easy trigger of explosive condensation (see Sec. 4.3 and 4.4). The development of an explosive condensate is a multi-stage process, and the overall scaling properties of ECP depends on the dynamics of early stages. Observations of key processes in the system's initial stages will be made difficult by rapid particle assimilation introduced by a high γ. Principally, a high γ makes relatively very little difference in the physical manifestation of explosive condensation models. However, γ is kept low for presentation purposes. From the experience of simulating these models, we choose γ to be within the range $[2, 7)$ throughout the thesis.

- d: The diffusive parameter d is taken to be of order $\sim O(1)$, as we are interested in understanding our models with arbitrary finite diffusivity. The case of vanishing diffusivity $d \to 0$ is studied separately in Sec. 6.2. However, for presentation purposes, usually a relatively smaller d is taken to provide a clearer separation between different stages in the evolution of dynamics. This is further elaborated in Sec. 4.1, 4.3 and 4.4. Therefore d is typically chosen within the range $[0.01, 1)$, but almost always $d > 1/L$.

- ρ: The density of the system is taken to be an integer. The density usually satisfies $\rho > \rho_c$, where ρ_c is numerically computed as outlined in Sec. 3.4, unless otherwise stated. Bearing this in mind, it can be numerically expensive to simulate systems with large numbers of particles $N = \rho L$, therefore ρ is usually chosen to be $\sim O(1)$. A list of ρ_c for the system parameters used throughout this thesis is provided in Appendix D.

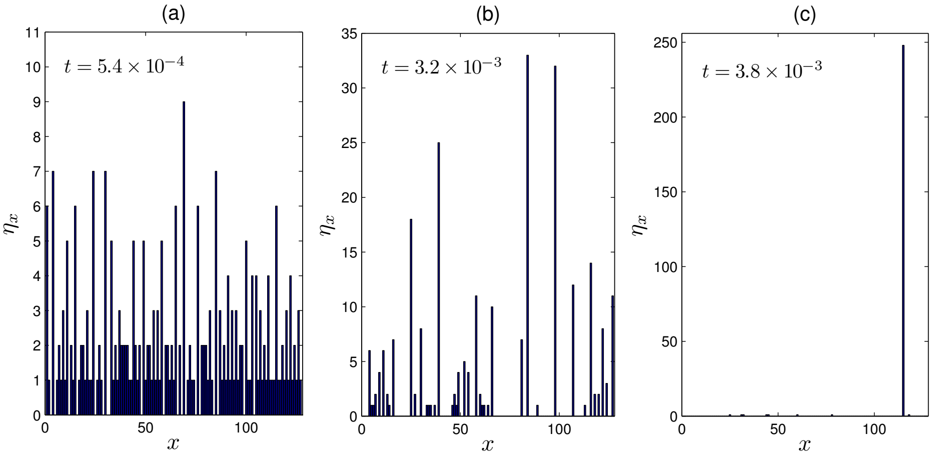

Figure 3.1: For $\gamma = 5$, $\rho = 2$, $L = 128$, $d = 0.01$, for the model characterized by rates (3.2) on a totally asymmetric graph, and particles initiated on the lattice multinomially. Three instances of the full configuration of the system are plotted. (a) Shortly after the beginning of the dynamics. (b) Just before the domination of one cluster. (c) Condensate is formed embedded on the background with some critical density, which can be computed in (2.14). Compare to the time-dependent cross-section plot of Fig. 3.2, which has different parameters but outlines the same stages leading up to condensation.

- L: The system size L has to be sufficiently big for the effects of explosive condensation to be apparent. To have a clear distinction between the fluid and the condensate, and for $\rho \sim O(1)$, sizes of systems are usually set to be $L > 10^2$. Our simulations do not go beyond $L \sim 10^5$ due to numerical costs of doing so.

3.2.1 Condensation

To give a schematic illustration of the formation of an "explosive condensate", the original Waclaw and Evans' model as characterized in (3.1) is simulated and plotted in Fig. 3.1, where the configuration η of the system at three different instances are shown. Particles are randomly distributed initially, and they transition to an intermediate stage where the dynamics are dominated by a large cluster that eventually forms the condensate. Notice that there are several particles in the background long after a condensate is formed, corresponding to a fluid state with density ρ_c .

In addition to the configuration plots, we plot the location of the three most occupied sites against time in Fig. 3.2. Note that the parameters used in Fig. 3.1 are different from Fig. 3.2, but the same stages to stationarity are observed. This is a totally asymmetric model with periodic boundary conditions, which means that particles can only move in one direction (upwards along the y-axis of Fig. 3.2 on a torus, as the lattice Λ is mapped on

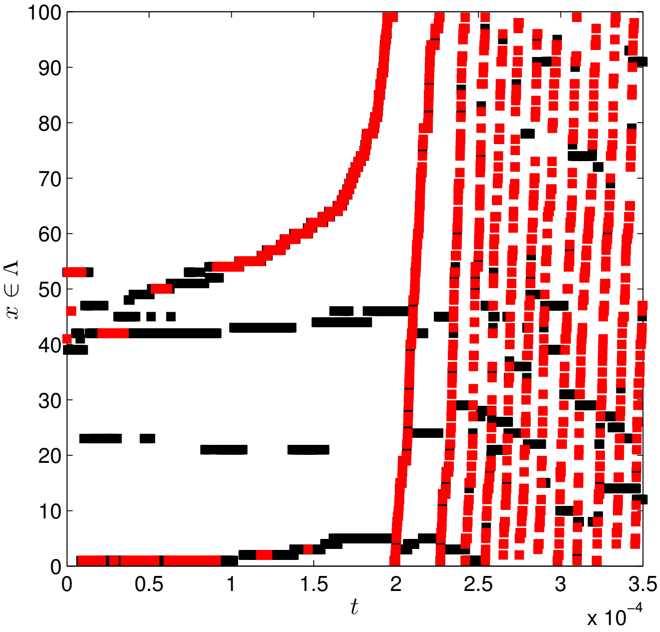

Figure 3.2: $L = 100$, $\rho = 4$, $d = 0.1$, $\gamma = 3$, totally asymmetric graph, for model characterized by rates (3.2). Positions of the maximum occupancy (red), second and third maximum occupancies (both in black) are plotted against time. Compare with Fig. 3.1 to see full configuration of occupancies at selected instances. Note that the parameters are different from Fig. 3.1 because they are arbitrarily chosen, as we are only interested in the schematic behaviour of explosive condensation.

to the y-axis). The speeds of the largest cluster (in red) can be estimated by its relative position on the lattice as time proceeds. Although the sizes of clusters are not indicated on this plot, we know from configuration plots that clusters gain particles as they move across the lattice.

As the red colour indicates the cluster with the highest number of particles, the fact that it interchanges between red and black in the range $t \in [0, 10^{-4})$ suggests that clusters are competing for being the largest cluster. At first, several clusters are competing for particles, until one cluster dominates at around $t = 1.5 \times 10^{-4}$ and accelerates. Note that time t is a unit of time that is obtained as the reciprocal of rates, meaning that the physical length of time is characterised by the physical units of rates. In this study, we have not attached a definitive physical measurement to rates, which is the common practice in literatures of this field. Therefore, t has no physical unit, it is nevertheless a consistent measure used throughout the thesis that is characterised by the rates of interaction. The dominating cluster gains speed and mass from interacting with other clusters, and condensation occurs at around $t = 2.25 \times 10^{-4}$.

From Fig. 3.2, the speeds of clusters can be estimated by the gradient of the position of clusters against time. From $0 \leq t < 1 \times 10^{-4}$, two clusters are competing to be the cluster with the highest mass. This corresponds to the instant at which Fig. 3.1 (b) is measured. From $1 \times 10^{-4} < t < 2.25 \times 10^{-4}$, one cluster is evidently dominant and increases in speed. In this period, the second highest and third highest cluster can be observed to be moving at a much slower speed. For $t > 2.25 \times 10^{-4}$, the dominant cluster becomes totally dominant and moves through the system in very little time. The dominating cluster accelerates as it "eats up" other clusters with an increasing rate. Its speed approaches a constant as its mass reaches $m \sim (\rho - \rho_c)L$. This corresponds to the instant at which Fig. 3.1 (c) is measured, where particles can be observed in the background in its steady state.

As the largest cluster moves across the system with increasing speed, there is an illusion where smaller clusters are moving in the opposite direction, which can be observed at around $t = 2.25 \times 10^{-4}$ onwards in Fig. 3.2. This characteristic feature is counter-intuitive, as the graph is totally asymmetric and particles can only move in one direction. This seemingly backward movement of particles is caused by the stochastic effects in the transfer of mass between clusters, where part of the condensate is "left behind" after it has collided with a smaller cluster. For a detailed explanation of this process, see Fig. 4.8 in Sec. 4.2.2 or [6].

A novel finding of the explosive condensation process is that the time to stationarity decreases with increasing system size. The scaled maximum occupancy number $\eta_{\max}/N$, which is the size of the site with the highest occupancy, is plotted against time in Fig. 3.3. The system reaches stationarity when almost all particles are concentrated in one cluster. The time to steady state is heuristically estimated to scale $\sim (\ln L)^{1-\gamma}$ in [6]. This implies for $L \to \infty$, steady state is reached instantly. The heuristic derivation of this intriguing result can be found in Appendix C, and a simpler novel alternative explanation will be introduced in Chapter 4.

3.3 Tools to characterize explosive condensation

Studying the evolution of the maximum occupancy number $\eta_{\max}$, as outlined in the previous section, is one of the many methods in observing the various stages of explosive condensation. The maximum occupancy number is the occupancy measurement of one single site only, and it is not representative of the entire configuration. Step-by-step evolution of system configuration cannot be properly understood without a physical description of the entire system configuration, such as the second moment σ^2 of the configuration. In Sec. 3.2, we will properly define $\eta_{\max}$ and σ^2, which will be used for analysing the models throughout this thesis. The time to condensation T_{SS} , which is an important property that charac-

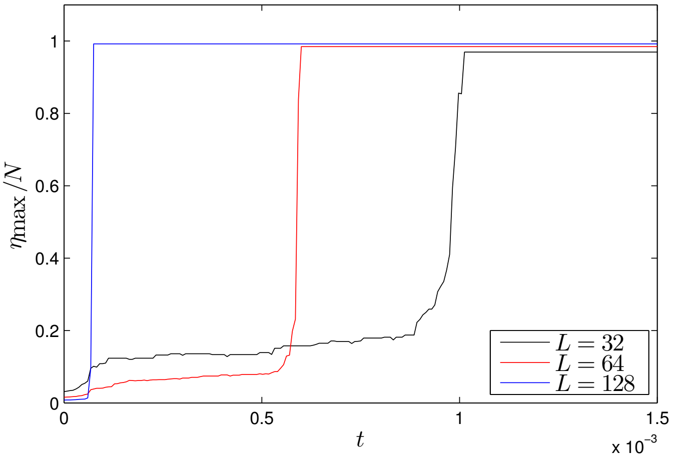

Figure 3.3: The scaled size of the largest cluster is plotted against time for $\gamma = 5$, $d = 0.5$ for the model with rates (3.1). At $\eta_{\text{mas}}/N \to 0$, all particles are concentrated on one cluster site.

terises explosive condensation, is also defined. The numerical efficiency and accuracy in measuring a reliable T_{SS} is also discussed in this section.

The stages to stationarity using such measurements are subsequently calculated from the generator for the $\gamma_1 = \gamma_2 = 1$ case of the ECP or the inclusion process in Sec. 3.3.1. Attempts are made to repeat the same computation for the general ECP model, and discussions are provided to outline why this is ineffective. Note that the tools introduced in this section will be used throughout this chapter and Chapter 4.

Maximum Occupancy

The simplest physical measurement is the maximum occupancy $\eta_{\max}$, which is the occupancy of the highest occupied site in the configuration η. This is defined as

$$\eta_{\max} = \max_{x \in \Lambda}\{\eta_1, \eta_2, ..., \eta_L\} \,. \tag{3.4}$$

Although this is not a generic measurement for the entire system, the evolution of the occupancy of the maximum site $\eta_{\max}(t)$ can be a useful description for cluster-driven dynamics at the later stages of the dynamics (see Sec. 4.2). This is especially useful for cases with explosive condensation. This is because it provides an accurate measurement of when the system reaches stationarity with $\eta_{\max} = (\rho - \rho_c)L$, where only one cluster dominates. $\eta_{\max}$ can also be used to compute the time to steady state $\langle T_{\text{SS}} \rangle$, which is defined in (3.5).

Second moment σ^2

The models of study are continuous time discrete space models, where for most cases a non-equilibrium steady state contains the condensate. It is therefore advantageous to have global measurements, alongside $\eta_{\max}$, that characterise the system-wide distribution and are not constrained for local measurement. The second moment σ^2 across the system can be measured and is defined as

$$\sigma^2 = \frac{1}{L} \sum_{z \in \Lambda} \eta_z^2 \ . \tag{3.5}$$

This is the simplest observable that captures the temporal evolution of the condensed phase, since the first moment is constant in time due to conservation of the number of particles. Due to spatial homogeneity, the expectation of (3.5) is equal to the expected value of η_x^2 for all x. In simulations we approximate the expectation by averaging over $\langle 1/L \sum_{x=1}^{L} \eta_x^2 \rangle$, denoted by $\langle \cdot \rangle$ (typically 100 in our simulations) of realizations. This is particularly useful in studying the evolution of the system for coarsening dynamics (see Sec. 4.5.2), where several clusters dominate and a single condensate has not been formed yet. However, we use $\langle \sigma^2 \rangle$ with caution for monotonic increasing cases that are also extremely sensitive to waiting times. In fact, for some cases in Chapter 4, regular second moment intervals are averaged over instead of averaging over regular time intervals. This is discussed in greater detail in Sec. 5.2.

Time to condensate

One of the main findings in ECP studies is that the time to steady state decreases with L [6, 59], such that for $L \to \infty$, the time to steady state $T_{\mathrm{SS}} \to 0$. The time to steady state is the time required for a system with particles that are initially distributed with uniform probability on a site reaching its steady state. T_{SS} is written as

$$T_{\mathrm{SS}}^{\sigma^2} = \begin{cases} \inf_{t>0} \left\{ t : \sigma^2(t) > (\rho - \rho_c)^2 L - a\sqrt{L} \right\} & , \text{if } \rho \geq \rho_c \\ \infty & , \text{for } \rho < \rho_c \ , \end{cases} \tag{3.6}$$

where ρ_c is the critical density of the system, such that when a condensate forms, ρ_c is the background density and $a\sqrt{L}$ are the expected fluctuations of the system (see Sec. 4.5.1). Consistent with the characteristics of IPS with stationary product measures having condensation in its steady state, $(\rho - \rho_c)L$ is the expected mass of the condensate. The critical density ρ_c can be predicted by the numerical computation of (2.14) (see Sec. 2.2.3).

Numerically estimating T_{SS} may be computationally expensive for system sizes of interest. This is due to the characteristics of cluster dynamics being extremely repetitive for large clusters. It is difficult to provide a definitive explanation at this stage, but this would be clearer as properties of cluster dynamics are explained in Sec. 4.2. The issue with computational costs for large clusters is further elaborated in Chapter 5. Bearing these in mind, we use several simplifications throughout this thesis when estimating T_{SS}. These methods can be categorized into two categories.

- For systems with explosive condensation, T_{SS} can be estimated when $\eta_{\max}$ reaches some critical occupancy (see Sec. 4.4), as the cluster would cover the entire lattice in an extremely rapid time.
- Secondly, for systems with no explosive condensation (such as the case $\gamma_1 = \gamma_2 \in (2, 3)$), the scaling behaviour of T_{SS} with L can be quickly estimated by the time it reaches a certain level of second moment.

Although these examples do not strictly follow (3.6), they nevertheless provide a reliable estimate of T_{SS} in the said conditions, and their accuracies discussed in the sections mentioned.

3.3.1 Example: Inclusion Process

Choosing $\gamma_1 = \gamma_2 = 1$, the models with (3.2) and (2.40) become the IP, which was introduced in Sec. 2.3.2. Note that this is no longer the ECP and does not have condensation behaviour for $d = O(1)$. This case is used as a benchmark study to the dynamics of explosive condensation. In this example, $\sigma^2(t)$ for the IP is solved using the generator in the complete graph and Erdős-Rényi graph.

The adjacency matrix $p(x, y) = 1$ for $x \neq y$, and 0 otherwise in the complete graph. Taking the generator of the IP in (2.41), and substituting the observable $f(\eta) = \eta_z^2$, the generator is written as

$$\mathcal{L}\eta_z^2 = \sum_{x\in\Lambda} \eta_x(\eta_z + d)[(\eta_z + 1)^2 - \eta_z^2] + \sum_{x\in\Lambda} \eta_z(\eta_x + d)[(\eta_z - 1)^2 - \eta_z^2] , \tag{3.7}$$

and this can be expanded and simplified to

$$\mathcal{L}\eta_z^2 = \sum_{x\in\Lambda} \eta_x(\eta_z + d)[2\eta_z + 1] + \sum_{x\in\Lambda} \eta_z(\eta_x + d)[-2\eta_z + 1] . \tag{3.8}$$

Collecting η_z and taking $\sum_{x\in\Lambda}$, η_z is independent of this summation, so (3.8) becomes

$$\mathcal{L}\eta_z^2 = \eta_z^2(-2dL) + \eta_z(2dN + 2N + dL) + dN. \tag{3.9}$$

Recalling the second moment as defined in (3.5), the second moment of the inclusion process is obtained by summing over (3.9) and dividing it by L gives

$$\frac{1}{L}\sum_{z\in\Lambda}\mathcal{L}\eta_z^2 = \frac{1}{L}(-2dL)\sum_{z\in\Lambda}\eta_z^2 + \frac{N}{L}(2dN + 2N + dL) + \frac{L}{L}dN\,. \tag{3.10}$$

Taking the mean-field approximation and recalling the properties of generators in Sec. 2.2.1, (3.10) can be written as a first order ordinary differential equation

$$\frac{d}{dt}\mathbb{E}\sigma_t^2 = \frac{d\langle\sigma_t^2\rangle}{dt} = -2dL\langle\sigma_t^2\rangle + \frac{2dN^2}{L} + \frac{2N^2}{L} + 2Nd\,. \tag{3.11}$$

An ansatz solution is used to solve (3.11), which is written as

$$\begin{aligned} \langle\sigma_t^2\rangle &= a + be^{-\lambda t} \\ \frac{d}{dt}\langle\sigma_t^2\rangle &= -\lambda be^{-\lambda t}\,. \end{aligned} \tag{3.12}$$

Let $k_1 = -2dL$ and $k_2 = \frac{2dN^2}{L} + \frac{2N^2}{L} + 2Nd$ for simplicity in manipulation of terms, and substitute the results in (3.12) to (3.11). Collecting the terms, (3.12) becomes

$$\langle\sigma_t^2\rangle = \rho^2 + \frac{\rho^2}{d} + \rho + \left(\langle\sigma_0^2\rangle - \rho^2 - \frac{\rho^2}{d} - \rho\right)e^{-2dLt}\,, \tag{3.13}$$

The early dynamics of the system where $\langle\sigma_0^2\rangle \gg \rho^2 + \frac{\rho^2}{d} + \rho$ is dominated by the exponential decay

$$\langle\sigma_t^2\rangle = \langle\sigma_0^2\rangle e^{-2dLt}\,. \tag{3.14}$$

Numerical results for $\langle\sigma_t^2\rangle$ compared to (3.13) and (3.14) with varying parameters in Fig. 3.4, where two sets of initial conditions converge to the same scaled second moment.

Taking $t \to \infty$ for (3.13), the second moment of the steady state is obtained

$$\langle\sigma_\infty^2\rangle = \rho^2 + \frac{\rho^2}{d} + \rho\,, \tag{3.15}$$

to which the numerical results in Fig. 3.4 converge. For $d = O(1)$, $\langle\sigma_\infty^2\rangle$ is finite. The convergence of the system to a finite second moment suggests that the inclusion process does not have condensation behaviour for $d = O(1)$. In the case $d \to 0$, second moment $\langle\sigma_\infty^2\rangle \to \infty$, which implies condensation as reported in the literature [57, 54] in the said domain. Numerical results for σ_∞^2 are compared with (3.15) in Fig. 3.5, over different instances of ρ and d.

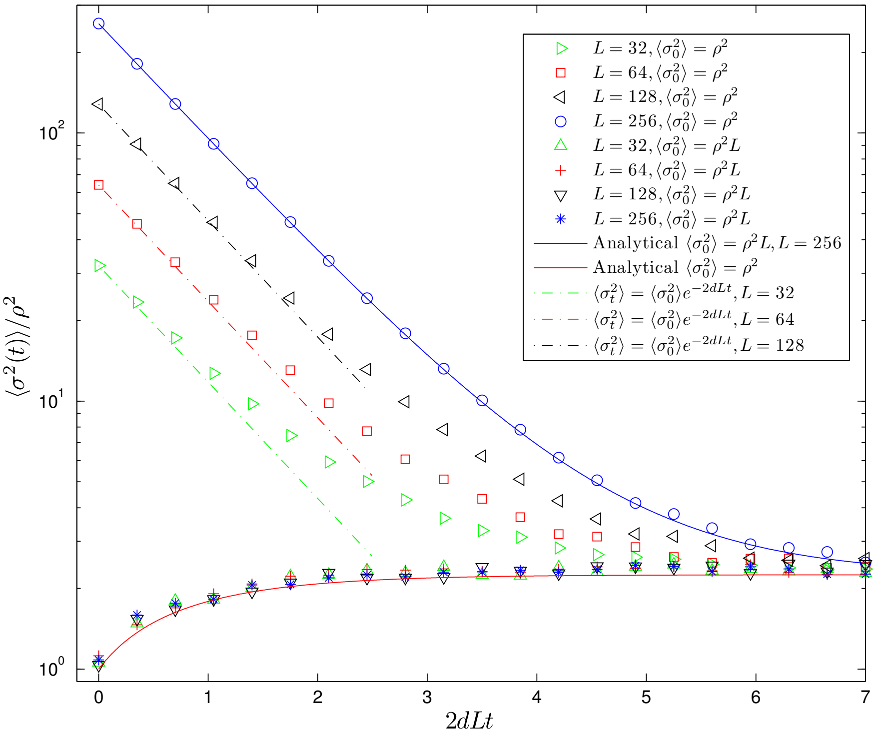

Figure 3.4: Scaled $\langle\sigma^2(t)\rangle$ against scaled t, for the inclusion process, $d = 1$, on a complete graph. The solid line follows theoretical results (3.13). The increasing and decreasing sets of data have different initial conditions. For the decreasing set of data, all particles are initially all concentrated on one site. For the increasing set of data, all particles are multinomially distributed initially. Both sets of result converges to σ^2_∞, which is given by (3.15). The x and y-axis are scaled by $2dL$ and ρ^2 respectively. The y-axis is logged to show the exponential relaxation of the system, as denoted in (3.14).

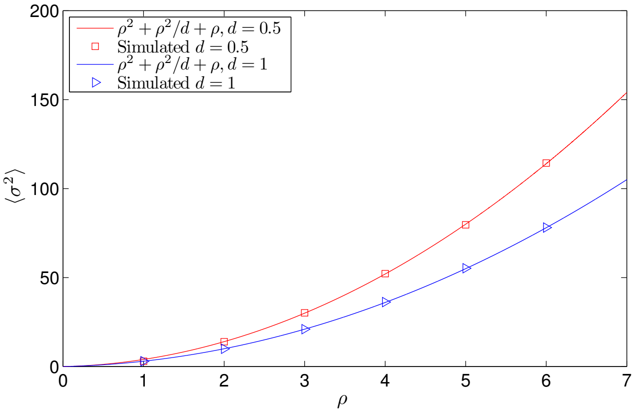

Figure 3.5: σ^2_∞ is plotted against ρ for the model with rates (2.40) on a totally asymmetric graph. Theoretical results are given by (3.15). This can be alternately explained using properties of stationary product measures in Sec. 2.2.3 and the derivation of (2.18). The error of the numerics are comparable to the marker sizes.

It should be noted that while the results for $\sigma^2(t)$ and the scaling of σ^2_∞ are derived based on mean-field approximations on a complete graph, the results in Fig. 3.5 are obtained from a totally asymmetric graph. The invariance in σ^2_∞ can be obtained from any homogeneous graphs as well. $\sigma^2(t)$ is accurate over different graphs but with a constant prefactor in time. This property is explained through the derivation of the time-dependent second moment solution of the generator equation on the Erdős-Rényi graph on the generator in (3.17).

Inclusion Process on Erdős-Rényi graphs

The Erdős-Rényi graph [71] is a method of generating random graphs with L and S_c being the number of nodes and probability of edges being included, respectively. The graph is therefore denoted by the notation $G(L, S_c)$. Upholding the mean-field approximation, the generator can be rewritten with a revision based on a modified adjacency matrix. Taking $(1/L)\sum_{x,y\in\Lambda} p(x,y) = S_c$, (3.7) is rewritten as

$$\mathcal{L}\eta_z^2 = S_c\sum_{x\in\Lambda}\eta_x(\eta_z+d)[(\eta_z+1)^2-\eta_z^2] + S_c\sum_{x\in\Lambda}\eta_z(\eta_x+d)[(\eta_z-1)^2-\eta_z^2]\,, \tag{3.16}$$

such that $S_c = 1$ denotes the complete graph. The derivation from (3.7) to (3.15) holds with a rescaling in time. Therefore in the Erdős-Rényi graph, (3.13) has a different equilibration time $t_{\text{eq}} = 1/2dLS_c$ but converges to the same second moment at steady state as the

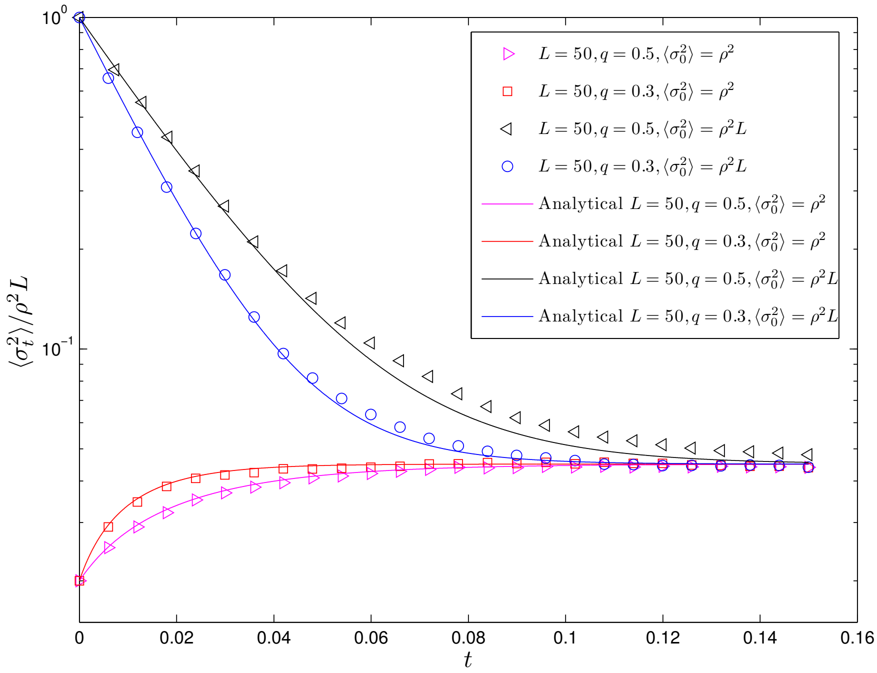

Figure 3.6: Scaled $\langle\sigma^2\rangle$ is plotted against t, for the inclusion process, on the Erdős-Rẽnyi graph. Numerical results with different S_c and different initial conditions are compared. The solid lines indicate theoretical results, which are given in (3.17).

complete graph case

$$\langle\sigma_t^2\rangle = \rho^2 + \frac{\rho^2}{d} + \rho + \left(\langle\sigma_0^2\rangle - \rho^2 - \frac{\rho^2}{d} - \rho\right) e^{-2dS_c t} \,. \tag{3.17}$$

Fig. 3.6 shows the second-moment for systems of different Erdős-Rẽnyi graphs being plotted against time. The generator of both the nearest neighbour symmetric and totally asymmetric cases can also be written in the form of (3.16). In the complete graph for large L, there are $L^2 - L \simeq L^2$ edges to be included. There are L connected edges for the totally asymmetric case, so $S_c^{\text{asym}} = L/L^2 = 1/L$. For the nearest neighbour symmetric case, there are $2L$ edges to be connected. This leads to $S_c^{\text{sym}} = 2L/L^2 = 2/L$.

3.3.2 Generator on models with rates (3.2) and (3.3)

Solving the generator for certain observables for the inclusion process can be relatively straightforward. However for models characterized by rates (3.2) and (3.3), where $\gamma > 1$, there are no clear methods to close the solution. For the model with rate (3.3), the generator for observable $f(\eta) = \eta_z^2$ for the complete graph case is written as

$$\mathcal{L}\eta_z^2 = \sum_{x\in\Lambda} \eta_x^{\gamma_1}(\eta_z^{\gamma_2} + d)[2\eta_z + 1] + \sum_{x\in\Lambda} \eta_z^{\gamma_1}(\eta_z^{\gamma_2} + d)[-2\eta_x + 1] , \tag{3.18}$$

where the combination of linear terms and summation of powers make mean-field solutions very difficult. For specific values of $\gamma_1 = \gamma_2 > 1$, there might be solutions as combination of higher moments, but there is no general solution. A heuristic approach is needed in order to characterize the formation of a condensate, as shown in Chapter 4.

3.4 Stationary measures for the explosive condensation model

In this section, we study the stationary product measures of the models with rate (3.2) and (3.3). These results are compared to the stationary product measures of the inclusion process.

3.4.1 Model with rates (3.2)

This model does not satisfy condition 3 in Theorem 2.2.1 for $\gamma_1 \neq \gamma_2$. Therefore, the general derivation is based on the assumption that the system satisfies detailed balance. Substituting the rates into the weights (2.12), the weights are written as

$$W^{\mathrm{wa}}(n) = \prod_{k=1}^{n} \frac{(k-1+d)^{\gamma_2}}{(k+d)^{\gamma_1} - d^{\gamma_1}} , \tag{3.19}$$

where notations with superscript “Wa” indicates they are derived for the model with rates (3.2). There is no explicit analytical solution for (3.19). Numerical solution for (3.19) can be obtained over certain parameter ranges, where physical measurements such as the second moment as depicted in (2.18) converges. The range of these parameters can be estimated by studying the asymptotic behaviour of $W(n)$. (3.19) is written in the logarithmic form

$$W^{\mathrm{wa}}(n) = \exp\left(\sum_{k=1}^{n} (\ln(k-1+d)^{\gamma_2}) - \ln[(k+d)^{\gamma_1} - d^{\gamma_1}]\right) . \tag{3.20}$$

Taking the k^{γ_2} and k^{γ_1} terms as

$$\ln(k-1+d)^{\gamma_2} = \ln(1 - 1/k + d/k)^{\gamma_2} + \ln k^{\gamma_2}$$

and

$$\ln[(k+d)^{\gamma_1} - d^{\gamma_1} = \ln[(1 + d/k)^{\gamma_1} - (d/k)^{\gamma_1}] + \ln k^{\gamma_1} ,$$

$W^{\mathrm{wa}}(n)$ in (3.20) can be written as

$$W^{\mathrm{wa}}(n) = \exp\left(\sum_{k=1}^{n} \ln\left(1+\frac{d-1}{k}\right)^{\gamma_2} - \ln\left[\left(1+\frac{d}{k}\right)^{\gamma_1} - \left(\frac{d}{k}\right)^{\gamma_1}\right] + (\gamma_2-\gamma_1)\ln k\right) . \tag{3.21}$$

For $n \to \infty$, there are three scenarios for how $W^{\mathrm{wa}}(n)$ scales, depending on γ_2 and γ_1. For $\gamma_2 \neq \gamma_1$, for large k the $\ln k$ term dominates, so $W^{\mathrm{wa}}(n)$ scales super-exponentially as

$$W^{\mathrm{wa}}(n) = \exp\left(\sum_{k=1}^{n}(\gamma_2-\gamma_1)\ln k\right) = (n!)^{\gamma_2-\gamma_1} \sim n^{n(\gamma_2-\gamma_1)} . \tag{3.22}$$

The physical meaning is that, γ_1 and γ_2 controls the non-linearity of the factorized hop rates for the giving and receiving terms respectively. For $\gamma_2 > \gamma_1$, large clusters will accumulate much faster than other clusters. Conversely, for $\gamma_1 > \gamma_2$, large clusters are discriminated and will give away particles much faster than receiving.

Whether $W^{\mathrm{wa}}(n)$ increases or decreases depends on whether $\gamma_2 > \gamma_1$ or $\gamma_1 > \gamma_2$. For $\gamma_1 > \gamma_2$, $W^{\mathrm{wa}}(n) \sim n^n$ increases exponentially and there is no convergence. For $\gamma_1 = \gamma_2 = \gamma$, the k^γ terms in (3.21) cancel out. Approximating $\ln(1 \pm \epsilon)^\gamma = \ln(1 \pm \gamma\epsilon) = \pm\gamma\epsilon$ for $\epsilon \to 0$ as $n \to \infty$, (3.21) is simplified as

$$W^{\mathrm{wa}}(n) = \exp\left(\sum_{k=1}^{n}\left(\frac{\gamma(d-1)}{k} - \gamma\frac{d}{k}\right)\right) = \exp\left(-\sum_{k=1}^{n}\frac{\gamma}{k}\right) \sim n^{-\gamma} . \tag{3.23}$$

Note that for $\gamma_1 \neq \gamma_2$, the derivation holds only for the symmetric graph as the condition in theorem 2.2.1 is not satisfied, while the case $\gamma_1 = \gamma_2$ can be applied also to translation invariant, asymmetric graphs. In summary, as $n > 0$, the three ranges for the scaling of $W^{\mathrm{wa}}(n)$ are

$$W^{\mathrm{wa}}(n \to \infty) \simeq \begin{cases} n^{(\gamma_2-\gamma_1)n} \to \infty & \text{if } \gamma_2 > \gamma_1 \\ n^{(\gamma_2-\gamma_1)n} \to 0 & \text{if } \gamma_1 > \gamma_2 \\ n^{-\gamma} & \text{if } \gamma_1 = \gamma_2 \end{cases} . \tag{3.24}$$

For the case when $\gamma_2 > \gamma_1$, there would be no finite moment solutions as W^{Wa} grows much faster than other terms in the moment generating function

$$S^q(\phi > 0) = \frac{1}{z(\phi)}\sum_{n=0}^{\infty}(\lambda\phi)^n n^q n^n \to \infty,$$

where S^q denotes the q^{th} moment of the system. In this regime, condensation is always the steady state for any finite fugacity ϕ. In the other extreme for $\gamma_1 > \gamma_2$, $W^{\mathrm{wa}} \to 0$. Therefore, there is no condensation for any range of fugacity.

The $\gamma_1 = \gamma_2$ case for the model with rates 3.2

The interesting case is for $\gamma_1 = \gamma_2 = \gamma$. In this special case, the model with rate (3.2) satisfies criterion 3 in Theorem (2.2.1). Therefore stationary product measures exist for its general case. From (2.16), the density for the case $\gamma_1 = \gamma_2$ is given by

$$\rho_{\mathrm{wa}}(\phi > 0) = \frac{1}{z(\phi)} \sum_{n=0}^{\infty} (\lambda\phi)^n n^{1-\gamma} = \begin{cases} < \infty & \text{for } 0 < \phi \leq 1, \gamma > 2 \\ \infty & \text{if } \phi > 1 \end{cases} . \tag{3.25}$$

For $\gamma > 2$, the density converges in the region $\phi \in [0, 1]$, and this corresponds to $\rho^{\mathrm{wa}} \in [0, \rho_c]$. There exists a critical density ρ_c, where for $\rho \leq \rho_c$, particles are distributed homogeneously on a fluid state. However, for $\rho > \rho_c$, which corresponds to $\phi > \phi_c = 1$, the system would split into a homogeneous fluid state and a condensate.

The second moment of the system can be calculated in a similar way, and we write

$$\sigma^2_{\mathrm{wa}}(\phi > 0) = \frac{1}{z(\phi)} \sum_{n=0}^{\infty} (\lambda\phi)^n n^{2-\gamma} = \begin{cases} < \infty & \text{for } 0 < \phi \leq 1, \gamma > 3 \\ \infty & \text{if } \phi > 1 \end{cases} , \tag{3.26}$$

where a finite σ^2 is obtainable only when $\gamma > 3$. The interesting case is when $\gamma \in [2, 3)$ for $\rho < \rho_c$. In this regime, condensation is not observed, but the second moment diverges. We collect the different ranges of critical fugacity in the three ranges of γ_1 and γ_2 mentioned above, and we write

$$\phi_c^{\mathrm{wa}} = \begin{cases} 0 & \text{for } \gamma_2 > \gamma_1 \\ \infty & \text{for } \gamma_1 > \gamma_2 \\ 1 & \text{for } \gamma_1 = \gamma_2 \end{cases} . \tag{3.27}$$

Similarly, the critical densities of each range can be written as

$$\rho_c^{\mathrm{wa}} = \begin{cases} 0 & \text{for } \gamma_2 > \gamma_1 \\ \infty & \text{for } \gamma_1 > \gamma_2 \\ \text{finite } \rho & \text{for } \gamma_1 = \gamma_2 \end{cases} . \tag{3.28}$$

Numerical simulation of $\rho(\phi)$ and $\sigma^2(\phi)$

$\rho_(\phi)$ and $\sigma^2(\phi)$ are calculated numerically from (2.14) and (2.17), as there are no clear analytical solutions. Fugacity is plotted in Fig. 3.7 . The monotonically increasing functions

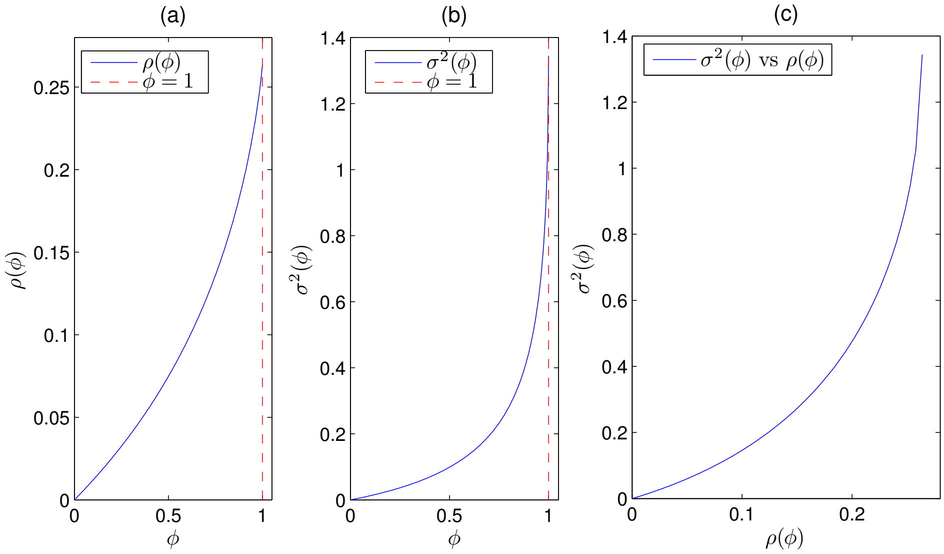

Figure 3.7: For $\gamma_1 = \gamma_2 = 5$, $d = 0.3$, for the model with rates (3.2) in the $\gamma_1 = \gamma_2$ case. (a) $\rho(\phi)$ is plotted against fugacity ϕ, (b) $\sigma^2(\phi)$ is plotted against ϕ, and (c) $\sigma^2(\phi)$ is plotted against $\rho(\phi)$. The red line indicates $\phi = \phi_c = 1$, as no finite moments converge for $\phi > 1$.

of $\rho(\phi)$ and $\sigma^2(\phi)$ are shown in the range $\phi \in [0, 1)$. For $\phi > 1$, the solution diverges.

We want to confirm the radius of convergence for $\rho(\phi)$ and $\sigma^2(\phi)$ in the regime of γ, for the case $\phi = 1$. This is not a straightforward problem, because there is no analytical solution to (3.25) and (3.26). The numerical approach is problematic in the sense that it always return a finite number as the solution, which does not capture cases of divergence. As one can see from (2.14) and (2.17), the numerical evaluation of $\rho(\phi)$ and $\sigma^2(\phi)$ requires the summation with an index n. To see convergence numerically, we use two different ranges of n in computing the density and second moment. If the solution converges, then there will be no difference in both numerical simulations. If the simulation with a larger range of n is significantly bigger than the simulation with the smaller range of n, then the solution diverges at that region.

We plot $\rho(\phi = 1)$ and $\sigma^2(\phi = 1)$ against γ 3.8. From (3.25) and (3.26), we estimated that $\rho(\phi = 1)$ and $\sigma^2(\phi = 1)$ would diverge at $\gamma \to 2$ and $\gamma \to 3$, respectively. This can be observed in the difference of the two numerical simulation in Fig. 3.8, where the ratio of the two simulations increases at $\gamma \to 2$ and $\gamma \to 3$, respectively.

3.4.2 Model with rates (3.3)

For the model that is characterized by rates (3.3), the weights $W^{\text{mod}}(n)$ are written as

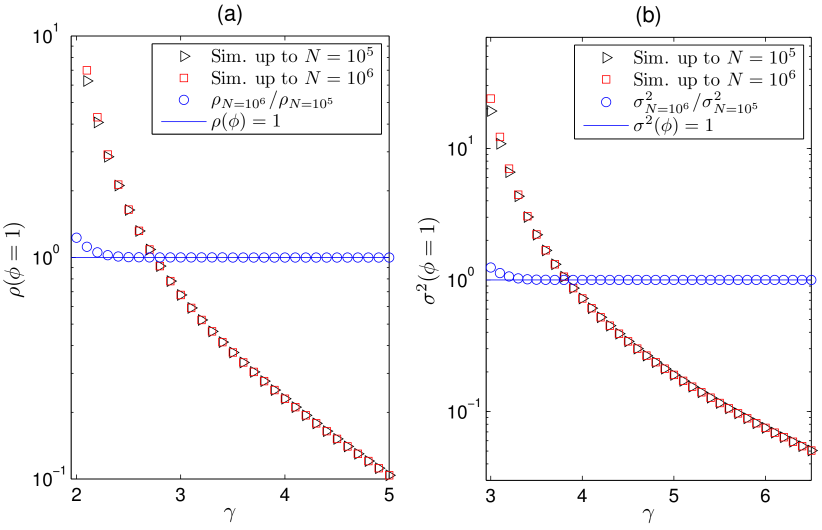

Figure 3.8: For $d = 0.4$ and the model with rates (3.2) for the $\gamma_1 = \gamma_2 = \gamma$ case. (a) $\rho(\phi = 1)$ is plotted against γ, and (b) $\sigma^2(\phi = 1)$ is plotted against γ. Black markers indicate when the solution is numerically obtained by evaluating (2.14) and (2.17) from $n = 0$ to $n = 10^5$, and the red marker is obtained by evaluating the respective partition functions from $n = 0$ to $n = 10^6$. The blue marker is the division of the two results. The blue marker will remain at 1 unless the numerical results diverge.

$$W^{\text{mod}}(n) = \prod_{k=1}^{n} \frac{(k-1)^{\gamma_2} + d}{k^{\gamma_1}} \,, \tag{3.29}$$

where quantities with superscript "mod" indicates they are derived for the model with rates (3.3). The model with rates (3.3) does not satisfy condition 3 in Theorem (2.2.1), stationary product measures only exist for symmetric graphs if $\gamma_1 \neq \gamma_2$. Similar to the derivation for the second moment and mean of the model characterized by rates (3.2) in Sec. 3.4.1, there is no clear analytical solution if (3.29) is substituted into (2.16) and (2.18). Instead, the scaling behaviour of $W^{\text{mod}}(n)$ is studied, and (3.29) is written in the logarithmic form

$$W^{\text{mod}}(n) = \exp\left(\sum_{k=1}^{n} \ln[(k-1)^{\gamma_2} + d] - \ln k^{\gamma_1} \right), \tag{3.30}$$

where k^{γ_2} and k^{γ_1} can be substituted out, and (3.30) can be written as

$$W^{\text{mod}}(n) = \exp\left(\sum_{k=1}^{n} \ln\left[\left(1 - \frac{1}{k}\right)^{\gamma_2} + \frac{d}{k^{\gamma_2}} \right] + \ln k^{\gamma_2} - \ln k^{\gamma_1} \right) . \tag{3.31}$$

Similar to the model with rate (3.2), distinctive results are obtained depending on the choice of γ_1 and γ_2. For $\gamma_1 \neq \gamma_2$, since $k \gg (1 - 1/k)$ for $k \to \infty$, (3.31) is simplified as

$$W^{\text{mod}}(n) = \exp\left(\sum_{k=1}^{n} (\gamma_2 - \gamma_1) \ln k \right) = (k!)^{(\gamma_2 - \gamma_1)} \simeq n^{n(\gamma_2 - \gamma_1)} \,, \tag{3.32}$$

which has the same scaling property to the previous example. For $\gamma_1 = \gamma_2$, and using the Taylor expansion $\ln(1 \pm \epsilon)^{\gamma} = \ln(1 \pm \gamma\epsilon) = \pm\gamma\epsilon$ for $\epsilon \to 0$ as $n \to \infty$. So (3.31) becomes

$$W^{\text{mod}}(n) = \exp\left(-\sum_{k=1}^{n} \frac{\gamma}{k} \right) \simeq \exp(C - \gamma \ln n) \sim n^{-\gamma} \,. \tag{3.33}$$

The scaling behaviour for $W(n)^{\text{mod}}$ is therefore the same as $W(n)^{\text{wa}}$ in (3.24). This means that the range for which ρ_c and σ_c^2 exists are the same as the scaling results from (3.25) to (3.28).

Condensation

For $\gamma_1 > \gamma_2$, no condensation is observed numerically. Condensation occurs for the $\gamma_2 > \gamma_1$ case. T_{SS} is plotted against L in Fig. 3.9. Similar to the results in the literature [6] or for $\gamma_1 = \gamma_2 > 2$, Fig. 3.9 implies $T_{\text{SS}} \to 0$ for $L \to \infty$.

For $\gamma_1 = \gamma_2$, and $\gamma > 2$, condensation is observed for a wide range of results. The analysis of the formation of condensate in the focus of Chapter 4. The critical densities

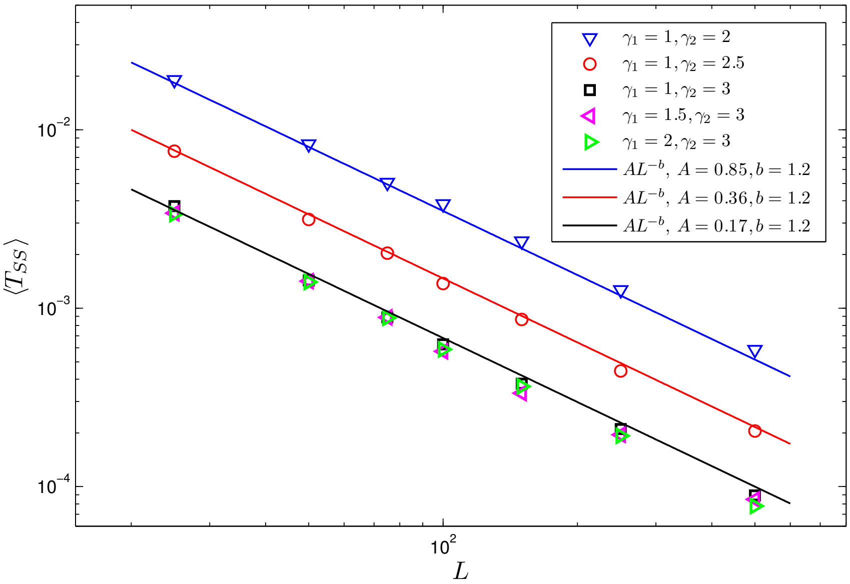

Figure 3.9: T_{SS} is plotted against L, $d = 0.5$, $\gamma_2 > \gamma_1$ for the model with rate (3.2). Condensation is observed in these cases. Scaling of $\langle T_{\mathrm{SS}} \rangle$ is mostly dependent on γ_2. γ_1 is non-significant to the speed to stationarity as $W(n) \sim n^n$.

and critical second moments of numerical results presented in Chapter 4 are presented in Appendix D.

Chapter 4

Microscopic analysis of condensation dynamics

In this Chapter we study the dynamics to stationarity for explosive condensation models, where above some critical density a fraction of all particles accumulates on a single cluster. This process is deemed "explosive", because the time to condensation goes to zero as $L \to \infty$. With an understanding of steady state properties for systems with stationary product measures (see Sec. 2.2.3), it should be noted that such methods do not provide a dynamic picture of how a system evolves to its steady state, nor does it provide time-dependent solutions to specific physical properties. An alternative approach to system dynamics at a microscopic level is considered, where different stages of dynamics are identified. The timescales of such stages are derived, and the interchange between these stages are explained. This leads to a comprehensive model that is based on cluster nucleation, coarsening and explosive condensation.

With this model, a coherent explanation for the time to reach steady state and the evolution of cluster is proposed, and is in line with the description of condensation. Consequently, a simpler derivation for $\langle T_{\text{SS}} \rangle$ for the totally asymmetric graph is presented, compared to the results by Waclaw and Evans [6, 59]. This model is also extended to the symmetric graph case, where a similar explosive condensation behaviour is observed as well as a novel non-explosive regime, depending on parameter values.

The cluster dynamics results in this Chapter lead to an improvement in numerical efficiencies. This revised method in simulation is used to obtain numerical results for models of size $L > 10^3$ with explosive condensation for the symmetric graph case, where previously it is difficult to obtain. Details of this numerical method, together with a discussion of its limitations can be found in Sec. 5. It is noted that this type of heuristic study has also been used in other IPS such as the zero-range process [36, 48, 24, 49, 5], the inclusion process [54] and partially in [6, 59].

Summary of Results

This Chapter is organised as follows. In Sec. 4.1 we provide an overview of two different types of condensation depending on system parameters, namely the explosive condensation and cluster coarsening. Before analysing the dynamics of these two types of condensation in depth, we first derive physical properties of cluster dynamics, which is outlined in Sec. 4.2. The early dynamics of the system are analysed in Sec. 4.3. Having understood cluster dynamics, we focus on the heuristic analysis of the two types of condensation mentioned above, using tools developed in Sec. 4.2 and Sec. 4.3. In Sec. 4.4, the dynamics of explosive condensation are studied, and this is followed by a detailed analysis of cluster coarsening in Sec. 4.5. Finally, we provide an analysis for the stability of clusters in Sec. 4.6.

In this chapter, results are organised by the successive stages in the condensation process. As there are two models and two graphs studied in this chapter, derivations of these cases are often presented under the same subsections, which might cause confusion to some readers. To alleviate the effort of trying to trace the derivation of a single set of results for a specific model and graph, we organise the key results of each case in Tables 4.1 - 4.3. These tables are organised as follows:

- Table 4.1 is a summary of results for cluster dynamics and is taken from Sec. 4.2.
- Table 4.2 is a summary of results for explosive condensation and is taken from Sec. 4.4. The explosive condensation is only observed for certain choices of γ, as indicated near the top of the table. This is one of the two types of condensations observed in this study. For an overview of the difference of these two types of condensation processes, see Sec. 4.1.
- Table 4.3 is a summary of results for cluster coarsening and is taken from Sec. 4.5. Note that cluster coarsening is only observed in symmetric systems for a certain parameter range, which will be elaborated in the said chapter in detail.

Simplifications in heuristic arguments

In the heuristic arguments used in this Chapter, simplifications are made based on presumed parameter ranges. We follow the range of parameters outlined in Sec. 3.2. Note that the regime for condensation to occur is $\gamma > 2$ for the totally asymmetric case and $\gamma > 3$ for the symmetric case, as suggested in Chapter 3. The same parameter range are used in this

General Model	$((\eta_x + d)^{\gamma_1} - d^{\gamma_1})(\eta_y + d)^{\gamma_2}$ (3.2)	$(\eta_x^{\gamma_1})(\eta_y^{\gamma_2} + d)$ (3.3)
Rates	$((\eta_x + d)^{\gamma} - d^{\gamma})(\eta_y + d)^{\gamma}$ (4.1)	$\eta_x^{\gamma}(\eta_y^{\gamma} + d)$ (4.2)
$\langle\tau_{\text{particle}}(\eta^{xy})\rangle$	$1/((\eta_x + d)^{\gamma} - d^{\gamma})(\eta_y^{\gamma} + d)$ (4.13)	$1/\eta_x^{\gamma}(\eta_y^{\gamma} + d)$ (4.3)
$\langle\tau_{\text{step}}\rangle_{\text{asym}}$	$(m)^{-\gamma}(d^{-\gamma} + C)$ (4.15)	$m^{-\gamma}(C' + d^{-1})$ (4.9)
$v(m)_{\text{asym}}$	$m^{\gamma}\frac{d^{\gamma}}{1+Cd^{\gamma}}$ (4.16)	$(dC' + 1)m^{\gamma}d^{-1}$ (4.10)
$\langle\tau_{\text{step}}\rangle_{\text{sym}}$	$m^{-\gamma+1}(d^{-\gamma} + C)$ (4.17)	$m^{-\gamma+1}(C' + d^{-1})$ (4.11)
$v(m)_{\text{sym}}$	$\frac{m^{\gamma-1}d^{\gamma}}{d^{\gamma}+1}$ (4.18)	$\frac{dm^{\gamma-1}}{1+C'd}$ (4.12)
Δm_{asym} Δm_{sym}	~ 0.5 (Page 58) $\sim m$ (Page 60)	

Table 4.1: Summary of results for cluster dynamics, which is a description of how clusters move and interact. These results can be found in Sec. 4.2.

Rates	Both (4.1) and (4.2)	
Graph	Totally Asymmetric	Symmetric
ECP observed	$\gamma > 2$	$\gamma > 3$
T_{Nu}	$\sim (\ln L)^{1-\gamma}\rho^{1-2\gamma}$ (4.22)	$\sim (\ln L)^{2-\gamma}\rho^{3-2\gamma}$ (4.23)
m_c	$\sim L^{1/\gamma}$ (4.26)	$\sim L^{2/(\gamma-1)}$ (4.25)
$\langle T_{\text{SS}}\rangle$	$\sim (\ln L)^{1-\gamma}$ (4.27)	$\sim (\ln L)^{2-\gamma}$ (4.28)
$m(t)$	$\left[m_0^{3-\gamma} + (3-\gamma)Ct\right]^{1/(3-\gamma)}$ (4.31)	$[C'\,(t_{\text{bu}} - t)]^{-\frac{1}{\gamma-3}}$ (4.32)
t_{bu}	$\sim L^{-\frac{(\gamma-1)}{\gamma}}$ (4.37)	$\sim L^{-\frac{2(\gamma-3)}{\gamma-1}}$ (4.33)

Table 4.2: Summary of results for the dynamics of explosive condensation. These results can be found in Sec. 4.4.

Rates	Both (4.1) and (4.2)	
Graph	Totally Asymmetric	Symmetric
Coarsening Condensation Observed	Not observed	$2 < \gamma < 3$
$\langle T_{\mathrm{SS}} \rangle$	NA	$L^{3-\gamma}$ (4.39)
$m(t)$	NA	$Ct^{\frac{1}{3-\gamma}}$ (4.50)
$\sigma^2(t)$	NA	$C(\rho - \rho_c)t^{\frac{1}{3-\gamma}}$ (4.52)

Table 4.3: Summary of results for cluster coarsening. These results can be found in Sec. 4.5.

Chapter. It should be reiterated that the diffusive parameter d is set to have size $d \sim O(1)$ throughout this Chapter, unless otherwise stated. The special case of vanishing diffusivity $d \to 0$ will be discussed as a separate case in Sec. 6.2.

4.1 Stages to stationarity

Models of interest

In Sec. 3.2, two models are introduced. The parameter regime for these two models, where phase transition is possible, are discussed in Sec. 3.4. We focus on the specific case of $\gamma = \gamma_1 = \gamma_2$ in this chapter, as this is the range where the stationary weights (3.24) and (3.31) do not scale super-exponentially. The rates for the models characterized in (3.2) and (3.3) are rewritten as

$$c(\eta_x, \eta_y) = ((\eta_x + d)^\gamma - d^\gamma)(\eta_y + d)^\gamma p(x, y), \tag{4.1}$$

and

$$c(\eta_x, \eta_y) = \eta_x^\gamma(\eta_y^\gamma + d)p(x, y)\ . \tag{4.2}$$

Recall that $p(x, y)$ represents the adjacency matrix, where only one-dimensional symmetric and totally asymmetric cases are studied in this chapter. For the numerical results presented, the corresponding critical densities ρ_c and second moment $\sigma^2_\infty(\phi = 1)$ can be found in Appendix D, which is derived by numerically evaluating (2.14) and (2.17).

It has been demonstrated in the previous chapter that if $\rho > \rho_c$, in a system with conserved number of particles, the system condenses. This leads to a finite critical second moment for $\gamma > 3$ and a finite critical density for all $\rho_c < \infty$ for all $\gamma > 2$. Depending on the parameter γ we observe two regimes:

1. **Explosive condensation is observed**: for symmetric systems with $\gamma > 3$ and asymmetric systems with $\gamma > 2$,
2. **Stationarity through cluster coarsening is observed for**: symmetric systems with $\gamma \in (2, 3)$, where the time to stationarity increases with L.

Making the differentiation between the above two paths to stationarity will be justified by timescale discussions in Sec. 4.3 - 4.5. For both cases, the process from initialization to reaching stationarity follows a multi-stage process, of which some of the stages have already been briefly mentioned in Figs. 3.1 and 3.2 in the previous chapter. In this section, we firstly provide a schematic overview of the dynamics to stationarity for different ranges of parameters and present a detailed description of each stage, with brief discussions on how the interchange between stages would occur.

Condensation on symmetric graph for $\gamma > 3$

The presence of successive stages for $\gamma > 3$ on a symmetric graph is illustrated in Fig. 4.1. In Fig. 4.1 $\sigma^2(t)$, which is a single value measurement that captures the distribution of the entire state as introduced in Eq (3.5), is plotted against arbitrary unit time t, from $t = 0$ to the system reaching stationarity, for $\gamma = 4.5$.

Fig. 4.1 is generated by Monte-Carlo methods using the Gillespie algorithm, where the details are illustrated in Chapter 5 and Appendix. B.1. This is just a typical example of explosive condensation for introductory purposes and a detailed explanation on how parameters affect the outcome will be presented in the following sections.

Only one instance of numerical simulation is shown in Fig. 4.1, as averaged results render the three stages less distinguishable (See numerical discussions in Sec. 5.2). As observed in Fig. 4.1 (b), the dynamics first go through a quick assimilation of particles during the initializing stage. This is followed by a relatively prolonged nucleation stage, as shown in Fig. 4.1 (a), where particles assimilate neighbours and occupation numbers change through direct interactions with immediate neighbours. This process is interrupted when some critical occupancy is reached. At this point a single cluster has gained sufficient mass to move across the entire lattice extremely rapidly, and swallows up even more mass in the process. This rapid condensation quickens as the mass of the condensate grows [6]. Note that the explosive condensation phase is reached directly from nucleation, as the critical occupancy number remains relatively small.

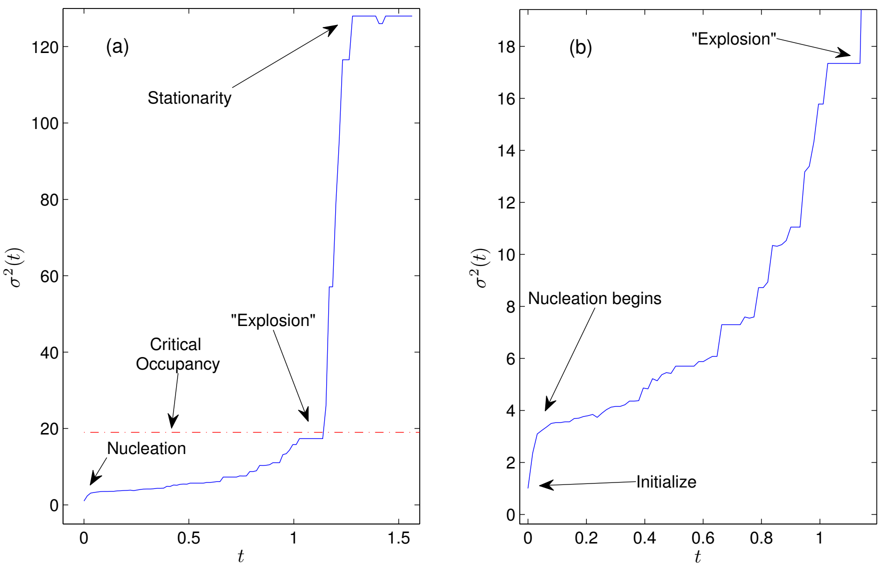

Figure 4.1: $\sigma^2(t)$ against t, for a single run, $\gamma = 4.5$, $\rho = 1$, $L = 128$, $d = 0.3$ for the model with rates (4.1) on a symmetric graph. (a) From initial stage up to condensation. The key stages are labelled. (b) The same plot highlighting early dynamics, up to the onset of explosion and the abrupt initializing phase is labelled.

Condensation on totally asymmetric graph for $\gamma > 2$

For the same model and parameters as the results in Fig. 4.1, but on a totally asymmetric graph, σ^2 is plotted in Fig. 4.2. The same three stages occur, although both the initializing stage and nucleation stage are even quicker, and the critical occupancy number is even smaller. Therefore T_{SS} occurs several magnitudes quicker than the same case on the symmetric graph. This can be qualitatively understood as clusters are able to cover the entire lattice with fewer steps on the totally asymmetric graph compared to its symmetric counterpart. In both Fig. 4.1 and Fig. 4.2, the dynamics are dominated by a prolonged period of cluster nucleation, which is succeeded by a sudden hike once a single cluster has gained sufficient mass to swallow up other fringe clusters quickly. Despite having a different adjacency matrix, the mechanism governing its dynamics to condensation is essentially the same as in the symmetric case.

Non-explosive condensation, symmetric graph for $\gamma \in (2, 3)$

The two previous cases shown in Fig. 4.1 and Fig. 4.2, both demonstrate explosive condensation. This is in contrast with models on a symmetric graph having parameters $\gamma \in (2, 3)$, for which σ^2 is plotted against t in Fig. 4.3. From the previous Chapter, it is understood

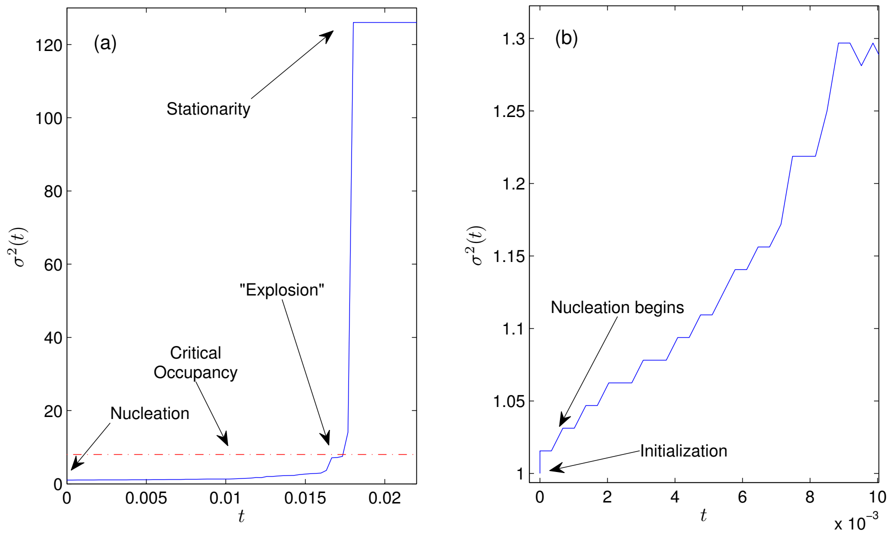

Figure 4.2: $\sigma^2(t)$ against t, for a single run, $\gamma = 4.5$, $\rho = 1$, $L = 128$, $d = 0.3$, for the model with rates (4.2) on a totally asymmetric graph. (a) shows simulation from initial stage up to condensation, and (b) shows the same plot highlighting early dynamics. The labels are the same as the ones used in Fig. 4.1.

that the condensed phase is formed with mass $(\rho - \rho_c)L$, where ρ_c can be numerically determined from (2.14). For the choice of γ in Fig. 4.3, $\rho_c = 2.65$ is considerably higher than the critical densities in the previous two examples. Therefore fluctuations towards reaching stationarity are much higher than Fig. 4.1 and Fig. 4.1, despite choosing a higher ρ.

As shown in Fig. 4.3, there is no explosive condensation observed. Contrary to the two previous examples with explosive condensation, the nucleation finishes extremely quickly, and the highest occupant of the system does not reach a critical occupancy m_c , as $m_c \gg L$ for $\gamma \in (2,3)$ (the estimation of m_c can be found in Sec. 4.4.1). Upon the completion of cluster nucleation, macroscopic clusters of size $O(L)$ are formed, and the dynamics is dictated by the interactions of roaming large clusters exchanging particles when they meet. This process of cluster coarsening is a visibly slower process than cluster nucleation, and the time scale to stationarity is therefore orders of magnitudes slower compared to the results obtained in Fig. 4.1 and Fig. 4.2. Eventually, stationarity is reached by cluster coarsening (c.f. Sec. 4.5).

Four stages to steady state

Collecting the observations in Fig. 4.1, to Fig. 4.3, four stages of the system dynamics are identified:

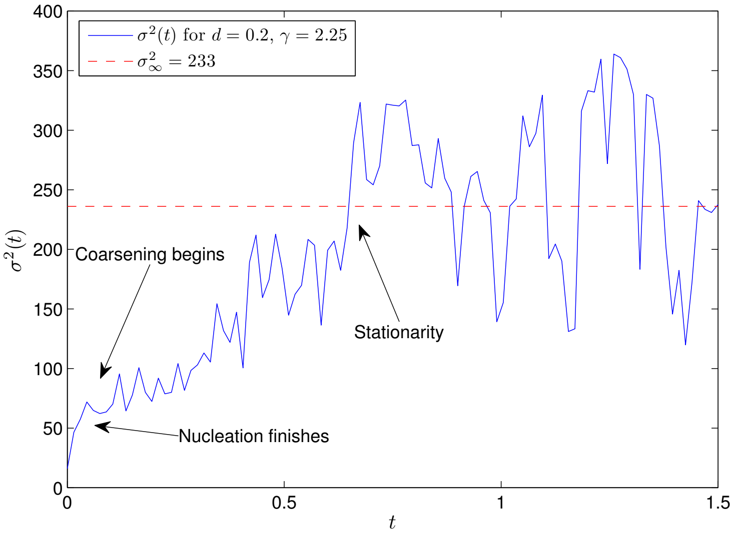

Figure 4.3: Second moment $\sigma^2(t)$ against t, for $\gamma = 2.25$, $\rho = 4$, $L = 128$, $d = 0.2$, symmetric graph, for a single run, for the model with rates (4.1). Nucleation quickly finishes, subsequently followed by prolonged periods of cluster coarsening. Stationarity is reached without forming an explosive condensate, contrary to the example presented in the $\gamma > 3$ cases in Fig. 4.1 and Fig. 4.2. σ^2_∞ is numerically computed with (2.17) and presented in Appendix D.

0. **Initialization**: At time $t = 0$, particles are arranged uniformly on the lattice such that $\mathbb{E}[\eta_x(t = 0)] = \rho$ for all $x \in \Lambda$. Typical cases we consider are to place each particle independently in a uniformly chosen lattice site, which leads to a multinomial distribution of the occupation numbers η_x, or we use the deterministic initial condition $\eta_x = \rho$ for integer densities ρ. Different types of initialization would not affect the scaling behaviour of subsequent stages, but might lead to different prefactors (see Sec. 4.3.1).

1. **Nucleation**: For supercritical densities $\rho > \rho_c$ the particles will quickly form clusters (see Sec. 4.3.2). This regime ends when the system either proceeds to:

   (a) Coarsening: for symmetric graph, $\gamma \in (2, 3)$, or

   (b) Explosive condensation: for symmetric graph $\gamma > 3$ and asymmetric cases $\gamma > 2$.

   Whether the system proceeds to coarsening or explosive condensation depends on whether some critical cluster size m_c is reached during cluster nucleation, as explained in Sec. 4.4.1.

2. **Coarsening**: For symmetric systems with $\gamma \in (2, 3)$ nucleation leads to a phase separated state, with several clusters of size $O(L)$ and a background configuration at density ρ_c. These clusters then move on the lattice (see Sec. 4.2.1) and interact when they get close by exchanging particles (see Sec. 4.2.2). Clusters may disappear, and all remaining clusters are stable and do not split into fragments (see Sec. 4.6). This drives a coarsening process which leads to a single condensate, and the time to stationarity in this case is increasing with the system size L (see Sec. 4.3 and Sec. 4.5).

3. **Explosive Condensation**: For symmetric systems with $\gamma > 3$ or asymmetric systems with $\gamma > 2$ there exists a critical cluster size $m_c \ll L$ which is subextensive on the lattice, such that a cluster of that size visits the whole lattice almost immediately (see Sec. 4.4). If one of the forming clusters reaches that size, nucleation ends and the largest cluster almost immediately absorbs all the excess mass in the system forming the condensate. The time to stationarity in this case decreases with the system size L (see Sec. 4.4.2).

4.2 Cluster dynamics

Before discussing the timescales of the respective stages to stationarity, it is important to understand more about cluster interactions. Multiplicative rates in models of explosive condensation lead to the quick formation of nucleates. For a system with relatively low background density, a nucleate will eventually deplete its immediate neighbouring sites of mass. Clusters of variable sizes roam around the lattice, and this occurs for both the coarsening stage or the explosive condensation stage. The heuristic arguments for the timescale of the various stages depend on the physical properties of clusters. Therefore, it is vital to understand how clusters move on the lattice, and how they interact with other clusters. Waclaw and Evans [6, 59] proposed a brief outline of cluster interactions for the totally asymmetric case. In this section, we extend this to the symmetric graphs as well. Together with the heuristic arguments in Sec. 4.3 - Sec. 4.6, we are able to describe fully how explosive and coarsening condensation takes place.

The arguments in this section are based on the assumption that clusters preserve mass until collision with other clusters, so each cluster can be treated as an independent entity. Clusters, however, can spontaneously "break-up" with a small probability. The ability for clusters to "break-up" is essential to the formation of a non-zero background density, although it occurs infrequently. For the complete portrayal of cluster dynamics, this section should be read in conjunction with the study on cluster stability in Sec. 4.6. This section will be divided into two parts, the transportation of clusters over empty lattices is discussed in Sec. 4.2.1, and the interactions between clusters are discussed in Sec. 4.2.2.

4.2.1 Cluster stepping time through empty lattice spaces

For a cluster with size $\eta_x = m$ surrounded by empty sites, let τ_{step} be the time it takes to move entirely to its neighbouring empty site. For the totally asymmetric case, $\eta_x \to 0$, $\eta_{x+1} \to m$. For the symmetric case, particles can move in either direction, so $\eta_{x+1} \to m$ or $\eta_{x-1} \to m$ while $\eta_x \to 0$.

Consider the totally asymmetric case, where a particle from a cluster of size m jumps into an empty site. If the destination site is also bordered by an empty site, then the rate for that one particle jumping further to the right is $\sim d^{\gamma}$, which is extremely small compared to the rate of other particles following from the cluster site, which is $\sim (m-1)^{\gamma}$. The movement of a cluster moving one step can be mapped into a totally asymmetric random walk, as illustrated in Fig. 4.4, and the total time for complete transportation of clusters by one lattice space can be computed by summing the average time for each successive step.

$\langle \tau_{\text{step}} \rangle$ for the model characterized by (4.2)

We now estimate the average time for a cluster to completely move one lattice space. Note that the choice of studying rates (4.2) ahead of rates (4.1) is an arbitrary one. Throughout this chapter, $\gamma > 2$ and $d \sim O(1) < 1$. For the model characterized by rates (4.2), the

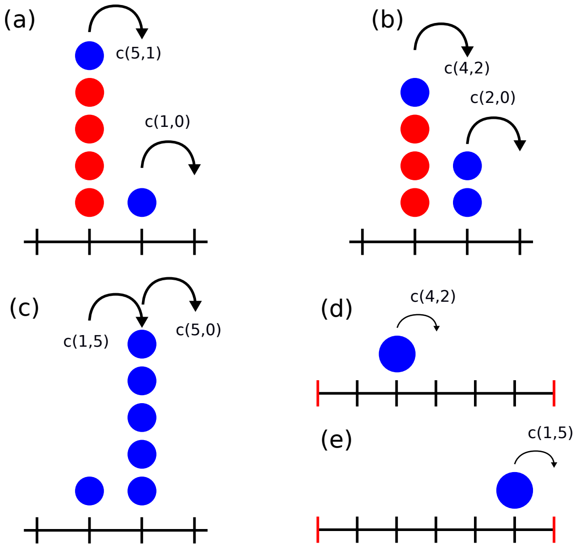

Figure 4.4: Mapping cluster movement in the totally asymmetric case to a one-dimensional asymmetric random walk. For a cluster with size $m = 6$, after the first step as shown in (a), the next jump comes from either arrows, such that the rates $c(5,1) \gg c(1,0)$. (b) for the next step, since $c(4,2) \gg c(2,0)$, the process continues up until (c), when the last particle moves to the right. This process is mapped to a one-dimensional asymmetric random walk, as (b) can be mapped to (d) and (c) mapped to (e).

average time for the movement of one particle from $x \to y$ is given by

$$\langle \tau_{\text{particle}}(\eta^{x\to y}) \rangle = \frac{1}{\eta_x^\gamma(\eta_y^\gamma + d)} \,. \tag{4.3}$$

In the totally asymmetric case, the time for the movement of one cluster is given by summing the successive time steps for a one-dimensional random walk, as illustrated in Fig. 4.4. For a cluster with mass m, the average time for a complete transportation of its own mass along one lattice space $\langle \tau_{\text{step}} \rangle$ is the summation of successive contributions of $\langle \tau_{\text{particle}}(\eta^{x\to y}) \rangle$,

$$\langle \tau_{\text{step}} \rangle = \sum_{i=0}^{m-1} \frac{1}{(m-i)^\gamma(i^\gamma + d)} \,, \tag{4.4}$$

Taking the time contribution of the first step at $i = 0$ separately to preserve symmetrically within the summation expression, we get

$$\langle \tau_{\text{step}} \rangle = \sum_{i=1}^{m-1} \frac{1}{m^{2\gamma}\left[1 - \frac{i}{m}\right]^\gamma \left[\left(\frac{i}{m}\right)^\gamma + \frac{d}{m^\gamma}\right]} + \frac{1}{dm^\gamma} \,. \tag{4.5}$$

Subsequently the Euler-Maclaurin equation is used, for $m \gg 1$, $i/m = x \rightarrow 0$ are regarded as small increments and can be integrated, where the limits are taken to be from $1/m$ to $1 - 1/m$, and noting that $dx = di/m$ we get

$$\langle \tau_{\text{step}} \rangle = \frac{1}{m^{2\gamma-1}} \int_{1/m}^{1-1/m} \frac{dx}{(1-x)^{\gamma}\left(x^{\gamma} + \frac{d}{m^{\gamma}}\right)} + \frac{1}{dm^{\gamma}} \,. \tag{4.6}$$

The term $d/m^{\gamma} \ll 1$ is of the same magnitude with x^{γ} in the lower bounds of the integral. For large m, the overall scaling property of the integral therefore resembles that of a symmetric function. Taking this assumption, we rewrite (4.6) as

$$\langle \tau_{\text{step}} \rangle = \frac{1}{m^{2\gamma-1}} \int_{1/m}^{1-1/m} \frac{dx}{(1-x)^{\gamma}\,(x^{\gamma})} + \frac{1}{dm^{\gamma}} \,. \tag{4.7}$$

Due to the symmetry of the integral in (4.7), it is integrated twice over in the range $x = 1/m$ and $x = 1/2$. Since the term $(1-x)^{-\gamma}$ is bounded above and below by a constant in the range $[1/m, 0.5]$, it does not affect the scaling with m. Introducing prefactor term C for the contributions of $(1-x)^{-\gamma}$, one obtains

$$\langle \tau_{\text{step}} \rangle \simeq \frac{2C}{m^{2\gamma-1}} \left[\frac{x^{-\gamma+1}}{-\gamma+1}\right]_{1/m}^{1/2} + \frac{1}{dm^{\gamma}} \simeq \frac{2Cm^{-3\gamma}}{\gamma-1} + m^{-\gamma}d^{-1} \tag{4.8}$$

for large m. Therefore the time for a whole cluster to transport to an adjacent site is of the same order as the time contributed by the first step. Letting $C' = 2Cm^{-2\gamma}/(\gamma-1)$, we write

$$\langle \tau_{\text{step}} \rangle = m^{-\gamma}(C' + d^{-1}) \,. \tag{4.9}$$

Note that the derivation of $\langle \tau_{\text{step}} \rangle$ is based on the assumption that d is a general constant of order 1. For $m \gg 1$, $C' \ll d$ and $\langle \tau_{\text{step}} \rangle$ scales as $m^{-\gamma}d^{-1}$. From (4.9), the rate or velocity $v(m)$ for an entire cluster to transport one step in an asymmetric graph will be

$$v(m)_{\text{asym}} = \frac{1}{\langle \tau_{\text{step}} \rangle} = (dC' + 1)m^{\gamma}d^{-1} \,. \tag{4.10}$$

Similarly to the totally asymmetric case, cluster movement in the symmetric case can be mapped to a one-dimensional random walk, as illustrated in Fig. 4.5. For the range of parameters used in this study, $c(a,b) \simeq c(b,a)$, where $a, b \geq 1$ and the rate for each step forwards has an approximately equal rate for trekking backwards, with a slight difference coming from the d dependent part of the rates. For a one-dimensional symmetric random walk, it takes an average of m tries to hit the right boundary before the left and complete the step. Therefore the velocity for an entire cluster to move can be estimated by dividing (4.8) by m. $\langle \tau_{\text{step}} \rangle_{\text{sym}}$ is therefore

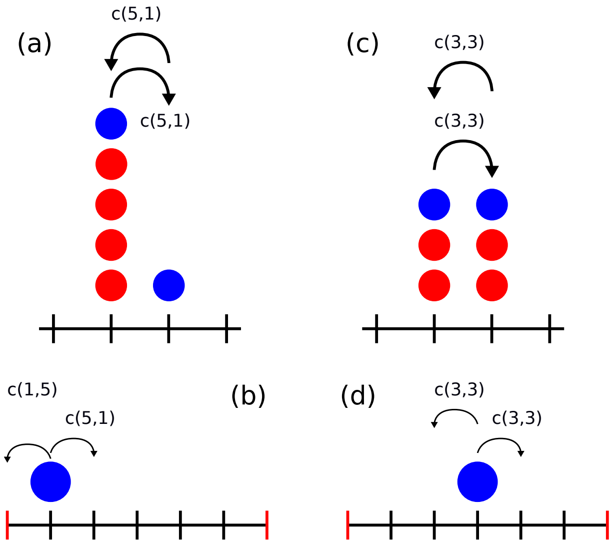

Figure 4.5: Mapping movement of cluster on symmetric one dimensional random walk for a cluster with size $m = 6$. (a) A particle jumped from the left hand side to an adjacent position on its right. For the next step, rates $c(5, 1)$ and rates $c(1, 5)$ dominate over the diffusive rates on the two ends. This process can be mapped into (b), for a single particle moves on a lattice of size $m + 1$. τ_{step} is therefore the time it takes for all particles to move from one site to either of its adjacent sites. In (c), particles going left and right have extremely similar rates for models characterized by rates (4.1) and (4.2). Therefore, the total time in reaching other sides can be regarded as a symmetric random walk as expressed in (b) and (d).

$$\langle \tau_{\text{step}} \rangle_{\text{sym}} = m^{-\gamma+1}(C' + d^{-1}) \,. \tag{4.11}$$

Therefore the rate for an entire cluster to move one step in a symmetrically connected graph is

$$v(m)_{\text{sym}} = \frac{dm^{\gamma-1}}{1 + C'd} \,, \tag{4.12}$$

with a different constant C as for the asymmetric case.

τ_{step} for the model characterized by rates (4.1)

The same approach can be used to determine τ_{step} for clusters moving on a lattice in Waclaw and Evans' model, which is characterized by rates (4.1). For the totally asymmetric case, the time $\langle \tau_{\text{particle}} \rangle$ it takes for a single particle to move to its adjacent site is written as

$$\langle \tau_{\text{particle}} \rangle = \frac{1}{((\eta_x + d)^\gamma - d^\gamma)(\eta_y^\gamma + d)} \,. \tag{4.13}$$

Similar to the derivations from (4.4) to (4.12), the time for entire clusters to move is estimated to be the summation of times for individual steps as illustrated in Fig. 4.4

$$\langle \tau_{\text{step}} \rangle = \sum_{i=0}^{m-1} \frac{1}{[(m-i+d)^{\gamma} - d^{\gamma}][i+d]^{\gamma}} \ , \tag{4.14}$$

which is simplified as

$$\langle \tau_{\text{step}} \rangle \simeq C \frac{m^{-3\gamma}}{\gamma - 1} + (md)^{-\gamma} \simeq (m)^{-\gamma}(d^{-\gamma} + C) \ . \tag{4.15}$$

Only d appears with the power γ instead of -1 as before, and the rate of cluster movement is

$$v(m)_{\text{asym}} = m^{\gamma} \frac{d^{\gamma}}{1 + Cd^{\gamma}} \ , \tag{4.16}$$

This result, together with τ_{step} for the model with rates characterized by (4.2) is compared to numerical results in Fig. 4.6. The results show for the range of parameters chosen, (4.9) and (4.15) are very good estimates for $\langle \tau_{\text{step}} \rangle$, and the constant C can be neglected for small values of d chosen. Similar to the argument in Fig. 4.4 which led to (4.12), the movement over a symmetrically connected graph is estimated by mapping cluster transportation between two sites to a one-dimensional random walk. This scales the velocity of the symmetrically connected graph by $1/m$ from (4.16). Time for one step is

$$\langle \tau_{\text{step}} \rangle = m^{-\gamma+1}(d^{-\gamma} + C) \ . \tag{4.17}$$

The rate is therefore

$$v(m)_{\text{sym}} = \frac{m^{\gamma-1} d^{\gamma}}{d^{\gamma} + 1} \ . \tag{4.18}$$

Similar to Fig. 4.6, the estimate for $\langle \tau_{\text{step}} \rangle$ for models in the symmetric graph is compared to numerical results in Fig. 4.7. For both graphs, the rate of cluster movement can be accurately computed. However, it should be noted that the movement of a cluster can sometimes result in a spontaneous disintegration, although this occurs at a much lower rate, as discussed in Sec. 4.6. The relatively simple scaling relationship and stability of clusters allow us to adapt the numerical methods. For large system sizes of $L \sim 10^3$, the numerical computation of cluster-cluster interaction can become very expensive, and this process of cluster movement can be simplified by replacing full simulations of steps by effective movement of complete clusters at certain crucial times of the numerical computation. This method has been implemented in the numerical simulation for $\langle T_{\text{SS}} \rangle$ later in this section, and its reliability is discussed in Chapter 5.

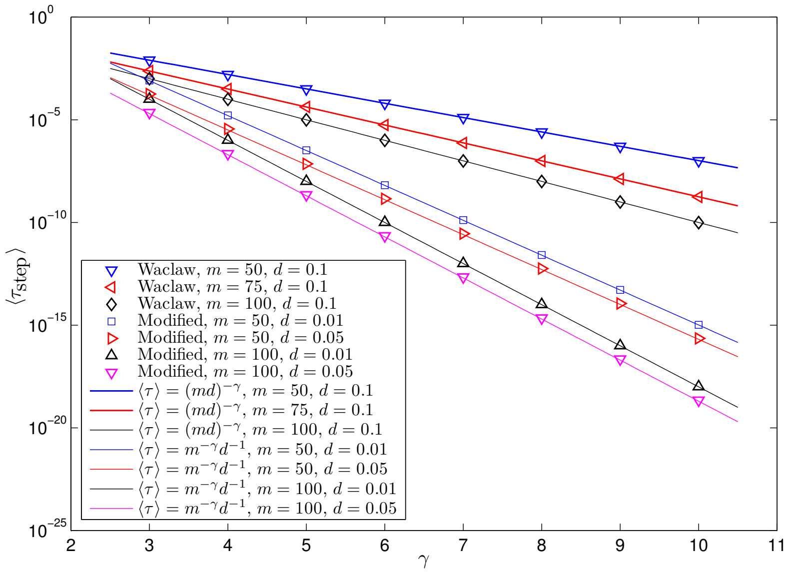

Figure 4.6: τ_{step} is plotted against γ for different cluster sizes m and diffusive term d. This is for the models with rates characterized by (4.2) and (4.1) in the totally asymmetric graph. Numerical results are generated with errors comparable to marker sizes. These are compared to the theoretical results given by (4.9) and (4.15), ignoring C since d is small enough

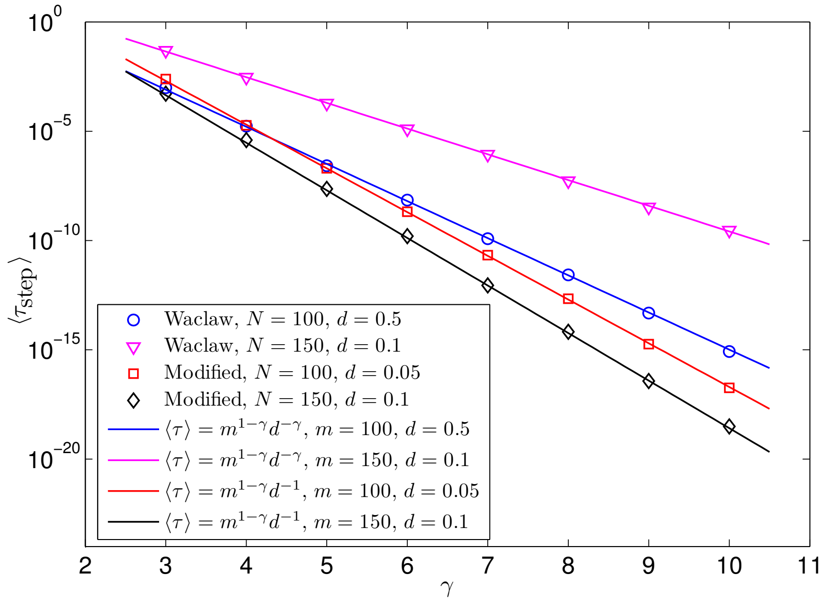

Figure 4.7: τ_{step} is plotted against γ for different cluster sizes m and diffusive term d. This is for the models with rates characterized by (4.2) and (4.1) in the symmetric graph. Numerical results are generated with errors comparable to marker sizes. These are compared to the theoretical results given by (4.11) and (4.17), again the constant C can be ignored.

4.2.2 Cluster Collision and transfer of mass Δm

"Collision" is the process when two clusters are separated by only one lattice site, a particle diffuses into the site between them. As a result, interactions take place over all three lattice sites and some mass Δm may be exchanged before the two clusters move away from each other. It is also possible for two clusters to merge into one cluster. When two clusters "collide", let m_1 be the mass of cluster with higher or equal mass entering the collision and m_2 is the mass of the other cluster. We define m_1' as the mass of the cluster with higher or equal mass after collision and m_2' is the mass of the other cluster with lower or equal mass after the collision. The exchange of mass is then

$$\Delta m(m_1, m_2) = m_1' - m_1 = -(m_2' - m_2)\,. \tag{4.19}$$

Total mass $M = m_1 + m_2 = m_1' + m_2'$ is a conserved quantity, such that if the two cluster merge, $m_1' = M$ and $m_2' = 0$.

Note that in this subsection, Δm is determined by inspecting the most probable interaction path. This is possible because the non-linear terms γ favours considerably the exchange of particles between clusters with higher mass. The models with rates (4.1) and (4.2) converges to the same most probable interaction path due to similar non-linearity terms. Therefore the following arguments are applicable for both the models (4.1) and (4.2).

Transfer of mass in the totally asymmetric setting

For the totally asymmetric case, Waclaw and Evans provides a schematic description and a measurement of $\Delta m \sim 0.4$ [6]. As part of the extension of the study in [6], Evans and Waclaw used a deterministic scattering derivation, in which Δm is estimated by continuous approximation, and zero mass transfer is predicted [59]. The discrepancies between the numerical measurement and continuous method of estimating Δm suggest that stochasticity is very important in cluster-cluster interactions. A subsequent numerical stochastic analysis suggests that, for large m_1 entering a collision, $\Delta m \sim 0.4 - 0.5$. We attempt to provide a qualitative argument, such that for $\gamma \gg 1$ and $m_1 \to \infty$, $\Delta m = 0.5$.

We first look at the schematic overview of cluster-cluster interaction in the totally asymmetric case. It has been observed that clusters entering a collision can leave an "imprint" of particles that is comparable to the size of the target smaller cluster in the totally asymmetric graph (see Fig. 3.1). This creates the illusion that the smaller cluster is moving backwards on a totally asymmetric graph, which is clearly not possible. An explanation of this is provided in [6], and we give an intuitive idea for the most probable interaction path in Fig. 4.8 largely following this.

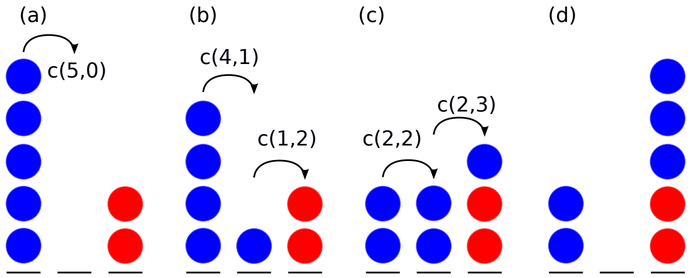

Figure 4.8: Collision of clusters in the totally asymmetric graph. Particles in blue make up the original mass of the cluster that enters collision, while red particles form the other cluster. In (a), a particle diffuses into the empty space and the configuration becomes (b). The rates for the adjacent sites with more particles are higher, therefore the next step is likely to be the step with rate $c(4, 1)$. Mass continues to flow from the first to the second site. This continues until the first and third lattice site contain approximately the same number of particles, such as the situation in (c). Subsequently, mass will flow from the second to third site until the second site is unoccupied. (d) This leaves the first site with around the same number of particles as the third site at the beginning of collision.

As clusters with higher mass travel faster, usually the cluster entering collision is the cluster with higher mass. For m_1 at lattice space $x = 1$ and m_2 at $x = 3$, and the first transfer made by a particle travelling from $x = 1$ to $x = 2$, then the occupancies for $\{x = 1, 2, 3\}$ will be

$$\{m_1, 0, m_2\} \to \{m_1 - 1, 1, m_2\} \, .$$

For both Waclaw and Evans' model and the model characterized by rates (4.2), assuming $m_1^\gamma > m_2^\gamma \gg d$, then the rates $c(\eta_1, \eta_2) > c(\eta_2, \eta_3)$ as long as occupancy $\eta_1 > \eta_3$. Particles continue to flow from site 1 to site 2 until $\eta_1 = \eta_3$, then occupancies for the three sites will be

$$\{m_1 - 1, 1, m_2\} \to \cdots \to \{m_2 + 1, m_1 - m_2 - 1, m_2\} \to \{m_2, m_1 - m_2, m_2\} \, . \tag{4.20}$$

From this point onwards, there are two positive scenarios, namely site 1 to site 2 or site 2 to site 3. For both the model with rate (4.1) and (4.2), these two scenarios occur with equal probabilities if $m_1^\gamma > m_2^\gamma \gg d$ holds. If this case does not hold, then either of the jumps would be slightly more probable depending on the relative sizes of m_1 and m_2. If $m_1 > 2m_2$, then the move from site 2 to site 3 is slightly more probable, and vice versa. However, for simplicity, we will assume that they are of equal probabilities.

In the first case $\{m_2, m_1 - m_2, m_2\} \to \{m_2 - 1, m_1 - m_2 + 1, m_2\}$ and then $c(\eta_2, \eta_3) >$

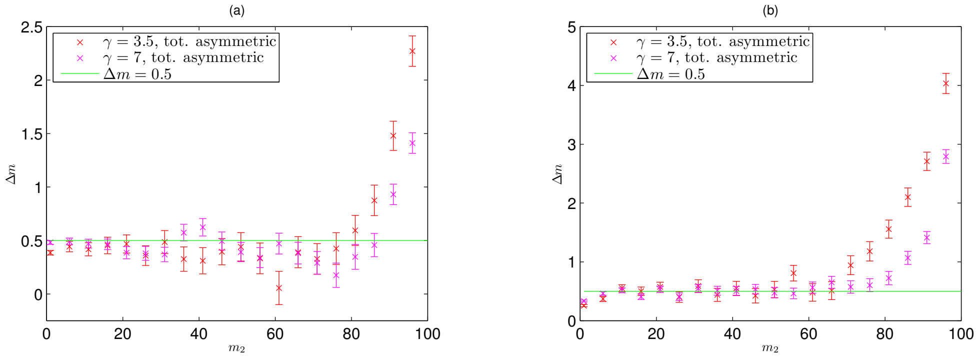

Figure 4.9: Δm against m_2, $m_1 = 100$, $d = 1$, for $\gamma = 3.5, 7$ for the totally asymmetric case. Solid line indicates the predicted $\Delta = 0.5$ for lower values of m_2. (a) Shows the model with rates (4.1) and (b) the model with rates (4.2).

$c(\eta_1, \eta_2)$. This means that eventually $\{m_2 - 1, m_1 - m_2 + 1, m_2\} \rightarrow \{m_2 - 1, 0, m_1 + 1\}$, and $\Delta m = 1$. Alternatively with equal probability, the exchange $\{m_2, m_1 - m_2, m_2\} \rightarrow \{m_2, m_1 - m_2 - 1, m_2 + 1\}$ can occur. Following the same arguments as before, this eventually leads to $\{m_2, 0, m_1\}$, where $\Delta m = 0$. Therefore, restricting to the two most probable interaction paths gives $\Delta m = 0.5$, providing $m_1^{\gamma} \gg d$. This is compared to numerical results in Fig. 4.9, where $\Delta m \sim 0.5$ is observed for $m_1 > m_2$. Note that for both scenarios, an imprint of $\sim m_2$ will be "left behind" creating an illusion of the smaller cluster travelling in the opposite direction.

However, this does not hold if $m_1 \approx m_2$ are approximately of equal size. Then many more interaction paths can exist, leading to an increase in Δm. Increasing γ would minimize this effect. The same relationship can be found for the model characterized by rates (4.2). This is observed in Fig. 4.10, where for most of the range of m_1 and m_2, $\Delta m \approx 0.5$. But when $m_1 \approx m_2$, the average particles exchanged are much less predictable.

Transfer of mass in the symmetric setting

The stochastic description of exchanging particles in the totally asymmetric case is based on the assumption that the larger cluster collides with the smaller cluster from behind, and exchanges some mass in the process. After this exchange, the larger cluster would continue to proceed forwards, without colliding with the smaller cluster unless it has visited every site in the lattice. But as $d \sim O(1)$ in this study, the separation of clusters after collisions is hard to determine on the symmetric setting. Therefore, even if the two clusters are separated by one lattice space after some exchange of mass, it is likely that the two clusters would quickly interact again due to their proximity. Therefore, the numerical measurement of Δm is obtained by measuring the difference in mass between the two clusters, when either of

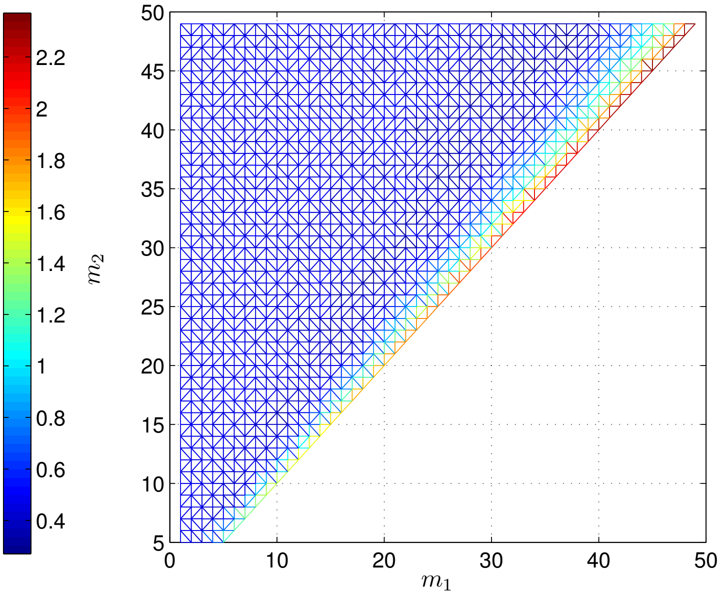

Figure 4.10: For $\gamma = 7$ and $d = 0.1$, totally asymmetric graph, for the model with rates (4.2), a heat graph of $\Delta m(m_1, m_2)$ is plotted against m_1 and m_2. $\Delta m(m_1, m_2) \simeq 0.5$ for a large area of m_1 and m_2, and this quickly increases towards $m_1 \approx m_2$.

the following two termination conditions are met. Firstly, if two clusters have drifted away for a large number of steps from each other. Secondly, if the two clusters have merged. The numerical results are shown in Fig. 4.11, where the average number of particles exchanged is proportional to the size of interacting clusters for $m_1 > m_2$. This is because there is a non-zero probability that the clusters merge, which leads to a linear behaviour.

The relationship shown in Fig. 4.11 is clearly linear when m_1 is significantly greater than m_2. The slight deviation from the linear relationship when $m_2 \to m_1$ is caused by the increased stochasticity in the interaction between the two clusters of similar mass. This is because, for $\gamma > 3$, slight changes in cluster mass result in drastic change in the speed of cluster movement. Even when m_1 is slightly greater than m_2, m_2 is relatively static compared to the quick moving m_1. However, if $m_2 \to m_1$, the speeds of the two clusters are of the same magnitude, and collisions are more frequent, yet the exact path of interaction is difficult to determine. The exact stochastic effect in the exchange of particles for two high mass clusters might be investigated in the future. However, as explained in Sec. 4.4 and 4.5, it is very rare to have m_1 and m_2 both being high in explosive dynamics. For coarsening dynamics, clusters of the same magnitude do coexist in the system, but very few clusters have very similar masses due to fluctuations in the initialisation process. Therefore, for the

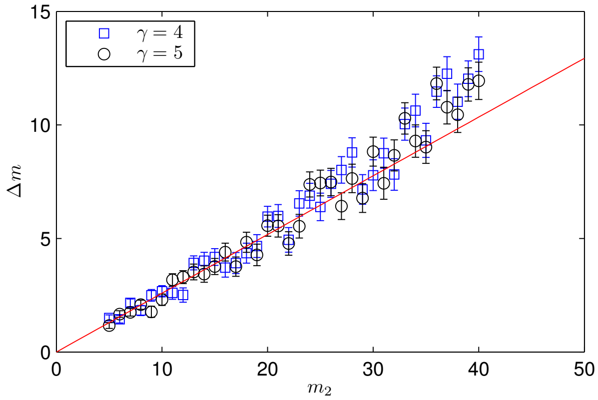

Figure 4.11: Δm against m_2 and $m_1 = 40$, on a symmetric graph, $d = 1$, for the model characterized by rates (4.1). The red line indicates a linear fit.

heuristic arguments throughout this chapter, the linear behaviour is upheld. This assumption leads to very accurate results in Sec. 4.4 and 4.5.

4.3 Cluster nucleation

As explained with schematic examples in Sec. 4.1, the rich variety of condensation behaviours for models with rates (4.1) and (4.2) are characterized by the timescale of the nucleation and subsequent explosion or coarsening stage. In this section, the microscopic properties of cluster nucleation are considered. This includes the initializing stage, microscopic description of the nucleation stage and terminating conditions for the nucleation stage. In these three cases, both symmetric and totally asymmetric cases for $\gamma > 2$ are studied. We estimate the time until a cluster reaches a certain size, and together with the terminating conditions dictating what subsequent stage the model would proceed to. Note that for the special case when diffusivity reaches zero $d \to 0$, results are provided separately in Sec. 6.2, and in this section $d = O(1)$ unless otherwise stated.

4.3.1 Effects of the initial distribution

Particle interaction starts when particles are distributed on the lattice either uniformly or multinomially. For uniform distribution with integer density ρ, occupancies at set up such that $\eta_x = \rho$, $\forall x \in \Lambda$ for $t = 0$. For particles distributed multinomially, $N = \rho L$ particles are each assigned to a lattice site chosen uniformly. Throughout this study, a uniform distribution is assumed for particle initialisation unless otherwise stated. The initial dynamics for uniformly distributed initial condition is illustrated in Fig. 4.12, which provides a

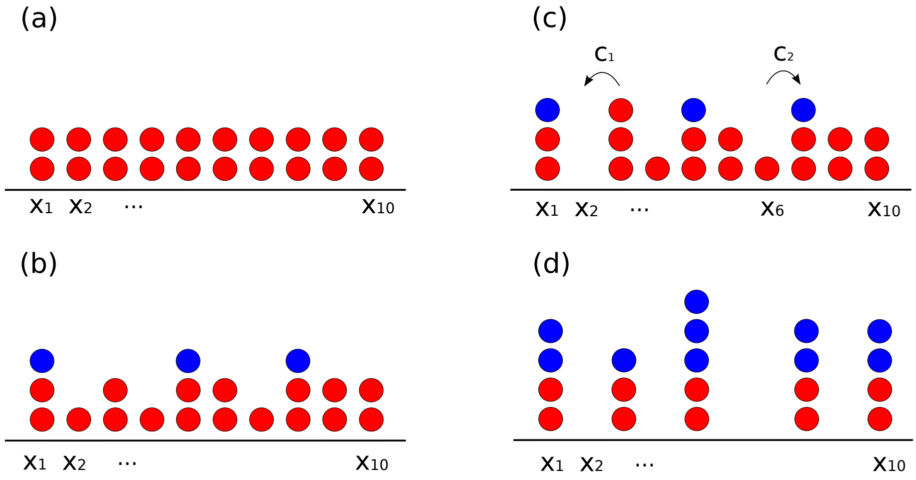

Figure 4.12: Initial dynamics for a symmetrically connected graph. (a) Particles are distributed uniformly with density $\rho = 2$, $L = 10$ at $t = 0$. The lattice is labelled accordingly. In the actual model, periodic boundary conditions are implemented but is omitted in this diagram for simplicity. (b) At a later stage, particles moved are labelled in blue. (c) Dynamics are bias towards interactions with non-zero receiving sites, such that rate $c_2 \gg c_1$. (d) Only for $d \to 0$, that the system evolves to a point where clusters are distinguished from one another separated by empty spaces locally. Particles that has been transported from $t = 0$ are labelled in blue. The absence of a background density in this case is supported by Table D that ρ_c becomes small as $d \to 0$.

schematic representation from the initial condition to the nucleation stage on the symmetric graph. Particles agglomerate around sites with higher occupancies during the early stages of nucleation, as shown in Fig. 4.12 (c).

For multinomial initial conditions, the occupation numbers at $t = 0$ fluctuate, which ensures a quicker initializing phase, as particles agglomerate faster on sites with higher occupancies due to the multiplicative nature of rates. For cases where $\rho > \rho_c$, a quicker nucleation time means that the system reaches critical mass faster (see Sec. 4.4). This contributes to a prefactor difference in the time scale, where the overall schematics of interaction is the same. Numerical results are presented in Fig. 4.13, where $\sigma^2(t)$ and configurations of early dynamics are plotted for the two different initial conditions in the symmetric case. The initial distribution of particles is irrelevant to the overall scaling of the dynamics, as the short time profile is similar. It should also be noted that in Fig. 4.13 (c) and (e), local lumps of nucleated particles coexist with clusters that have separated from the background. This corresponds to the prolonged period of nucleation illustrated in Fig. 4.12 (c), and a complete spatial separation of clusters only occurs for very small d as depicted in Fig. 4.12 (d).

The subsequent evolution of $\sigma^2(t)$ for the two different initial conditions is plotted

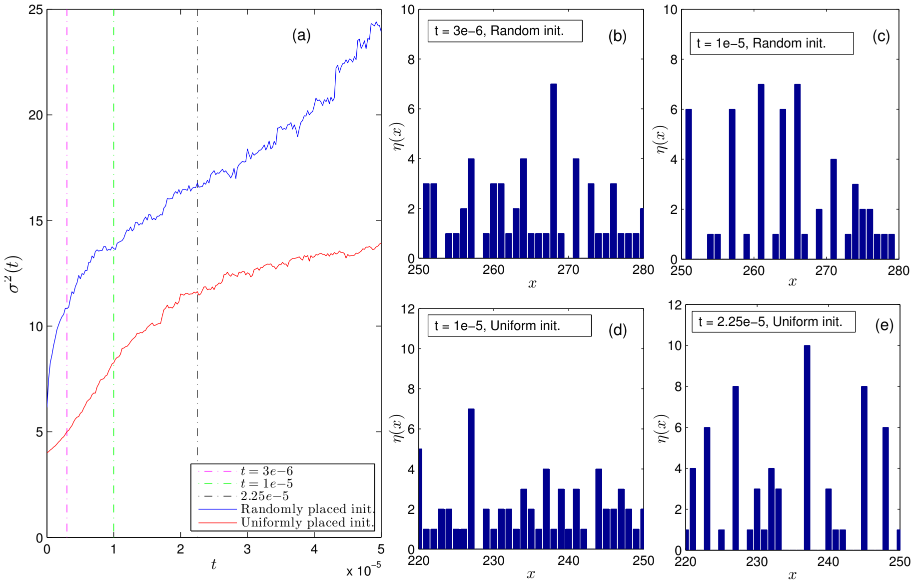

Figure 4.13: (a) $\sigma^2(t)$ against t for $\gamma = 5$, $\rho = 2$, $d = 1$, $L = 512$ and the model characterized by (4.1) for two different initial conditions on a symmetric graph. Only the early dynamics are presented. The blue and red line indicate random and uniform initial distributions, respectively. The vertical dashed lines represents the times where a section of the configurations is plotted in subsequent plots. Representative part of a configuration for multinomial initial condition at (b) $t = 3 \times 10^{-6}$ and (c) $t = 10^{-5}$. (d) Configuration for uniform initial conditions at $t = 10^{-5}$, and (e) $t = 2.25 \times 10^{-5}$.

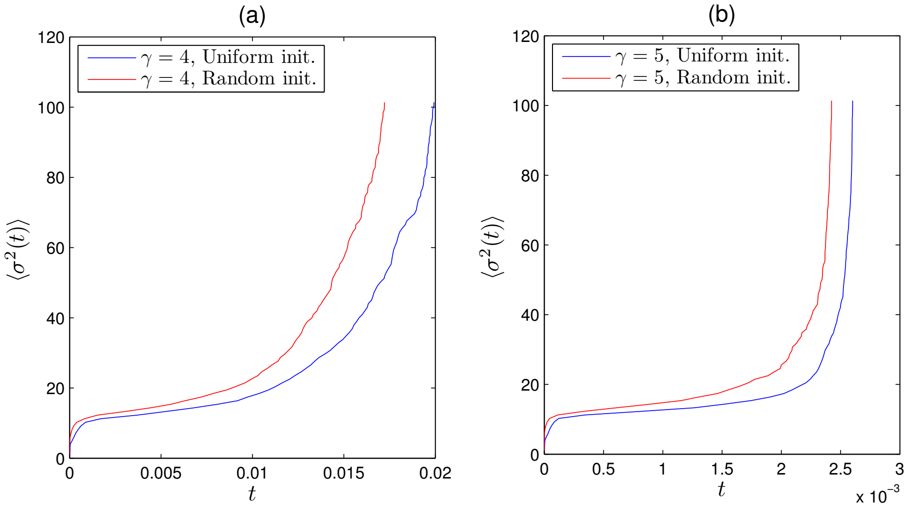

Figure 4.14: $\langle \sigma^2(t) \rangle$ against t, $d = 0.5$, $\rho = 2$, $L = 32$, for the model characterized by rates (4.2) on a symmetric graph. Different initial conditions are compared for (a) $\gamma = 4$ and (b) $\gamma = 5$.

in Fig. 4.14. As predicted, the system with multinomial initial condition reaches stationarity quicker. When dynamics are near stationarity, clusters of sizes $\sim O(L)$ are formed as the background is nearly depleted of particles. For higher γ, the dynamics would be increasingly dependent on the largest cluster only, as explained in Sec. 4.2. Therefore, the dynamics towards the end is similar between the two initial conditions in Fig. 4.14 (b) compared to Fig. 4.14 (a).

4.3.2 Growth of nucleating cluster

Schematic overview of nucleation dynamics

For both totally asymmetric and symmetric graphs, Fig. 4.15 illustrates the key characteristics of cluster nucleation. For $\rho > \rho_c$, clusters do not dissolve into the background, but instead grow in size as particles are concentrated on local sites since the multiplicative rates favour the agglomeration of particles. For the totally asymmetric case in Fig. 4.15 (a) and (b), as particles jump only in one direction, the system is likely to form larger nucleates, and interactions are more system-wide. But for the symmetric graph, more localized clusters would be formed, as illustrated in Fig. 4.15 (c) and (d). Despite seemingly different results due to nucleation, the scaling behaviour of the two graphs are principally the same. In the absence of a clear separation of timescales between nucleation and subsequent processes, one must look at the starting conditions for the explosive condensation and the coarsening

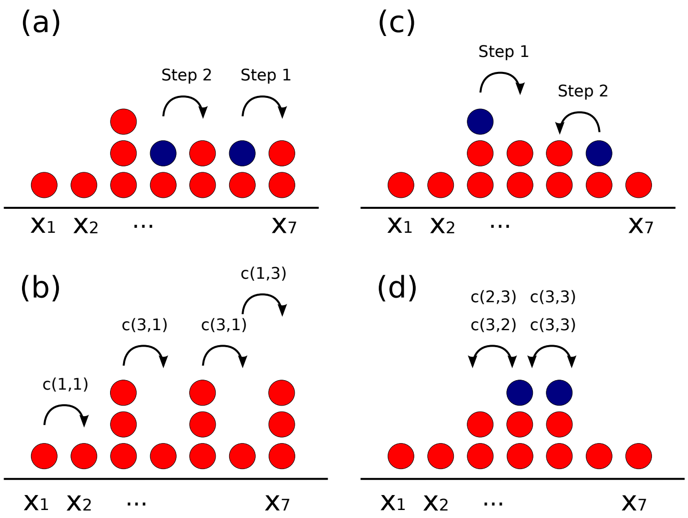

Figure 4.15: Schematic example of cluster nucleation for particle systems characterized by rates (4.1) and (4.2). Totally asymmetric graph is shown in (a) and (b), where particles are allowed to move in one direction only. From (a), in a hypothetical situation, particles are assumed to make the jumps “step 1” and “step 2”, and the configuration aftermath is shown in (b). In (b), the most likely jump is the two jumps that are marked $c(3, 1)$. Yet if site x_5 loses a particle, it is most likely that the site behind it x_4 would gain a particle from the move $\eta_3 \to \eta_4$. This means that nucleates of clusters can grow to relatively large piles and interactions typically span through a larger proportion of the cluster compared to the symmetric case. (c) shows the same configuration but on a symmetric graph, and particles are assumed to make the jumps “step 1” and “step 2”. In (d), the four most likely jumps are marked, and it is shown that particles are agglomerated along sites x_3 to x_5 until one site dominates. Nucleates are therefore relatively smaller in size, and interactions are more local.

regime to determine the completion of the nucleation regime.

Cluster nucleation begins as the particles are initialized and start to agglomerate locally as occupied sites are directly neighbouring each other. In condensation for the inclusion process as $d \to 0$, there is a clear separation of time scales for the termination of cluster nucleation, as nucleates simultaneously grow to the point where no particles are in the immediate vicinity of each other, or $\sum_{x\in\Lambda} \eta_x \eta_{x+1} = 0$ [54]. This does not occur for explosive condensation models with $d = O(1)$. The termination of the nucleation regime is defined loosely with the onset of subsequent processes, namely coarsening or explosion. Despite the ambiguity and the absence of separation of time scales, we can still estimate the approximate nucleation times. Note that the scaling analysis below is applicable to both models with rates (4.1) and (4.2).

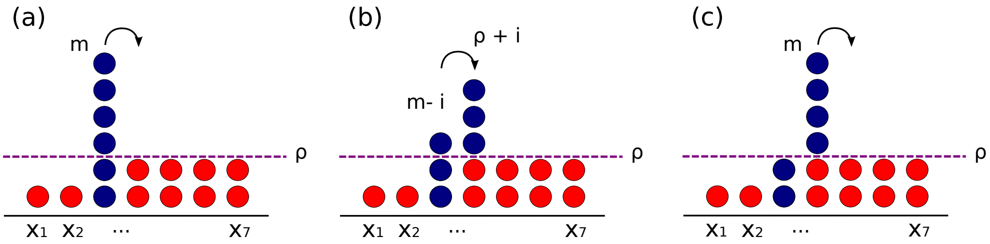

Figure 4.16: Estimating $\langle \tau_{\mathrm{Nu}}^{\mathrm{asym}} \rangle$. Cluster of m particles travels through a background of ρ uniformly distributed occupancies. Blue particles indicate the particles that make up a cluster at the beginning of the interactions. (a) at the start of the dynamics, for $m = 6$ and $\rho = 2$. (b) i is the number of successive steps as cluster m moves through the background. (c) Interaction finishes.

Nucleation in totally asymmetric graph

For particles distributed multinomially with large L, the distribution of particles is close to independent binomials, and the maximum of L independent random variables with Poisson tails is of order $\log L$ [72]. For particles distributed uniformly with ρ particles on each site, the same argument for the Poisson process that govern the initial particle motion on each site can apply. Since the number of events on each site up to time t is also Poisson distributed and independent for each cite, there will be a site on the lattice where in any finite small amount of time $\epsilon > 0$, a cluster of $O(\log L)$ particles is formed by these initial dynamics. Therefore due to fluctuations, after initialization the largest occupation number is of order $\rho \log L$. We follow the evolution of this fluctuation into a cluster, and estimate the time it takes to reach a size $M \gg \log L$. As explained in Sec. 4.2, the clusters move on the lattice with rate Cm^{γ}, where the constant C depends on the parameter of the model and the choice of model with rates (4.1) or (4.2). The derivation in Sec. 4.2 was for a cluster on an empty lattice, but it can be directly generalized to an environment with density ρ. The same computation applies and only the prefactor will change depending on the density. As a constant number of particles are gained through each interaction, the cluster will grow at rate proportional to m^{γ}. This process is illustrated in Fig. 4.16.

Particles nucleate to form clusters, which move along the asymmetric graph and gain particles linearly with each successive step, as explained in Sec. (4.2.2). The maximum occupancy after nucleation, which is also the cluster that is most likely to dominate, has mass that scales as $\rho \ln L$. The time to reach size M can be estimated by integrating successive times a cluster spends at size m until reaches M. These times are given by average inverse growth rates. The time for a cluster to grow from size $\rho \ln L$ to ϵM, where the constant $\epsilon \in [0, 1)$, is given by

$$T_{\mathrm{Nu}}^{\mathrm{asym}} = \int_{\rho \ln L}^{\epsilon M} \frac{1}{(m)^{\gamma}} dm \, . \tag{4.21}$$

Integration yields

$$T_{\mathrm{Nu}}^{\mathrm{asym}} = \frac{1}{1-\gamma} m^{1-\gamma} \Big|_{\rho \ln L}^{M} \sim (\ln L)^{1-\gamma} \rho^{1-2\gamma} \, . \tag{4.22}$$

Note that this timescale is in fact independent of the final size $M \gg \ln L$, due to the non-linearly increasing growth rate. This scaling behaviour applies for both the models that are characterized by rates (4.1) and (4.2) respectively. This is also very similar to the scaling behaviour obtained by Waclaw and Evans [6], which is explained in section Appendix. C. The similarity between Waclaw and Evans' result and $T_{\mathrm{Nu}}^{\mathrm{asym}}$ is because the dynamics in totally asymmetric graphs are dominated by the nucleation process.

Nucleation in a symmetric graph

Recalling the movement of particles on symmetric graph in Fig. 4.5 over empty sites, similar behaviour applies for clusters moving over a background with non-zero occupancies. The rate for a cluster to move one step over the background with non-zero occupancy for the model characterized by (4.1) or (4.2) is therefore given by $C\rho^{\gamma} m^{\gamma-1}$, where C again depends on d, γ and ρ.

The duration for nucleation $T_{\mathrm{Nu}}^{\mathrm{sym}}$ is the time required for a cluster of size $\rho \ln L$ to grow to ϵM

$$T_{\mathrm{Nu}}^{\mathrm{sym}} = \int_{\rho \ln L}^{\epsilon M} \frac{1}{\rho^{\gamma} m^{\gamma-1}} dm \sim (\ln L)^{2-\gamma} \rho^{3-2\gamma} \, . \tag{4.23}$$

Analogous to the totally asymmetric results (4.22), the scaling of cluster nucleation is strongly dependent on initial fluctuation and independent of the final size of M.

4.3.3 Termination of the nucleation process

As explained in greater detail in Sec. 4.4.4, for models with explosive condensation, the nucleation regime ends as the largest cluster grows to a critical size $m_c \ll L$ (see Sec. 4.4.1). Therefore both the symmetric and asymmetric nucleation would transit directly into explosive condensation regardless of whether nucleation results in larger or smaller nucleates for the different graphs. The exception is when $m_c \gg L$ for $\gamma \in (2, 3)$ on a symmetric graph, and this example will be explained in greater detail in Sec. 4.5.

4.4 Explosive condensation

After passing the nucleation stage, the dynamics proceed to either the explosive condensation stage or the prolonged process of cluster coarsening. In this section, the dynamics of explosive condensation is studied. Together with the timescale of the nucleation stage, $\langle T_{\mathrm{SS}} \rangle$ is estimated for both totally asymmetric and symmetric graphs and compared to numerical results. The time evolution of explosive condensation is also studied, and we compare this to the results obtained by Waclaw and Evans [6], which focus on explosive condensation for the totally asymmetric graph. This is extended to the symmetric graph in this study. The insights obtained from observations for various stages of the dynamics (Sec. 4.1) provides a framework towards a simpler argument for a similar scaling behaviour of $\langle T_{\mathrm{SS}} \rangle$ as Waclaw and Evans' results (see Appendix. C). It should be noted that the time-scale analysis of this subsection focuses on the large cluster relationship, and therefore are applicable for both rates (4.1) and (4.2).

4.4.1 Explosive condensation and critical occupancy

Explosion occurs when a single cluster reaches some critical occupancy number m_c, after which it is fast enough to move across the whole lattice at a fraction of the elapsed system time up to that point. As condensation occurs, the mass of the system quickly agglomerates to one cluster, while the mass in the background is still close to its initial distribution at the early stage of explosive condensation. To help us with understanding the basic key stages of cluster evolution, we study the configuration plots.

Stage by stage configuration plots for symmetric and totally asymmetric systems are illustrated in Fig. 4.17 and 4.18, respectively. The more detailed narration of these two figures are further elaborated in Sec. 4.4.2 and Sec. 4.4.3, respectively. The seemingly strange characteristic of the existence of background mass is captured in the configuration plot of Fig. 4.17 (e), (f) for the totally asymmetric case and Fig. 4.18 for the symmetric case.

From this point onwards, the cluster moves through mostly an empty lattice and follows the dynamics of cluster movement as explained in Sec. 4.2.1. Note that clusters on a symmetric graph are moving like a one-dimensional random walk, they have to make an average of L^2 steps to cover the entire lattice. In a non-stationary background and of density ρ, the critical occupancy m_c in the symmetric case is determined by a cluster with speed (4.12) making L^2 steps to cover the entire lattice in a time vanishing as $L \to \infty$,

$$\frac{L^2}{m_c^{\gamma-1}} \ll T_{\mathrm{SS}} \, . \tag{4.24}$$

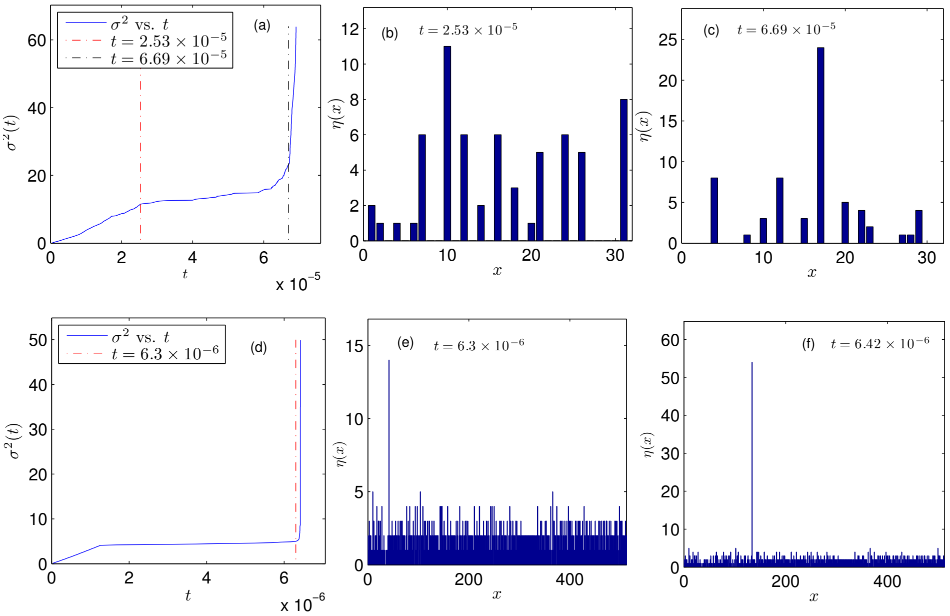

Figure 4.17: For totally asymmetric graph, model characterized by rates (4.1), $\gamma = 5$, $d = 0.1$ and $\rho = 2$. For (a), (b) and (c), $L = 32$, and $L = 512$ for (d), (e) and (f). (a) The second moment is plotted against time. Red and black lines corresponds to the instants during the interaction where the configuration is plotted on the right hand side. (b) Particles are concentrated into one cluster through nucleation, corresponding to the moment marked by the red line in (a). (c) The instant when explosive condensation is about to occur. A cluster reaches critical mass and is about to move into explosive condensation. (d) The second moment is plotted against time. The red line corresponds to the point when explosive condensation begins. The critical mass is reached while clusters are nucleating. (e) The time when a cluster is about to dominate through explosive condensation. (f) Shortly afterwards, the condensate continues to grow while the background is still populated by particles.

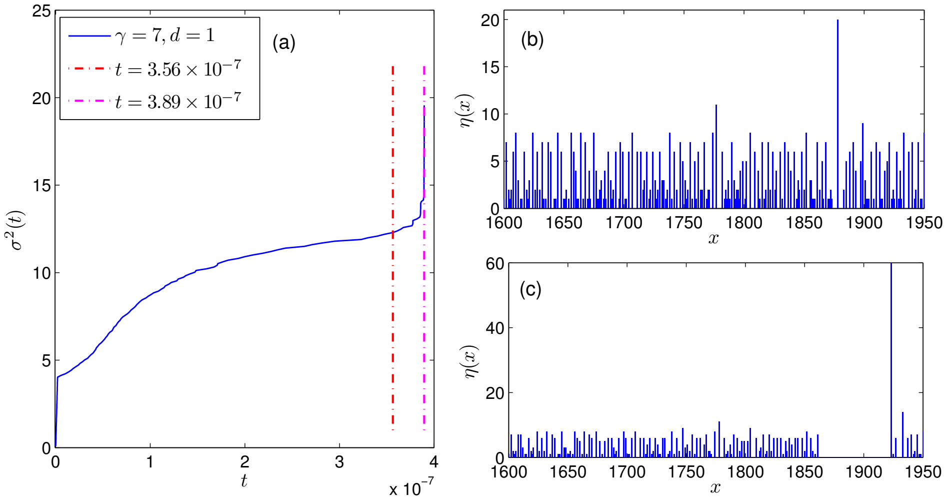

Figure 4.18: For the symmetric graph, $\gamma = 7$, $d = 1$, $\rho = 2$, $L = 2048$, model characterized by rates (4.2). (a) The second moment against time in the system is plotted. Explosive condensation is observed at around $t = 3.9 \times 10^{-7}$. Dashed lines represent the instances when the configuration of the system is given in (b) and (c). (b) Configuration of the system at $t = 3.56 \times 10^{-7}$ for a selected part of the lattice. (c) Configuration for $t = 3.89 \times 10^{-7}$ for the same part of the lattice.

We are interested in how m_c scales in the thermodynamic limit. The scaling relationship of m_c is taken by assuming $T_{\text{SS}} \sim O(1)$. Therefore, the size of critical mass m_c scales as

$$m_c \sim L^{2/(\gamma-1)} . \tag{4.25}$$

Recalling that $N \sim L$, this confirms that explosive condensation does not occur for $\gamma < 3$ on the symmetric graph, as the critical mass would be $m_c \gg N$. This means that the system will not have enough mass to reach critical mass. For the totally asymmetric case, going through similar arguments but for a cluster with speed (4.10) covering the entire lattice in L steps, m_c is given as

$$\frac{L}{m_c} \ll T_{\text{SS}} \Rightarrow m_c \sim L^{1/\gamma} . \tag{4.26}$$

For the totally asymmetric case, $m_c \ll L$ for $\gamma > 1$. So condensation, which occurs for $\gamma > 2$ (see. Sec. 3.4.1 and 3.4.2), is always explosive.

On symmetric graph, condensation is only explosive for $\gamma > 3$, which is schematically represented in Fig. 4.19. For $\gamma < 3$ however, m_c is not reached and coarsening dynamics takes over as nucleation finishes (as explained in Sec. 4.5).

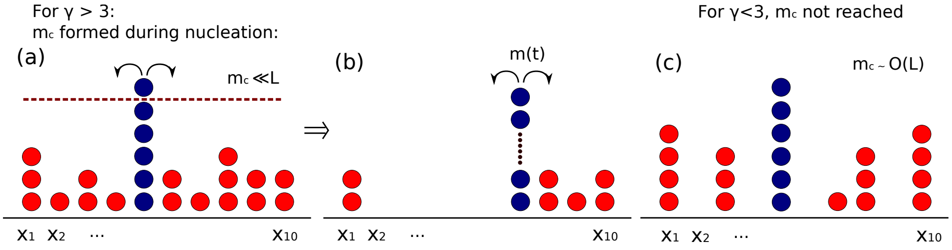

Figure 4.19: Schematic illustration for models that demonstrate explosive condensation on a symmetric graph. Blue particles indicate the cluster with the highest occupancies, while red particles indicate all other clusters. For $\gamma > 3$, (a) dashed line represents m_c depicted in (4.25), and is reached during the nucleation regime. This progresses to an explosive condensation, (b) where black dots represent particles in the cluster that are omitted for presentation purposes, such that the actual size of the cluster is much larger than the scale on this diagram. For $\gamma < 3$, m_c is not reached during the nucleation regime and clusters $\sim O(L)$ dominate until reaching stationarity.

4.4.2 $\langle T_{\rm SS} \rangle$ on a totally asymmetric graph

The scaling for the cluster nucleation $T^{\rm asym}_{\rm Nu} \sim (\ln L)^{1-\gamma}$ is given in (4.22). By (4.26), the explosive regime leads to stationarity in a time smaller than some small power of L. Therefore, $\langle T_{\rm SS} \rangle$ is asymptotically dominated by $T_{\rm nu}$, and we have

$$\langle T_{\rm SS} \rangle^{\rm asym} \sim (\ln L)^{1-\gamma} \,. \tag{4.27}$$

In the thermodynamic limit $L \to \infty$ and $\gamma > 2$, explosive condensation is observed, as $T_{\rm SS} \to 0$. The range of γ that demonstrates explosive condensation is different to the cases on a symmetric graph. To illustrate the microscopic difference between the totally asymmetric and the symmetric case, a schematic example is illustrated in Fig. 4.20 for $L = 32$ for $\gamma = 2.5$, $d = 1$ and $\rho = 2$, where the second moment is plotted against time with full particle configuration displayed for several different instances. The second moment of the stationary state is predicted by numerically evaluating (2.17).

Fig. 4.20 should be compared to Fig. 4.25, where the time for nucleation and coarsening can be observed, instead of undergoing explosive condensation. For the totally asymmetric case, in Fig. 4.20 (c), explosion dynamics begin to dominate after a relatively prolonged period of nucleation. In the symmetric case, however, for the same range of γ nucleation finishes quickly, followed by a prolonged period of coarsening. The scaling of $\langle T_{\rm SS} \rangle$ against L for the range $\gamma \in [2, 3)$ is plotted in Fig. 4.21. This result is included separately from the main results in Fig. 4.22 to highlight that explosive condensation is observed in the range $\gamma \in [2, 3)$ for the totally asymmetric case, while no explosion is observed in the symmetric case, as shown in Fig. 4.26.

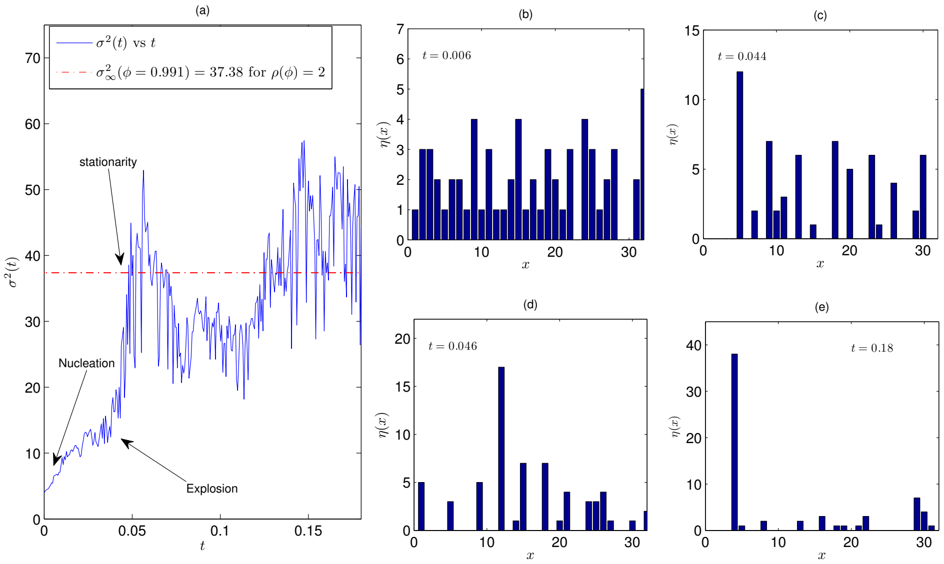

Figure 4.20: For totally asymmetric graph, $\gamma = 2.5$, $d = 1$, $\rho = 2$, model characterized by rates (4.1). (a) Second moment versus time is plotted. Red dotted line indicates the second moment of the steady state, which is predicted by numerically evaluating (2.17). Note that for $\gamma > 3$, σ^2 diverges, which leads to large fluctuations. The configuration at different instances are shown from (b) to (e). (b) Initializing and nucleation. (c) Nucleation continues, and one cluster is beginning to dominate. (d) Approximately the time when m_c is reached by the largest cluster. (e) Steady state: explosive condensation ensures that the largest clusters dominates, quickly reaching the steady state with the background density.

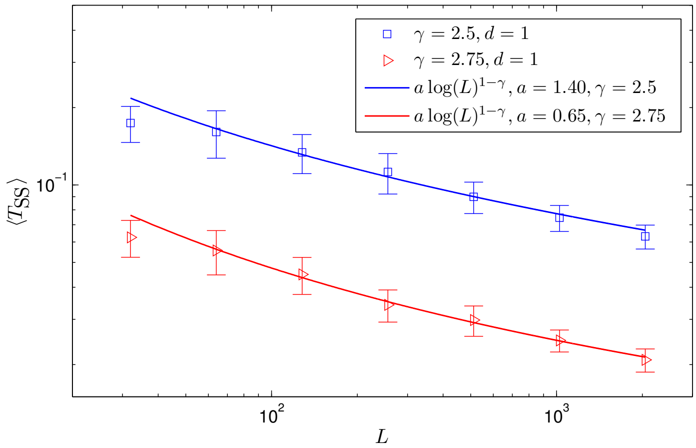

Figure 4.21: $\langle T_{\mathrm{SS}} \rangle$ is plotted against L for $\gamma = 2.5$ (blue) and $\gamma = 2.75$ (red), $d = 1$, $\rho = 2$, totally asymmetric graph for the model characterized by rates (4.1). Theoretical results (4.27) for $\gamma = 2.5$ and $\gamma = 2.75$ are plotted as the solid line.

The evolution of $\sigma^2(t)$ is compared for $\gamma = 5$ on the totally asymmetric graph in Fig. 4.17, with two different L, alongside with configuration plots at different times during the interaction. For Fig. 4.17 (a) - (c), notice that nucleation is approaching the end relatively earlier on, as the overall mass in the system is a limiting factor to reach m_0 in small systems. This is compared to the $L = 512$ case, for a higher system size, nucleation dynamics dominates up to the point of a single cluster reaches the critical mass. This is illustrated in Fig. 4.17 (d) - (f).

The scaling of $\langle T_{\mathrm{SS}} \rangle$ on the totally asymmetric graph for $\gamma > 3$ is presented in Fig. 4.22, where the theoretical results are given by (4.27).

4.4.3 $\langle T_{\mathrm{SS}} \rangle$ on the symmetric graph

The scaling for the cluster nucleation is $T_{\mathrm{Nu}}^{\mathrm{sym}} \sim (\ln L)^{2-\gamma}$. Since for $\gamma > 3$ the critical cluster size $m_0 \ll L$, this again dominates the time to stationarity and

$$\langle T_{\mathrm{SS}} \rangle_{\gamma>3}^{\mathrm{sym}} \sim (\ln L)^{2-\gamma} \,. \tag{4.28}$$

The second moment against time for $\gamma = 7$, $L = 2048$ for the model characterized by rates (4.2) on a symmetric graph is plotted in Fig. 4.18 (a). Configurations of this simulation are shown in Fig. 4.18 (b) and (c).

For Fig. 4.18 (a), the simulation has been terminated before reaching stationarity, as it has demonstrated that the highest occupancy has reached the critical mass m_c, as made clear in the subsequent configuration graphs. Explosive condensation is observed at around 3.9×10^{-7}, and the configuration is plotted at two instances prior to condensation. In Fig. 4.18 (b), the nucleation process dominates, and a cluster with size ~ 20 is observed to be higher than most other occupancies. In Fig. 4.18 (c), the cluster previously observed has gained sufficient mass to dominate and swallows clusters in its vicinity. Note that the configuration of the system is largely unchanged otherwise; the scaling of $\langle T_{\mathrm{SS}} \rangle$ on the symmetric graph for $\gamma > 3$ is presented in Fig. 4.23.

4.4.4 $\sigma^2(t)$ for explosive condensation

Having confirmed numerical results for $\langle T_{\mathrm{SS}} \rangle$ for models that demonstrate explosive condensation, we now look at the time-dependent evolution of the system. The evolution of $\sigma^2(t)$ is considered for $\gamma > 3$ in the symmetric graph case. For the models characterized by rates (4.1) and (4.2), the rate D of gaining particles from an exchange is given by

$$D = m^{\gamma-1} C(d, \rho) \sim m^{\gamma-1} \,, \tag{4.29}$$

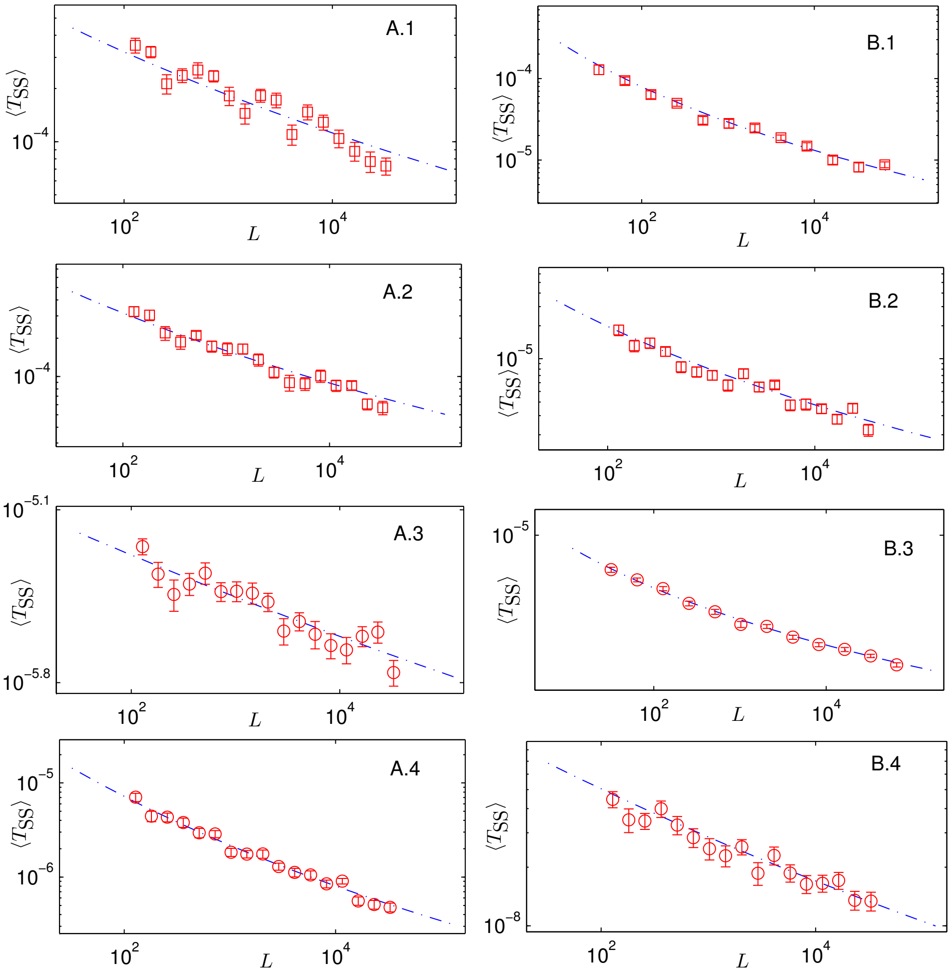

Figure 4.22: Plots of T_{SS} against L for totally asymmetric graphs. Columns A-B: For models characterized by rates (4.1) and (4.2) respectively. Rows 1-4: $\gamma = 5$ $d = 0.1$, $\gamma = 5$ $d = 1$, $\gamma = 7$ $d = 0.1$ and $\gamma = 7$ $d = 1$. Error is comparable to the size of markers if not indicated. Dashed lines are corresponding theoretical results given by (4.27).

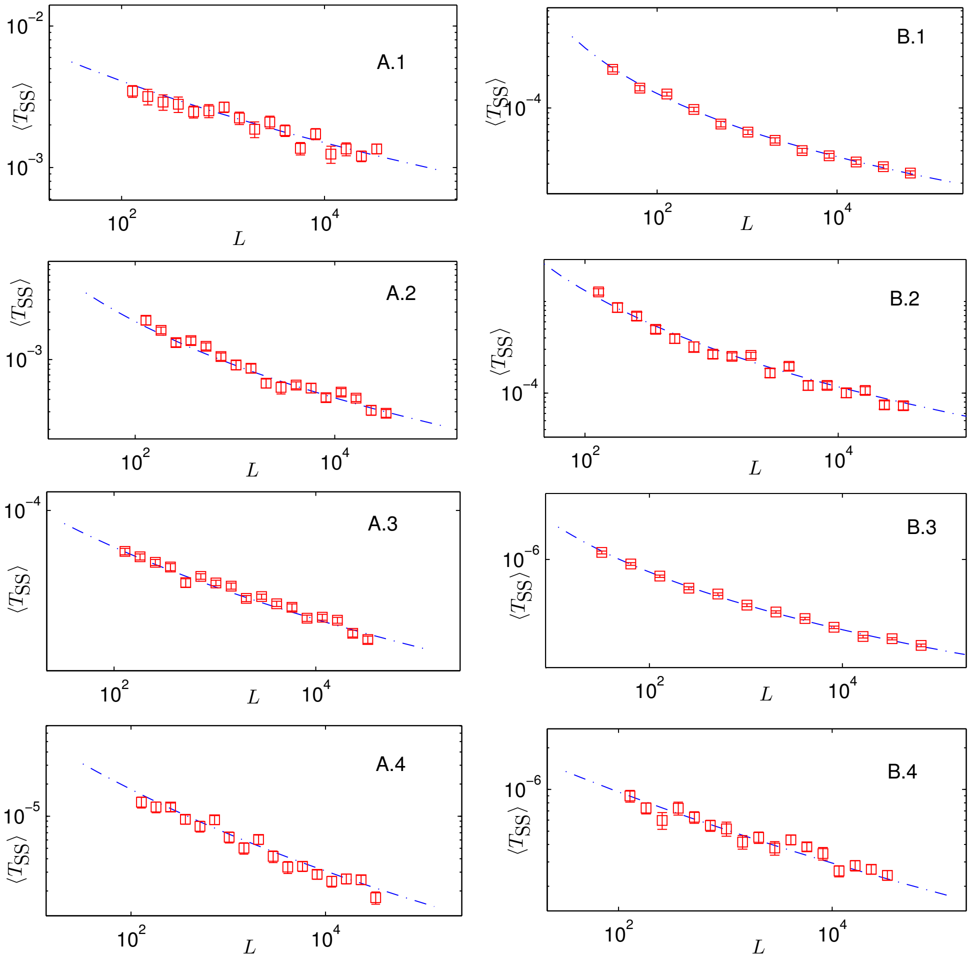

Figure 4.23: Plots of T_{SS} against L for symmetric graphs. Columns A-B: For models characterized by rates (4.1) and (4.2) respectively. Rows 1-4: $\gamma = 5$, $d = 0.1$, $\gamma = 5$, $d = 1$, $\gamma = 7$, $d = 0.1$ and $\gamma = 7$, $d = 1$. Error is comparable to the size of markers if not indicated. Dashed lines are corresponding theoretical results given by (4.28).

where $m^{\gamma-1}$ on the left hand side is the step rate of the cluster derivation in Sec. 4.2. Note that this is an estimation of D for early stages of nucleation, where $\langle \eta_{x\pm 1}^{\gamma} \rangle \sim O(1)$, as opposed to the stationary state where this would diverge. The critical cluster size was derived in (4.25) to be $m_c = L^{2/(\gamma-1)}$, which is consistent with (4.29). The evolution of the occupancy for a typical cluster is given by the differential equation

$$\frac{d}{dt}m(t) = \frac{D}{m(t)} = Cm^{\gamma-2}(t) \,, \tag{4.30}$$

which can be solved to give

$$m(t) = \left[m_0^{3-\gamma} + (3-\gamma)Ct\right]^{1/(3-\gamma)} \,. \tag{4.31}$$

Since $\gamma > 3$, this leads to the system having a finite "blow-up time" $t_{\mathrm{bu}} < \infty$, where as $t \to t_{\mathrm{bu}}$ $m(t) \to \infty$. Writing the dynamics in terms of t_{bu} gives

$$m(t) = \left[C' \left(t_{\mathrm{bu}} - t\right)\right]^{-\frac{1}{\gamma-3}} \,, \tag{4.32}$$

where $C' = (\gamma - 3)C$ and $t_{\mathrm{bu}} = m_0^{3-\gamma}/(C(\gamma - 3))$. So the time required for a cluster to "blow-up" once reaching m_c is given by setting $m(0) = m_c$, and substituting (4.30) leads to

$$t_{\mathrm{bu}} \sim L^{-\frac{2(\gamma-3)}{\gamma-1}} \searrow 0 \,. \tag{4.33}$$

So for $\gamma > 3$ and increasing system sizes, the blow-up time vanishes, which is consistent with explosive condensation. Note that $m(t)$ can never reach infinity due to finite size and saturates at $m(t) = (\rho - \rho_c)L$. Since t_{bu} vanishes as a power with the system size L, $\langle T_{\mathrm{SS}} \rangle$ is dominated by initial dynamics to reach m_c, which is $\sim (\ln L)^{2-\gamma}$. This is consistent with the timescale analysis in (4.23). The time evolution of the model that displays explosive condensation is compared to numerical results in Fig. 4.24. This is derived as

$$\sigma^2(t) = (\rho - \rho_c)m(t) = (\rho - \rho_c)\left[C' \left(t_{\mathrm{bu}} - t\right)\right]^{-\frac{1}{\gamma-3}} \,, \tag{4.34}$$

which gives a theoretical prediction for $\sigma^2(t)$ with (4.32).

The dynamics of a typical cluster in a totally asymmetric system can also be determined using similar arguments. The dominating cluster move in one direction in the totally asymmetric graph. The background particles have an average size of $\langle \eta_{x\pm 1}^{\gamma} \rangle \sim O(1)$. For a cluster moving across the lattice with speed m^{γ} with an average $\Delta m = 0.5 \sim O(1)$, as shown in Sec. 4.2.2, the evolution of the occupancy for a typical cluster is given by

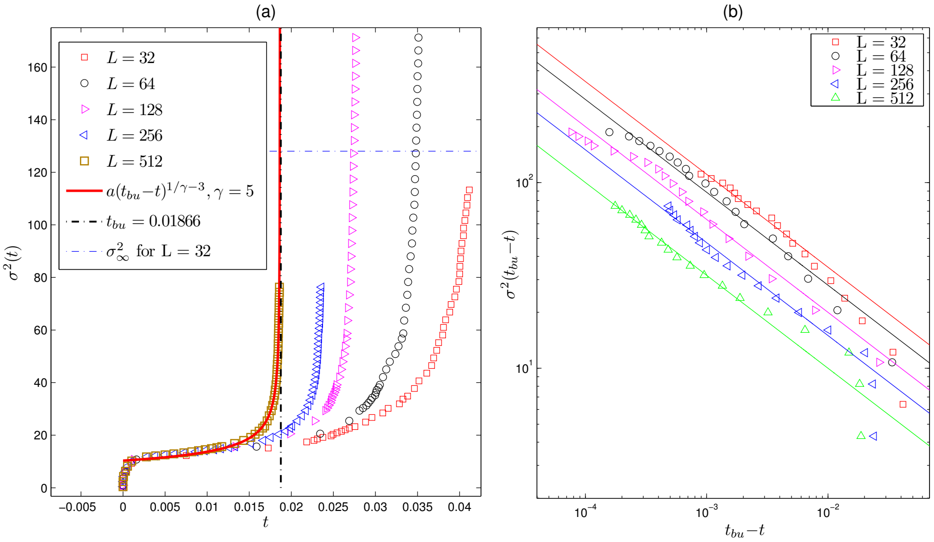

Figure 4.24: For $\gamma = 5$, $d = 0.01$, $\rho = 2$, symmetric graph. (a) $\sigma^2(t)$ for a range of L is plotted. Plots are generated and terminated after reaching a certain proportion of their respective stationary value for efficiency purposes. Blue line represents the cut-off for $L = 32$, where cut-offs for higher system sizes are beyond the range in this plot. t_{bu} and solution of $\sigma^2(t)$ following (4.34) are also plotted with t_{bu} for $L = 512$ indicated by a vertical dash-dotted line. (b) $\sigma^2(t_{\text{bu}} - t)$ is plotted and on a double-log scale to confirm the power law scaling with $-\frac{1}{\gamma-3} = -\frac{1}{2}$ solid lines.

$$\frac{dm}{dt} = Cm^{\gamma} , \tag{4.35}$$

which can be solved to give

$$m(t) = \left[m_0^{-\gamma+1} - (\gamma - 1)Ct \right]^{1/(-\gamma-1)} . \tag{4.36}$$

Substituting $m_0 = m_c$ from Eq. (4.26), the blow up time after reaching critical mass is given by

$$t_{\mathrm{bu}}^{\mathrm{sym}} \sim L^{-\frac{(\gamma-1)}{\gamma}} \searrow 0 , \tag{4.37}$$

and this vanishes for large L, which is consistent to the speed of which explosive condensation occurs.

4.5 Cluster Coarsening

Cluster coarsening is the period of interaction where clusters of size $\sim O(L)$ dominate. As demonstrated in the previous sections, there are two paths to reach the system steady state. Following from the nucleation stage for $\gamma \in (2, 3)$ on the symmetric graph, we recall that the critical mass $m_c \gg L$. This means that nucleation is able to finish completely without reaching the critical occupancy number required for explosive condensation. Several clusters of macroscopic size $O(L)$ emerge, and they start exchanging particles. The coarsening process continues until the system reaches stationarity. In this section, the time scales of coarsening and nucleation are compared and $\langle T_{\mathrm{SS}} \rangle$ is estimated. This is compared to the numerical results, and the scaling is distinctively different from the results obtained for explosive condensation. A time-evolution model for the microscopic interactions during the coarsening process is then proposed.

4.5.1 $\langle T_{\mathrm{SS}} \rangle$ for $\gamma \in (2, 3)$ on a symmetric graph

For totally asymmetric graphs, cluster velocity scales as $v(m) \sim m^{\gamma}$ (see Sec. 4.2.1), and therefore clusters with higher mass collide with lower mass clusters from behind. In doing so, a constant amount of mass is gained in each collision (see Sec. 4.2.2). Let the time for coarsening to finish be T_{Co}. The scaling of T_{Co} can be computed by estimating the time for a cluster to cover the entire empty lattice.

The step rate of clusters for the model characterized by rates (4.1) and (4.2) on a symmetric graph are given in (4.12) and (4.18) respectively. Since clusters on a symmetric graph move like a one-dimensional random walk, they have to make an average of L^2 steps

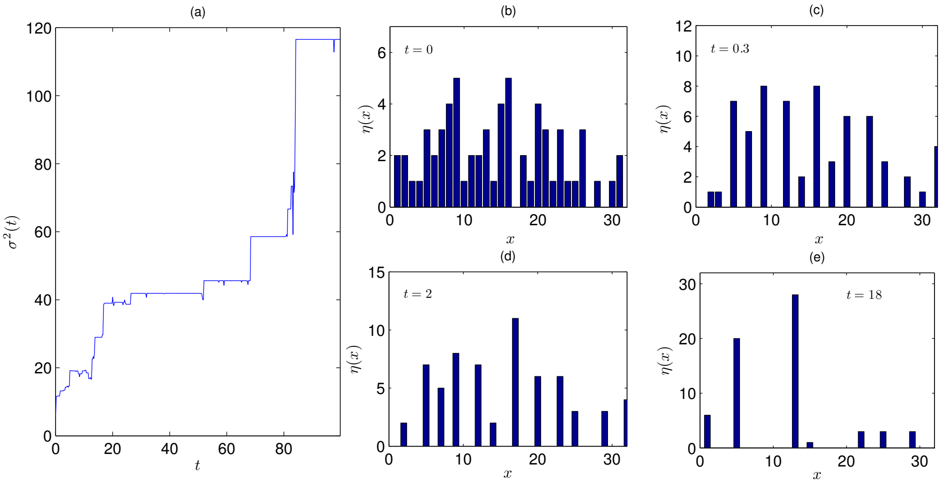

Figure 4.25: For symmetric graph, model characterized by rates (4.1), $\gamma = 2.5$, $d = 0.1$, $L = 32$ and $\rho = 2$. (a) $\sigma^2(t)$ is plotted. Condensation is not observed, and the rapid "hike" in the second moment in the end corresponds to two clusters merging, which is a characteristic feature for cluster coarsening. The configuration at different times are plotted from (b) to (e). (b) At $t = 0$, particles are initialized on the lattice multinomially. (c) Within a relatively short period of time compared to overall $T_{\rm SS}$, the nucleation state is completed, as several clusters $\sim O(L)$ are formed and surrounded by empty sites. (c) and (d) Coarsening process continues for a relatively long period.

to cover the entire lattice. Recalling $N \sim O(L)$, the estimate for symmetric graph coarsening time $T_{\rm Co}^{\rm sym}$ is given as

$$T_{\rm Co}^{\rm sym} \sim L^2 N^{1-\gamma} \sim \rho^{1-\gamma} L^{3-\gamma} \,. \tag{4.38}$$

For the symmetric graph for $\gamma \in (2,3)$, the nucleation and coarsening times are given by $T_{\rm Nu}^{\rm sym} \sim (\ln L)^{2-\gamma}$, as shown in (4.23), and $T_{\rm Co}^{\rm sym} \sim L^{3-\gamma}$ respectively. In the thermodynamic limit $L \to \infty$, $T_{\rm Co}^{\rm sym} \gg T_{\rm Nu}^{\rm sym}$, which suggests the nucleation stage is followed by a prolonged coarsening stage. This is illustrated in the numerical example given in Fig. 4.25. In Fig. 4.25 (a), the second moment versus time for one simulation for $\gamma = 2.5$ is plotted, and the corresponding configuration diagrams are plotted in Fig. 4.25 (b) - (d). Coarsening dynamics dominate as the process of nucleation finishes much quicker. Since $T_{\rm Co}^{\rm sym} \gg T_{\rm Nu}^{\rm sym}$, the time to condensation can be approximated by the contributions of the coarsening stage only

$$\langle T_{\rm SS} \rangle_{\gamma<3}^{\rm sym} \sim L^{3-\gamma} \,. \tag{4.39}$$

Critical densities increase for increasing γ's, and can reach $\rho_c \approx O(1)$. Since $\gamma > 3$,

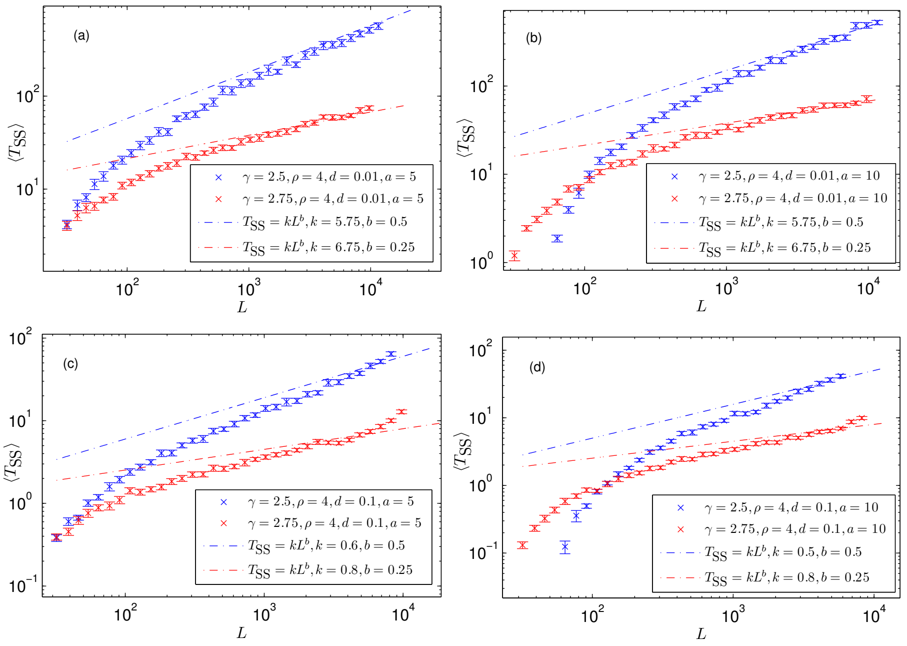

Figure 4.26: T_{SS} against L for the model characterized by rates (4.1), $d = 0.1$, $\rho = 2$, symmetric graph, $\gamma = 2.5$ (blue) and $\gamma = 2.7$ (red). The dashed blue and red lines indicate the scaling behaviour (4.39) for large L. Threshold sensitivity measure a is defined in (4.40). (a) For $d = 0.01$, $a = 5$, (b) for $d = 0.01$, $a = 10$, (c) $d = 0.1$, $a = 5$ and (d) $d = 0.1$, $a = 5$.

the second moment of the background distribution $\langle \eta_x^2 \rangle = \infty$ diverges (see Sec. 3.4), and to account for these fluctuations and constraining computation times, a threshold for which the system has reached stationarity is used. For the second moment $\sigma^2(t)$, a system is considered to have reached stationarity when it reaches a threshold value given by

$$\rho^2 L - a(\rho_c L)^{3-\gamma} , \tag{4.40}$$

with a correction that is $\ll L$, where a is a positive constant that controls the sensitivity of the system to fluctuations. The scaling behaviour of T_{SS} is compared to the numerical results in Fig. 4.26. As shown in Fig. 4.26, a relatively low d is chosen since this improves simulation speed, still $d \gg 1/\rho L$ especially towards the results for large L. The numerical results show good agreement with the time to steady state scaling in (4.39).

4.5.2 Symmetric Coarsening

The first attempt to solve for the time-dependent second moment is by applying the generator to the observable η_x^2, as analogous to the derivation of the inclusion process in Sec.

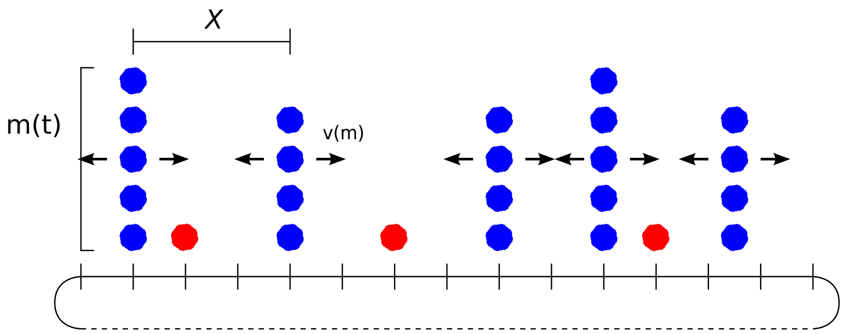

Figure 4.27: Schematic representation of coarsening dynamics for symmetric graph. This represents a typical but simplified version of cluster coarsening, assuming that explosive condensation is not reached (see Sec. 4.4). $n(t)$ clusters of average size $m(t)$ are formed, separated by distance X, and move on a lattice with background density (represented red particles) exchanging particles between them.

3.3.1. As recalled from (2.9), using $f(\eta) = \eta_x^2$

$$\begin{aligned}\mathcal{L}\eta_x^2 = &\left[\eta_x^\gamma(d+\eta_{x+1}^\gamma) + \eta_x^\gamma(d+\eta_{x-1}^\gamma)\right](1-2\eta_x) + \\ &\left[\eta_{x-1}^\gamma(d+\eta_x^\gamma) + \eta_{x+1}^\gamma(d+\eta_x^\gamma)\right](1+2\eta_x)\,,\end{aligned} \tag{4.41}$$

and with $\sigma^2(\eta) = \frac{1}{L}\sum_{x\in\Lambda}\eta_x^2$, the following is obtained

$$\mathcal{L}\sigma^2(\eta) = \sum_{x\in\Lambda}\eta_x^\gamma\left[\eta_{x+1}^\gamma + d(1-\eta_x)\right]\,. \tag{4.42}$$

It is hard to see what are the dominating terms and how to close this equation in a meaningful way. Therefore, an independent mean-field derivation for the average cluster size $m(t)$ is introduced. Fig. 4.27 is a schematic representation of a typical configuration for cluster coarsening on a symmetric graph, assuming that explosive condensation is not reached.

Let there be $n(t)$ clusters of typical size $m(t) \sim O(L)$ that roam on the lattice embedded in a background density. The total mass contained in clusters is given by

$$n(t)m(t) = (\rho - \rho_c)L\,. \tag{4.43}$$

The attempted jump rate of a cluster would be given by $m^\gamma(d + \langle\eta_{x\pm1}^\gamma\rangle)$. The term $\langle\eta_{x\pm1}^\gamma\rangle$ signifies stationary expectation of neighbouring sites. Recall from (2.12) that weights $W(n)$ decay like $n^{-\gamma}$. Principally

$$\langle\eta_{x\pm1}^\gamma\rangle = \frac{1}{Z}\sum_{n=0}^{\infty}W(n)n^\gamma \sim \frac{1}{Z}\sum_{n=0}^{\infty}1 = \infty\,. \tag{4.44}$$

However, since it is assumed that bulk sites are smaller than clusters of size $m(t)$, as illustrated in Fig. 4.27, the sum can be stopped at $m(t) \sim L$. Therefore, the attempted jump rate would be $m^{\gamma+1}$. Only every $1/m^{\text{th}}$ attempt is successful as discussed in Sec. 4.2, and the rate of a successful cluster step would be m^{γ}. The time for two clusters to meet on a symmetric graph is X^2/D, where the average distance X between clusters is

$$X = \frac{L}{n(t)} = \frac{m(t)}{\rho - \rho_c} \,. \tag{4.45}$$

The rate of two clusters meeting is therefore

$$\frac{1}{\tau} \sim D/X^2 \sim m^{\gamma-2}(\rho - \rho_c)^2 \,. \tag{4.46}$$

Two clusters merge with possibility $1/m$ upon collision. Should this occur, the change in the number of clusters would be given by

$$n(t) \to n(t) - 1 = n_{\text{new}}(t) \,. \tag{4.47}$$

Thus $(\rho - \rho_c)L = n_{\text{new}}(t)m_{\text{new}}(t) = m_{\text{new}}(t)(n(t) - 1)$, and the average growth of cluster sizes is given by

$$m_{\text{new}}(t) - m(t) = \frac{m(t)}{m(t) - 1} = \frac{m(t)^2}{(\rho - \rho_c)L - m(t)} \sim m(t) \,. \tag{4.48}$$

This signifies that the mean cluster size changes proportionally to $m(t)$ when two merge, which happens with probability $1/m$. The time evolution of a typical cluster in coarsening can then be written as

$$\begin{aligned} \frac{d}{dt}m(t) = C\frac{D}{X^2}\frac{1}{m(t)}m(t) =& C(\rho - \rho_c)^2 m^{\gamma-2}(t) \\ =& C' m^{\gamma-2}(t) \,. \end{aligned} \tag{4.49}$$

Solving (4.49) with $\gamma \in (2, 3)$, we get

$$m(t) = Ct^{\frac{1}{3-\gamma}} \,. \tag{4.50}$$

We now consider the connection of $m(t)$ to $\langle \sigma^2(t) \rangle$. Following the description in Fig. 4.27, where clusters are interacting on a lattice embedded with background density, $\sigma^2(t)$ is written as

$$\sigma^2(t) = \left\langle \frac{1}{L} \sum \eta_x^2 \right\rangle = \frac{L - n(t)}{L} \langle \eta_x^2 \rangle + \frac{n(t)}{L} m^2(t) \,, \tag{4.51}$$

where once again $\langle \eta_x^2 \rangle = \infty$ for $\gamma \in (2, 3)$ but $\frac{1}{L} \sum \eta_x^2 \sim L^{\alpha}$ for some $\alpha < 1$. So the term

$\frac{L-n(t)}{L} \sum_{x\in\Lambda} \eta_x^2 \ll L$ can be neglected for non-cluster sites. Using 4.43 $\sigma^2(t) = (\rho - \rho_c)m(t)$ is proportional to $m(t)$. The second moment is therefore

$$\sigma^2(t) = C(\rho - \rho_c)t^{\frac{1}{3-\gamma}} \, . \tag{4.52}$$

This is compared to simulated results in Fig. 4.28, where two examples are provided. We see that the predicted exponents in (4.52) are consistent with the data for large times. For comparison, other exponents with better fits are also plotted, and a full numerical confirmation of (4.52) would require data for larger system sizes which are computationally difficult to obtain. Still, we think that our results in Fig. 4.26 and Fig. 4.28 convincingly show that $\langle T_{\mathrm{SS}} \rangle$ diverges with increasing L for $\gamma \in (2, 3)$ on a symmetric graph. Condensation is therefore not explosive, in contrast to results for totally asymmetric dynamics.

4.6 Cluster Stability

In coarsening dynamics on a symmetric graph for $\gamma \in (2, 3)$, the mass of a cluster is assumed to be conserved as it travels through empty lattice sites. Clusters may spontaneously "split-up" and the probability of this occurring is discussed in this section. Cluster splitting-up is a bi-fold process, where a successful split-up requires a cluster to first disintegrate into two or more separate clusters, and subsequently fail to re-merge. The second part of the splitting-up process is characterized by the probability of the two clusters drifting away to a distance $\sim m$ apart:

1. **Splitting**: When a cluster divides without interaction with other clusters, and it forms two clusters. The two clusters are separated by one empty site.
2. **Drifting**: For a cluster of mass m and that has already been split into two, drifting occurs when the two clusters successfully diffuse away from each other, separated by a distance $\sim m$ without re-merging with each other in the process.

In this section, the rates of splits on the symmetric graph for the models with rates (4.1) and (4.2) are computed, and the total number of drifts during coarsening time $\langle T \rangle_{\mathrm{Co}}^{\mathrm{sym}}$ are estimated.

For the models studied in this thesis, a schematic representation of the process for cluster splitting on a symmetric graph is illustrated in Fig. 4.29. As a cluster moves through the lattice, its mass m is distributed over two lattice sites over some period of time, with sizes $m - k$ and k, respectively. During this time, a particle may hop in the opposite direction, which may trigger a break-up step in the other direction, as illustrated in Fig. 4.29 (a) and (b). Should this step attempt be successful, the cluster splits into two separate clusters, and

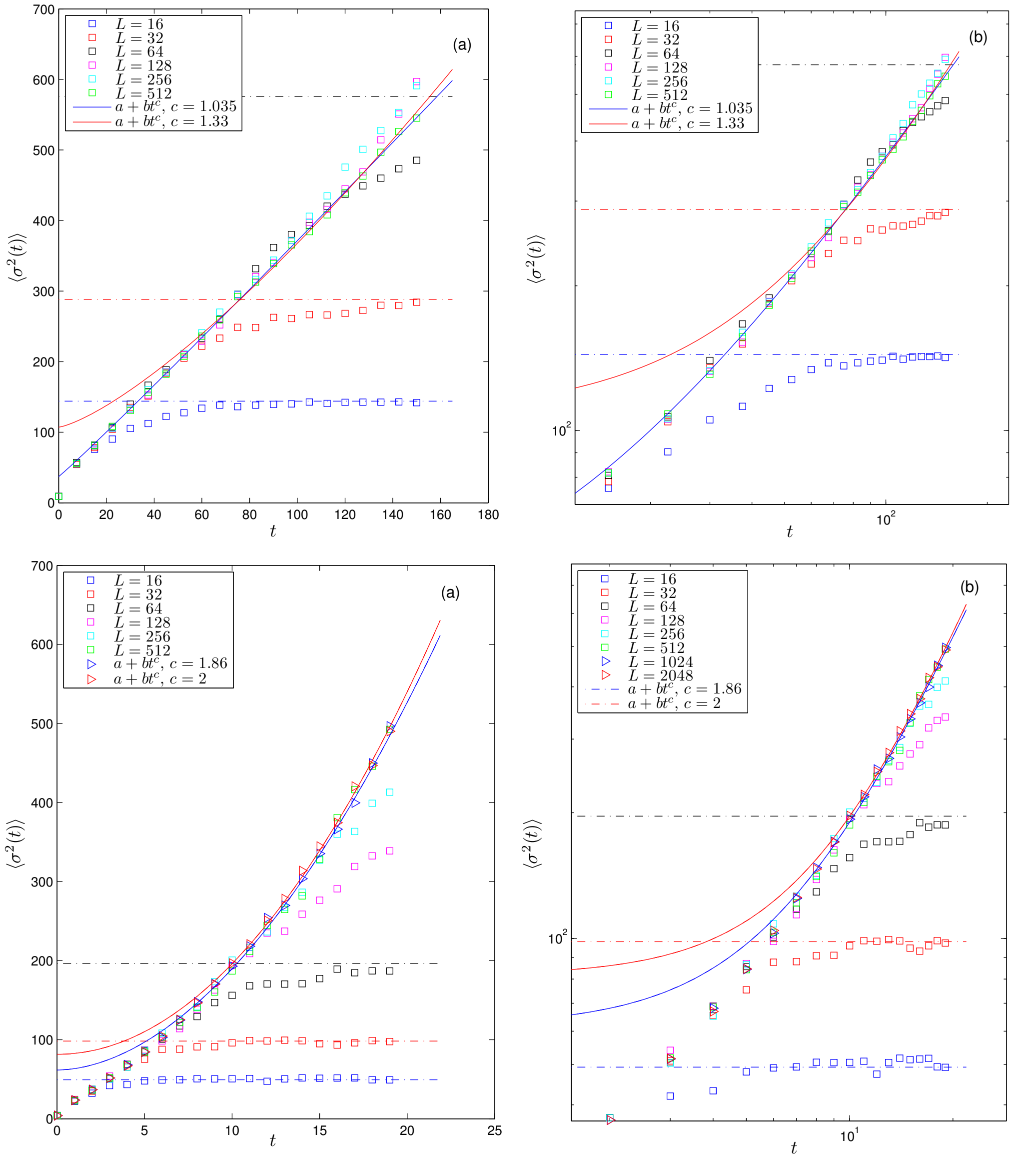

Figure 4.28: $\langle \sigma^2(t) \rangle$ against t, symmetric graph, for model characterized by rates (4.2). Dashed lines represents σ^2_∞ for $L = 16, 32, 64$, and the solid lines are given by (4.52) with different scaling for comparison. (a) $\gamma = 2.25$, $d = 0.01$ and $\rho = 3$ and the log-log version is given in (b). (c) $\gamma = 2.5$, $d = 0.1$ and $\rho = 2$ and the log-log version is given in (d).

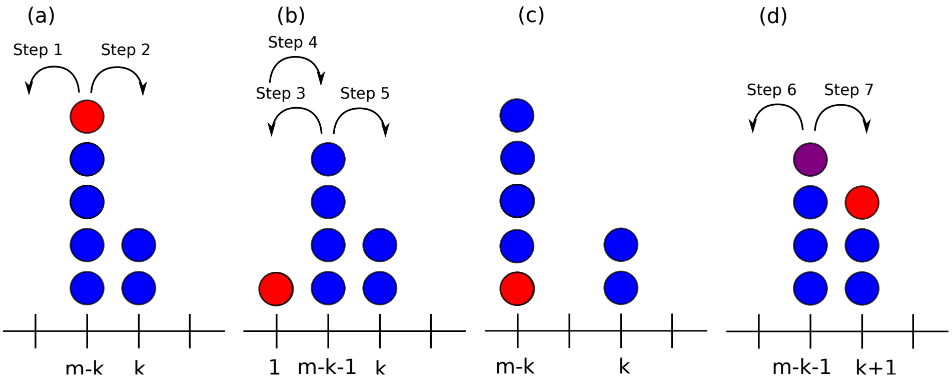

Figure 4.29: Schematic illustration of a cluster splitting on symmetric graph. The occupancy number is labelled at the bottom of each of the sites displayed. (a) A typical scenario while a cluster with mass m moves along the lattice, a fraction of the cluster's mass k is moved to a neighbouring site. The process of a cluster splitting may be triggered if the red particle hops to the opposite direction (step 1), as opposed to moving in the direction towards the pile with k particles (step 2). If the red particle has hopped left: (b) In this scenario, the rates of step 3 and 4 are roughly the same. Therefore, the dynamics between the left and the centre cluster follows a one-dimensional symmetric random walk. The clusters would successfully split after an average of $\sim m$ tries. (c) Should a split be successful, the resulting configuration is illustrated. (d) If "step 2" is taken instead of "step 1", a similar argument from (a) to (c) dictates that the purple particle has $\sim 1/m$ chance of splitting away from the centre cluster, but now with the split being $m - k - 1$ and $k + 1$ in size.

their sizes would be related to the fraction of mass k transported when a particle decides to hop in the opposite direction. The probability of split is, therefore, the time spent while the cluster is in the middle of a step multiplied by the rate at which the rest of the jump in the opposite direction is successful. The notation $v(m-k)$ is the rate of a successful second jump. We write the probability of split as

$$p_{\text{split}} = \sum_{k=1}^{m} v(m-k) T_{k,m} \, . \tag{4.53}$$

Note that this probability would be a slight overestimate, as the time contributions from the subsequent steps following a successful second jump are ignored.

In the models of this study, clusters are always embedded in a non-empty background with density $\rho_c \sim O(1)$. Splits with sizes $\sim O(1)$ do not therefore constitute a part of the macroscopic dynamics. To ensure that only macroscopic splits are measured, the window of times for split-up cluster moves is selected as

$$p_{\text{split}} = \sum_{k=\epsilon m}^{(1-\epsilon)m} v(m-k)T_{k,m} = \sum_{k=\epsilon m}^{(1-\epsilon)m} \frac{v(m-k)}{(m-k)^{\gamma}k^{\gamma}} \ . \tag{4.54}$$

ϵ is introduced to distinguish splits with size $\sim O(m)$, whose presence can influence the macroscopic dynamics of the system and contradict the assumption that cluster mass is almost always conserved. The rate at which the second jump is successful is given by

$$v(m-k) = (m-k)^{-1}\left(\sum_{i=1}^{m-k}\frac{1}{(m-k-i)^{\gamma}i^{\gamma}}\right)^{-1} \sim (m-k)^{\gamma-1} \ . \tag{4.55}$$

The derivation of (4.55) is similar to the derivation of the velocity of a cluster on a symmetric lattice, which is computed in (4.17) and (4.18). Substituting this result and taking $k/m = x$ and $dk = mdx$, (4.54) can be integrated by taking $m \to \infty$ using the Euler-Maclaurin equation

$$p_{\text{split}} = \int_{\epsilon}^{1-\epsilon} \frac{dx}{(1-x)^{-1}x^{\gamma}} = \int_{\epsilon}^{1-\epsilon} \frac{mdx}{m^{\gamma+1}(1-x)x^{\gamma}} \ . \tag{4.56}$$

This is further simplified to give

$$p_{\text{split}} = m^{-\gamma}\int_{\epsilon}^{1-\epsilon} \frac{dx}{x^{\gamma}-x^{\gamma+1}} \ . \tag{4.57}$$

Given $\epsilon \in [0,1)$ and $\gamma > 2$ and that we are interested in the scaling of m only, the leading term in Eq. (4.57) is integrated over and this gives

$$p_{\text{split}} \sim m^{-\gamma}\epsilon^{1-\gamma} \ . \tag{4.58}$$

Depending on the choice of ϵ, p_{split} is given as

$$p_{\text{split}} \sim \begin{cases} m^{-1} & \text{for } \epsilon \sim \frac{1}{m} \\ m^{-\gamma} & \text{for } \epsilon \sim 1 \ . \end{cases} \tag{4.59}$$

Measuring p_{split} numerically requires a choice of ϵ such that smaller clusters that contribute to the background density ρ_c would not be counted. The choice $\epsilon = 1/m$ in (4.59) represents the probability of all splits, including smaller splits. For the macroscopic splits, which is the focus of this section, $\epsilon \sim O(1)$ is used, which means that $p_{\text{split}} \sim m^{-\gamma}$. ϵ is carefully chosen such that $\epsilon m > \rho_c$, where ρ_c is the critical density of the system.

Numerically, p_{split} is not determined in a straightforward way, as a cluster may split into multiple clusters of size $O(1)$ or move along the lattice without ever reaching $\sum_{x\in\Lambda}\eta_x\eta_{x+1} = 0$. To estimate p_{split}, the system is initiated by firstly placing all particles on site $x = 0$. The system is allowed to run until:

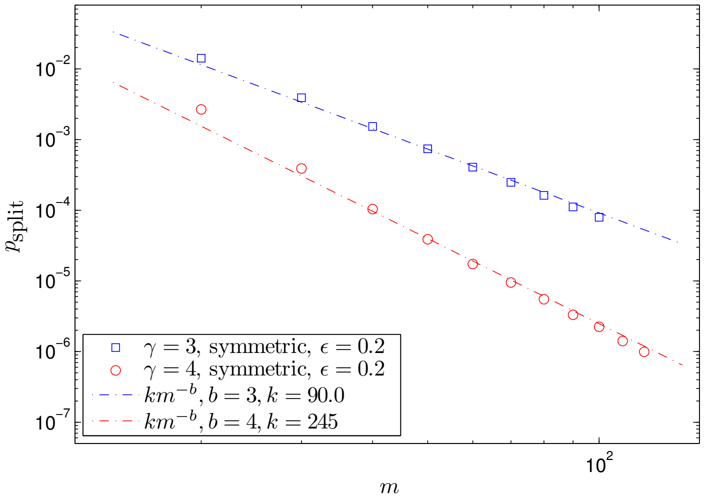

Figure 4.30: For $d = 1$, model characterized by rates (4.2), symmetric graph. p_{split} for $\epsilon = 0.2$ is plotted against initial cluster size m. The theoretical results given in the dashed lines following (4.59). Critical density is $\rho_c = 0.701$ and $\rho_c = 0.212$ for $\gamma = 3$ and $\gamma = 4$, respectively.

- When $(1 - \epsilon)m$ is found at either one of the two neighbouring sites of $x = 0$. This would count as a normal step of a cluster, and no split would be counted, or
- when any two sites of the system have mass that exceeds ϵm, and these two sites are not nearest neighbours. This case would count as a split.

The numerical results illustrating the scaling behaviour between p_{split} and m are shown in Fig. 4.30. Notice that the scaling in Fig. 4.30 follows (4.59), but has a slightly quicker rate of decay. This might be a consequence of underestimating the time required for the cluster to have a successful second step, as indicated when deriving (4.53). Since the probability of split p_{split} is the chance that a split would occur when a cluster is moving one step a lattice, the rate of split is given by

$$r_{\text{split}} = v(m) p_{\text{split}} , \tag{4.60}$$

where $v(m)$ is the rate of a cluster step, which is determined in (4.18). Recalling that $m \sim O(L)$ towards the end of dynamics, and substituting the second part of (4.59) into (4.60) gives

$$r_{\text{split}} \sim m^{\gamma-1} m^{-\gamma} = m^{-1} \sim L^{-1} . \tag{4.61}$$

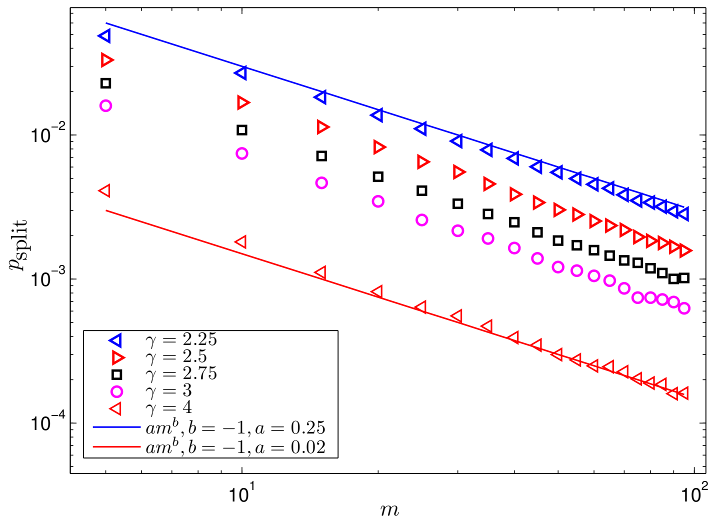

Figure 4.31: $p_{\rm split}$ versus m for the model characterized by rates (4.1), $d = 0.5$, on symmetric graph. Numerical results for different values of γ are shown with error comparable to symbol sizes. Theoretical results for $\gamma = 2.25$ and $\gamma = 4$ are given by (4.59) with $\epsilon \sim 1/m$, plotted as solid lines.

As $L \to \infty$, the rate of split $r_{\rm split} \to 0$. Cluster splitting takes part during coarsening dynamics only, and the coarsening time on the symmetric graph scales as $\sim L^{3-\gamma}$, as computed in Sec. 4.5. The total number of clusters breaking up $N_{\rm br}$ in this time scale is therefore given by

$$N_{\rm br} \sim L^{-1} L^{3-\gamma} = L^{2-\gamma} \,. \tag{4.62}$$

For $\gamma > 2$ and $L \to \infty$, the number of macroscopic splits diminishes. An interesting case arises when $\gamma < 2$, $N_{\rm br}$ increases with L. This would lead to a diverging background density, and corresponds to the results derived from the stationary product measures, where condensation occurs only for $\gamma < 2$ as explained in Sec. 3.4.1. For completion of the discussion of cluster stability, $p_{\rm split}$ for $\epsilon \sim 1/m$ is also numerically measured in Fig. 4.31, where the difference in scaling behaviour can be compared to Fig. 4.30. The probability of split scales as $p_{\rm split} \sim m^{-1}$, and no γ dependency is observed.

Similar to the derivation for the rate of splits in (4.61), the rate of splits for $\epsilon \sim 1/m$ would be $*p_{\rm split}^{\epsilon\sim 1/m} \sim m^{\gamma-1} m^{-1} = m^{\gamma-2} \sim L^{\gamma-2}$. The total number of splits during a coarsening process if smaller split clusters are counted as well. This is given as

$$N_{\rm br} \sim L^{\gamma-2} L^{3-\gamma} = L \,. \tag{4.63}$$

Note that this result encompasses splits of all sizes, with the majority of them being clusters with mass $\sim O(1)$. This means that the rate of particle accumulation of a macroscopic cluster is of the same scale as the rate of splitting into smaller clusters of size $O(1)$, which is consistent with the fact of having non-zero background density.

4.7 Discussion

This Chapter is a study of the microscopic dynamics leading to stationarity for the variations to the explosive condensation model, where the rates are introduced in (4.1) and (4.2). We focus on the $\gamma > 2$ range, where condensation is expected from the scaling of stationary weights (see Chapter 3). It should be noted that the models studied in this Chapter are translationally invariant, and we consider the thermodynamic limit of diverging lattice size and particle number with a fixed density. Other heuristic studies of condensation in homogeneous interacting particle systems include results on the ZRP [24, 26, 69, 73, 74], IP [23, 54, 57] and the ECP case [6, 59]. We are motivated by the findings of Waclaw and Evans, and want to find a more detailed characterisation of the formation of explosive condensates, including also the case of symmetric dynamics which has not been studied so far.

Explosive condensation and cluster coarsening are two processes observed in models with rates (4.1) and (4.2), and the dynamics of both processes are largely driven by cluster interactions. Before going into the timescale studies of each process, we explore the physical properties of clusters (see Sec. 4.2). Our cluster dynamics findings resembles Evans and Waclaw in the totally asymmetric case but have extended them for symmetric graphs as well. We introduce the concept of a critical occupancy number and provide the scaling with the system size. As a cluster grows to a critical occupancy number, it is able to cover the entire lattice in a very short period of time and accelerates as it continues to gain mass. With the understanding of clusters and the scaling of critical occupancy number, a scaling for the times for coarsening and nucleation are estimated.

The nucleation-coarsening model leads to a straightforward and comprehensive explanation of the scaling of the time to stationarity $\langle T_{\mathrm{SS}} \rangle$, arriving to the same scaling as the one proposed in [6] for the totally asymmetric case. The distinction between cluster nucleation and coarsening is not studied in [6, 59], because this only becomes significant for symmetric cases. We observe a rich behaviour for symmetric cases, depending on the system parameter γ. For $\gamma \in (2, 3)$, $\langle T_{\mathrm{SS}} \rangle$ increases with system size, whereas for $\gamma > 3$, $\langle T_{\mathrm{SS}} \rangle \to 0$ for $L \to \infty$.

The two scenarios to condensation are presented separately in this Chapter (Sec. 4.3 - Sec. 4.5), in which we often interchange within the discussions with different graphs. To have a coherent picture of the paths to stationarity in different ranges of γ and graphs, we summarize these results in Table 4.4. This can be read in conjunction with Sec. 4.1, where the multi-stage model leading to condensation is outlined in more detail.

Graph / range of γ	$0 < \gamma < 2$	$2 < \gamma < 3$	$\gamma > 3$
Symmetric	No Condensation	Coarsening Condensation	Explosive Condensation
Totally Asymmetric	No Condensation	Explosive Condensation	

Table 4.4: Summarising results in Chapter 4, listing the paths to stationarity for different range of γ and graph in the thermodynamic limit. The dynamics of coarsening condensation is illustrated in Sec. 4.5 and explosive condensation in Sec. 4.4. For the dynamics for $\gamma < 2$, where there is no condensation, which is established in Chapter 3.

From this multi-stage model, the explosive condensation scaling behaviour for $\langle T_{\text{SS}} \rangle$ is derived (4.27) for the totally asymmetric case, and is extended to the symmetric case in (4.28). For both results, the time to condensate goes to zero as $L \to \infty$, which is counter-intuitive from a physical perspective. This was first proposed in [6], but is confirmed for both symmetric and totally asymmetric cases with a detailed analysis.

In the future, similar systems for inhomogeneous cases and where mass is not conserved can be studied. Other variants of the model, such as one where the convergence critical densities depends on both γ and d can be studied (see Chapter 6).

For the findings of this Chapter, obtaining numerical results for $L > 10^3$ for symmetric graph cases are particularly difficult. To overcome the issue, we introduced a method that preserves stochasticity in particle exchange but also greatly simplifies simulating a moving cluster. This method is used for cases with explosive condensation only, and is explained further in Chapter 5. The main numerical results, such as Fig. 4.14, 4.21 - 4.24 are all obtained using this method.

Chapter 5

Numerical methods in explosive condensation

5.1 Introduction

The standard approach in simulating continuous-time Markov processes is by implementing the Gillespie algorithm, which was first introduced to solve continuous-time chemical systems [75]. Applications of the algorithm, alongside other numerical techniques [76], have since been applied to a wide range of simulations including the study of interacting particle systems. The numerical findings in Chapters 3 and 4 follow the broad strokes of such methods. However, as heuristic results derived in cluster interactions (see Sec. 4.2) emerge, several novel simplifications in the numerical methods can be implemented. From these novel simplifications, we develop a new algorithm for simulating Interacting Particle Systems. This algorithm can reduce simulation time by several magnitudes yet preserving the stochastic characteristics of the simulation. The new algorithm is used throughout this thesis and has also been adopted in other interacting particle systems research [54]. In this thesis, the new method are used especially for obtaining simulation results for higher L in the symmetric graph, where there is explosive condensation. In this Chapter, the foundations of the numerical methods in this thesis are outlined, together with discussions of its accuracy and limitations.

5.2 Exact stochastic simulation

Monte-Carlo simulation in this study uses the Fast Mersenne Twister [77, 78] for generating pseudo random numbers. Numerically simulating a continuous-time Markov process requires a reliable method to update times and the occupancy of states with a given set of rates. For a one-dimensional particle system with state space $X \in \mathbb{N}^{\Lambda}$, lattice Λ with finite size L and rates for interactions to take place where state space changes from η to η', we can simulate the changes of the occupancy throughout time using the Gillespie method [75] (or the Bortz-Kalos-Lebowitz algorithm [79]) directly with the information of the profile of rates $c : \{c_i$, where $i \in \Lambda\}$ without using the master equation. This method provides a simple and statistically accurate trajectory for stochastic simulation. This involves a simple update of the system time, where for the total rates of the system $R = \sum_{i,j\in\Lambda} r_{x,y}$, the update of the system time is simply

$$\Delta t = -R^{-1} \ln(u) \,, \tag{5.1}$$

where u is a random number with uniform distribution on $u \in (0, 1)$. The exact algorithm is presented in Appendix B.1. Binary tree search is used to optimize the efficiency of Monte-Carlo method over a large graph, as depicted in Appendix B.2.

Several issues arise when attempting to obtain numerical results for systems with explosive condensation. Firstly, while Waclaw and Evans computed results for $L \sim L^3$ for the totally asymmetric case, obtaining results for $L > 10^3$ in the symmetric case is extremely difficult. This is explored further in Sec. 5.3, where a new algorithm is introduced. For most of the results in Chapter 4 with explosive condensation, this new algorithm has been used. Discussions of its reliability and improved efficiencies are presented in Sec. 5.3.3.

Averaging over regular observable intervals

The other problem is the study of time-evolution observables $f(t)$ in the realms of cluster condensation. Studying observables over pre-defined time-intervals is the standard approach to studying a converging set of results. However, as computation time drastically increases for large L during explosive condensation (see Sec. 5.3.1), the problem is twofold. Firstly, having fixed time intervals means that systems that have reached stationarity would have to continue to run for a long period of time. Secondly, explosive condensation has a characteristic long nucleation time followed by an abrupt explosive condensation. Ignoring negligible effects from a rare split from a moving cluster, observables such as σ^2 and $\eta_{\max}$ are strictly increasing functions that are dependent on the evolution of the largest cluster. Four individual plots of $\sigma^2(t)$ are plotted in Fig. 5.1.

After varying periods of cluster nucleation, the system reaches condensation comparatively quickly once $\eta_{\max}$ reaches a critical value m_c as derived in (4.25). The times to condensation are evidently strongly dependent on the distribution of nucleation times. Averaging σ^2 over time produces a poor estimation of $\langle T_{\text{SS}} \rangle$ as it discounts the contributions of distributed nucleation times to T_{SS}. Therefore, for cases with explosive condensation,

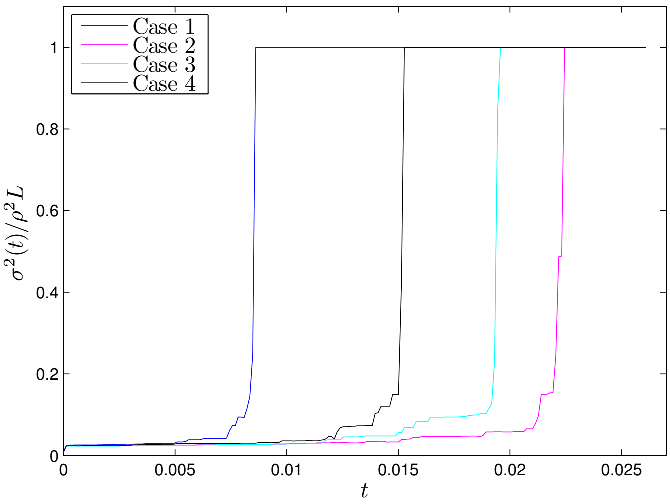

Figure 5.1: Four instances $\sigma^2(t)$, $\gamma = 5$, $d = 0.1$, symmetric graph, $\rho = 2$, $L = 64$ for model characterized by rates Eq. (4.1). Each instant shows a prolonged waiting time and an abrupt condensation process. Averaging over regular intervals of time would fail to capture the characteristic abruptness.

we measure the times when regular and successive observables are reached. The averaged results will be computed by averaging the different times instead of averaging the observable over regular times. This method has been used to obtain results for $\sigma^2(t)$ and $\eta_{\max}(t)$ for cases with explosive condensation.

5.3 Simplification of piles of effective cluster dynamics

For some of the numerical simulations in Chapter 4, simplifications on the original implementation of the Gillespie method are made. In this section, the method is outlined, together with a discussion on its efficiency, reliability and limitations.

5.3.1 Simulating large system sizes L

Let Ω be the total number of steps for a simulation to run from start to finish, such that a step is a numerical process that corresponds to the smallest change on the system configuration η. In the framework of the Gillespie method, one step corresponds to the movement of a particle to its neighbouring site. We first discuss the number of steps for the simulations executed in Chapter 4.

For $\rho > \rho_c$, stationarity is reached through two different mechanisms that are outlined in Sec. 4.1. Both these methods start from cluster nucleation, where particles of size

$\langle m \rangle \sim \rho \sim O(1)$ start to interact with each other and grow in size. This process terminates either by reaching cluster coarsening or explosive condensation, which have cluster sizes diverging with L.

For the totally asymmetric case, clusters move in the same direction. Clusters grow by moving across the system. m particles require m steps and there are L steps to cover the entire lattice, the total number of steps for the nucleation stage is $\sim mL$. Since $m \sim O(1)$ for the nucleation stage, therefore $\Omega^{\mathrm{asym}}_{\mathrm{Nu}} \sim L$. However, as the clusters grow and the dynamics are more cluster-dominated, clusters have size $m \sim O(L)$. The number of steps to finish cluster coarsening or condensation is unchanged at $\sim mL$. Focusing on the case for a system with explosive condensation, from Sec. 4.2.2, it is understood that clusters gain $\sim O(1)$ particles from each collision. As particles in the background when a single condensate dominates are of mass $\sim \rho$, this means $\Omega^{\mathrm{Co}}_{\mathrm{asym}} \sim L^2$. Therefore for large L

$$\Omega_{\mathrm{asym}} \sim L^2. \tag{5.2}$$

For the symmetric case, the same arguments can be used. Since particles can move in both directions, the movement of a cluster of particles with size m requires m attempts to successfully move itself across a lattice space. L^2 steps are required to cover the entire lattice. Therefore for the nucleation stage to finish, it requires $\sim m^2L^2$ steps. Similar to the arguments for the totally asymmetric case, $m \sim O(1)$, therefore $\Omega^{\mathrm{sym}}_{\mathrm{Nu}} \sim L^2$. For clusters of size $m \sim O(L)$ to cover the entire lattice, $\Omega^{\mathrm{sym}}_{\mathrm{Co}} \sim m^2L^2 = L^4$ steps are required. Therefore the overall number of steps for a symmetric graph to reach stationarity is given by

$$\Omega_{\mathrm{sym}} \sim L^4. \tag{5.3}$$

For both the symmetric and totally asymmetric case, coarsening and condensation dynamics would take much longer to complete, when compared with the nucleation dynamics. In Waclaw and Evans' [6, 59] original studies for totally asymmetric cases, they are typically numerically evaluated up to $L \sim 10^3 \sim 10^4$. For original implementations of the algorithm depicted in Appendix B.1, results beyond $L \sim 10^2$ for the symmetric cases and $L \sim 10^3$ for the totally asymmetric case were extremely expensive to obtain. In order to have a better understanding of the scaling behaviour of T_{SS} with L, modifications of the numerical methods are required.

5.3.2 Interchanging between cluster movement and collision

From Sec. 4.2 and Sec. 4.6, properties of a cluster from a microscopic perspective are better understood. These properties are vital in adapting the algorithm for greater efficiencies. Firstly, we note that the mass of clusters are largely preserved until collision. Secondly, the rate of entire clusters moving across lattice spaces can be accurately predicted for both asymmetric and symmetric systems (see Sec. 4.2.1), where clusters with mass m transports all its mass to a neighbouring site with rate $\sim m^{\gamma}$ for the totally asymmetric case, and $\sim m^{\gamma-1}$ for the symmetric case. This property is used to improve numerical efficiencies for later parts of the dynamics, namely the coarsening and the explosive condensation stage.

For the later parts of system dynamics, where interactions are dominated by clusters, transportation of an entire cluster can be simplified as one step by using the rates of cluster movement. In this case, the scenario in Fig. 4.4 and Fig. 4.5 can be replaced by a single numerical step. Clusters are therefore regarded as independent entities each with non-zero rates, which characterises a separate continuous-time model. Updates on the configuration space would involve the movement of entire clusters instead of a unit of mass. The interactions thereby enters a purely cluster-centric phase, in which the computationally intensive process of particle-particle movement of clusters can be substituted by a single step.

Cut-off and cluster-cluster interactions

There remain two questions. Firstly, switching to a completely cluster-centric model is only accurate if clusters are well separated. During the nucleation phase, occupants on the configuration are of size $m \sim O(1)$. The estimation of cluster speeds are only accurate for when the dynamics are dominated by the movement of large clusters of size $m \sim O(L)$. Therefore, a cut-off time for when large clusters dominate should be identified. Our algorithm should therefore switch from a particle-particle interaction to cluster-cluster interaction upon a good cut-off time. Secondly, it is true that the movement of clusters over empty lattice sites can be easily predicted by the said method above. However, the stochasticity of mass exchange in cluster-cluster interactions is hard to predict (c.f. Sec. 4.2.2).

We first consider the question of the switch-time. In the explosive condensation model, there is no clear cut-off between cluster nucleation and its subsequent stages. The simple solution is to use a stricter cut-off condition. The most straightforward method is to switch methods when there are no two non-zero clusters neighbouring each other. This is the case when nucleation has strictly finished, such that

$$\sum_{x\in\Lambda} \eta_x \eta_{x+1} = 0 \, . \tag{5.4}$$

As explained in Sec. 4.2.2, the transfer of mass $\Delta m(m_1, m_2)$ between clusters with size m_1 and m_2 has no simple solution. While for $m_1 \gg m_2$ in the totally asymmetric case, $\Delta m \sim 0.5$ for $m_2^{\gamma} \gg d$, there [59]. For the symmetric case, we know that $\Delta m \sim m$, but it is difficult to determine the exact solution, as there is a great element of stochasticity.

Therefore, to preserve the numerical accuracy of Δm exchanges between clusters, it is best to preserve interactions between clusters to the full simulation method.

Switching numerical methods and back

The numerical simulation is required to switch from the cluster-movement phase to a cluster-exchange phase, and revert back during cluster-cluster collision, such that the dynamics would begin normally; until condition Eq. (5.4) is reached. As this is another continuous-time Markov process, the Gillespie method can be implemented but with a different set of rates.

If there are k clusters on a symmetric lattice, each would have rates $r_i = m_i^{\gamma-1}d$ for the model characterized by Eq. (4.2). For Waclaw's original model this would be $r_i = m_i^{\gamma-1}d^{\gamma}$. However, if there is another cluster that shares the destination site as neighbour, the rate for that jump should be given by $r_i = m_i^{\gamma}d$ and $m_i^{\gamma-1}d^{\gamma}$ respectively. This is because that step would trigger another set of dynamics that is reverted back to the original set of algorithms. Therefore the rates for that specific jump should be the same as original rates as well. The same idea would apply for the totally asymmetric case. The time update is given by the same method using the Gillespie time update outlined in Eq. (5.1), but with $R = \sum_{i=1}^{k} r_i$.

If a cluster jumps to a space that is neighboured by another cluster, it would enter another phase where the interactions between the two clusters are considered independently from the rest of the dynamics. Note that towards the end of the dynamics, system size is $m \sim O(L)$. Consequently, the exchange of mass between two clusters greatly exceeds the rate of clusters moving into empty spaces, as $m^{2\gamma} \gg m^{\gamma}d$. Therefore, the diffusivity of clusters can be ignored when there are two clusters exchanging mass.

The interaction between the two colliding clusters can be mapped on the diagram in Fig. 5.2, where cluster-cluster interaction terminates when either the two clusters merge, or mass on both sites are conserved. In this process, some mass might be transferred from one to another. The entire algorithm can be found in Appendix B.3.

5.3.3 Comparing new and old algorithms

The new algorithm provides a much faster simulation of results, especially the dynamics towards stationarity. An example of the improved efficiencies are illustrated in Fig. 5.3, where the $\sigma^2(t)$ is plotted for both old and new algorithms.

The results in Fig. 5.3 exhibit explosive condensation, where cluster nucleation dictates early dynamics until $\eta_{\max}$ exceeds some critical occupancy number. From Fig. 5.3 (a) and (b), the rapid increase in number of steps is accompanied by the growth of

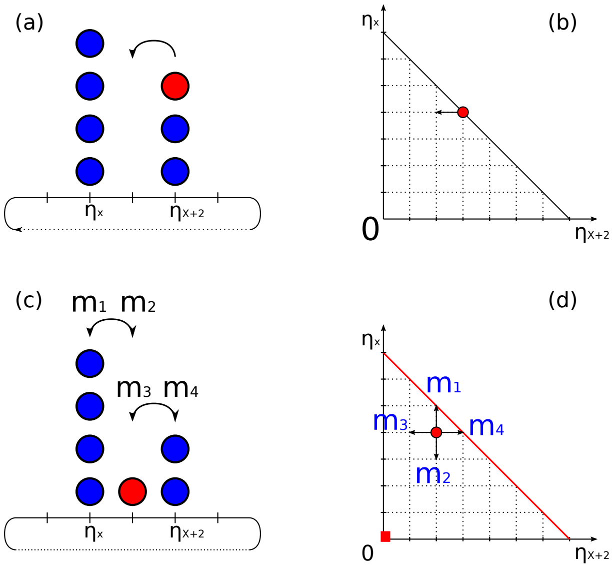

Figure 5.2: The model is adapted to accommodate special cases when clusters interact with each other for symmetric cases. Clusters are freely moving on empty lattices until (a) a particle moves into a space with another cluster in its proximity. The computation is switched to another algorithm depicted, with the values of η_x and η_{x+2} before the first interaction is saved. And this maps into a process where particle performs a random walk on a two-dimensional lattice as depicted in (b). Rates of the next move are computed and are represented in (c). The rates are similarly mapped into the lattice as shown in (d), and the red particle moves accordingly to the rates. This algorithm is stopped only when, either $\eta_{x+1} = 0$ or the two clusters are merged. The first absorbing state is depicted in the diagonal red line, and the latter case is when the particle moves into the dot at origin.

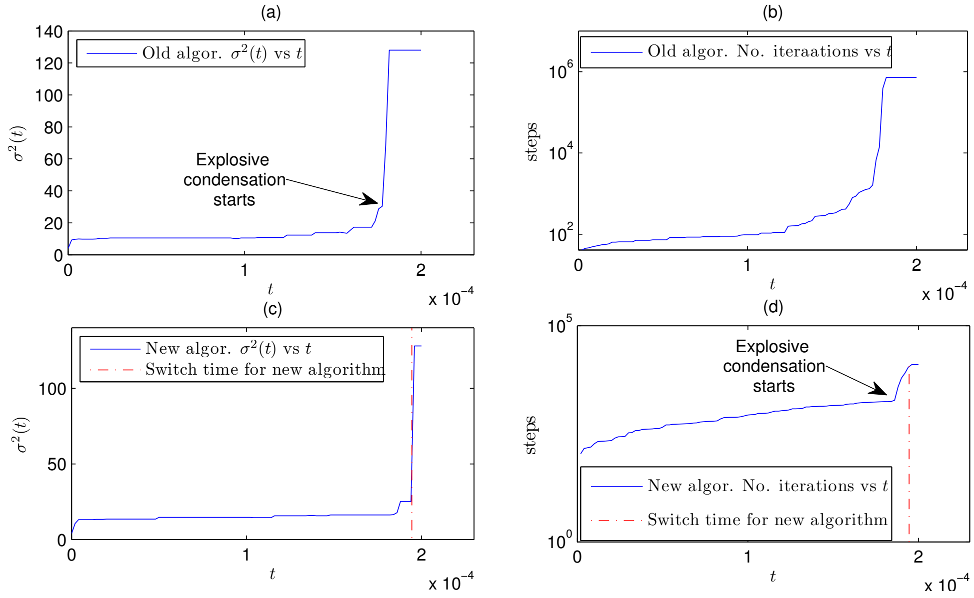

Figure 5.3: For $\gamma = 7$, $d = 0.5$, $\rho = 2$, $L = 32$ with the model characterized by rate (4.1) on a symmetric graph, comparing the number of steps required to obtain a similar set of results using the old algorithm and the algorithm denoted in Sec. 5.3.2 and Appendix B.3. (a) and (b) are computed using the original algorithm, with (a) σ^2 plotted against time. The approximate times for explosive condensation is indicated by the arrow. (b) Number of steps plotted against time. (c) and (d) are computed using the new algorithm described in Sec. 5.3.2 and the red dashed lines represents the time where the method of algorithm interchanges. (c) σ^2 against time, and (d) the number of steps against time, with an arrow indicating when explosive condensation starts to dominates.

condensate and it takes approximately $\Omega \sim 10^6$ steps for simulation to complete. In Fig. 5.3 (c) and (d), which is the same simulation but for the new algorithm, there is an initial rapid increase in steps as $\eta_{\max} > m_c$. However, as the cut-off Eq. (5.4) is reached, the growth of steps is greatly reduced and eventually $\Omega \sim 10^4$.

New algorithm for the totally asymmetric case

For the new algorithm in the totally asymmetric case, clusters of size m would take only one step to move across one lattice space, and it requires L steps to cover the entire lattice. Therefore total number of steps would be $\sim L$ and this is comparable to the contribution of the nucleation part. However, one must also consider the contributions from cluster-cluster interaction, which requires the transportation of m over L number of clusters of size $\sim O(1)$. This results in the overall scaling $\sim mL$. Therefore total number steps scales the same as the previous method:

$$\Omega'_{\text{asym}} = L$$

New algorithm in the symmetric case

For the new algorithm in the symmetric case, clusters of size m would take only one step to move across one lattice space, and L^2 steps are required to reach the entire lattice. However, one must also consider the effect of cluster-cluster interactions. For clusters of size $\sim O(L)$, the number of clusters would be $\sim O(1)$. When a cluster of mass $m \sim O(L)$ interacts with other clusters, it would take m steps to manifest itself on the target cluster, and they would have a $O(1)$ probability of diffusing away from each other. Therefore the total number of moves in one collision is given by m. At this stage, the clusters would be separated by a space of one. In the case of explosive condensation, the background is of the size $\sim O(1)$ and has $\sim L$ clusters. Therefore the number of steps for cluster-cluster interaction would be given by $\sim L^2$ as well. So the total number of steps would be

$$\Omega'_{\text{sym}} = L^2 \,. \tag{5.5}$$

The improved efficiency for simulation later parts of the dynamics made it easier for obtaining results beyond $L > 10^2$ in the symmetric case. As results in Fig. 4.23 shows, numerical simulations for $L \sim 10^4$ can be computed to have a clearer scaling behaviour of $\langle T_{\text{SS}} \rangle$.

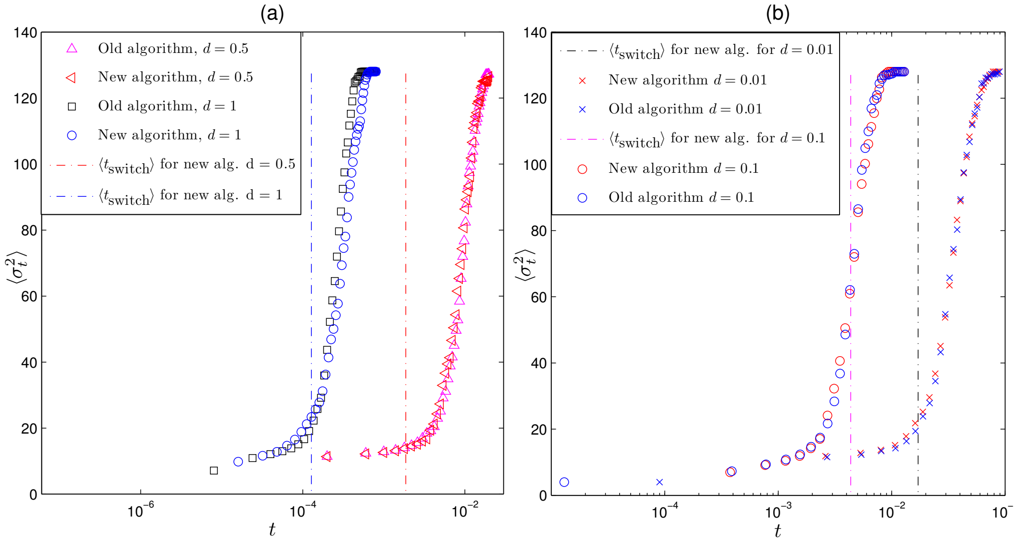

Figure 5.4: $\langle \sigma^2(t) \rangle$ for $\gamma = 5$, $\rho = 2$, $L = 32$, symmetric graph. The original and the new algorithm are plotted alongside for each graph. Dashed line indicates the switch time when the cluster based implementation is used. The two sets of results uses different set of rates and d. (a) Model characterized by rates Eq. (4.1), $d = 0.5$ and 1. (b) Model characterized by rates Eq. (4.2), $d = 0.01$ and 0.1.

New algorithm for cluster coarsening

Note that this is for the case with explosive condensation only. For cluster coarsening, the new algorithm can have the same improvement for numerical efficiencies for cluster transportation on empty lattices. However, as for the case $\gamma \in (2, 3)$ for the symmetric graph, the new algorithm would fail to capture the characteristic high background densities. This is because background particles would be regarded as clusters as well, and clusters are assumed never to split with the new algorithm. Therefore, all results in this thesis for systems that display coarsening dynamics are obtained using the original method.

Results from old and new algorithm

It remains for us to observe the quality of results for the new algorithm. For systems that demonstrate condensation and focusing on symmetric cases, $\sigma^2(t)$ is compared in Fig. 5.4 for different models and different d parameters. The results suggest an accurate depiction of condensation dynamics, especially for $d < 1$, when systems have lower background densities.

Chapter 6

Variations to the model

In this Chapter, we briefly discuss two variants of the models presented in the main findings of this study. Firstly, the models in Chapter 3 focus on cases with homogeneous graphs in the thermodynamic limit, where stationary product measures exist for the models. Weights can be conveniently written as a recursive function on the factorized transition rates. The asymptotic behaviour of the weights can therefore be computed and insights on the parameters, where the condensation transition occurs, can be found. In the case of the ECP, the model with rates (4.1) and (4.2), γ controls when condensation occurs. We introduce another model for which a a stationary product measure cannot be written in its general form, but explosive condensation exists and is controlled by both γ and d. This is discussed in Sec. 6.1.

Secondly, the IP demonstrates condensation when $d \to 0$, and the formation of the condensate is driven by the characteristics of cluster coarsening. For the models studied in Chapter 4, we focused on cases where $d \sim O(1)$. We have a mixture of results. Condensation can be reached by either nucleation dynamics followed by explosive condensation, or when coarsening behaviour reaches stationarity. An area of interest is to see how the ECP models evolve to condensation if $d \to 0$, and comparing them to the results of the IP. This is discussed in Sec. 6.2

6.1 Generalised model for comparison

We introduce another model that is similar to the models with rates (3.2) and (3.3), with attractive terms for both departure and receiving sites. The model's state space, lattice and update methods follow the set-up outlined in definitions 2.2. The transition rates are given by

$$c(\eta, \eta^{xy}) = (\eta_x^{\gamma_1})(\eta_y + d)^{\gamma_2} p(x, y) \,, \tag{6.1}$$

where the generator is written as

$$\mathcal{L}(f(\eta)) = \sum_{x \in \Lambda_L} p(x, y)(\eta_x^{\gamma_1})(\eta_y + d)^{\gamma_2} [f(\eta^x y) - f(\eta)] \,. \tag{6.2}$$

6.1.1 Stationary measure for generalised model

The model with rate (6.1) does not satisfy condition 3 in Theorem 2.2.1, so the generalised model does not have a stationary product measure. However, we can write down a stationary product measure by restricting our derivation to the symmetric graph case, which satisfies condition 2 in Theorem 2.2.1. The weights for this model in the form (2.12) are written as

$$W^{\text{gen}}(n) = \prod_{k=1}^{n} \frac{(k + d - 1)^{\gamma_2}}{k^{\gamma_1}} \,, \tag{6.3}$$

and similar to the weights for the previous models, (6.3) has no clear closed form analytical expression and the scaling behaviour is studied instead. Writing the logarithmic form and taking the k^{γ_2} term out, (6.3) is written as

$$W^{\text{gen}}(n) = \exp\left(\sum_{k=1}^{n} \ln \left(1 + \frac{d-1}{k}\right)^{\gamma_2} + (\gamma_2 - \gamma_1) \ln k \right) . \tag{6.4}$$

Within the range $\gamma_1 \neq \gamma_2$, the scaling relationship for $W^{\text{gen}}(n)$ is similar to the models in previous sections, as the $(\gamma_2 - \gamma_1) \ln k$ term dominates. The interesting case is when $\gamma = \gamma_2 = \gamma$. In this case, for $n \to \infty$, $\ln(1 + (d-1)/(k))^{\gamma} \to \gamma(d-1)/k$, where the contributions of smaller k's has no effect on the overall scaling. $W^{\text{gen}}(n)$ can be written as

$$W^{\text{gen}}(n) = \exp\left(\sum_{k=1}^{n} \ln \left(1 + \frac{d-1}{k}\right)^{\gamma} \right) \simeq \exp\left(\sum_{k=1}^{n} \frac{\gamma(d-1)}{k} \right) \sim n^{\gamma(d-1)} \,. \tag{6.5}$$

The scaling behaviours of $W^{\text{gen}}(n)$ are collected as

$$W^{\text{gen}}(n \to \infty) \simeq \begin{cases} n^{(\gamma_2 - \gamma_1)n} & \text{if } \gamma_2 \neq \gamma_1 \\ n^{\gamma(d-1)} & \text{if } \gamma_1 = \gamma_2 \,. \end{cases} \tag{6.6}$$

Similar to the derivation of $\rho(\phi)$ for the model with rate (3.2) in (3.25), the scaling of W^n can be substituted into the partition function to compute the radius of convergence for the density and second moment. We write the density as

$$\rho_{\text{gen}}(\phi > 0) = \frac{1}{z(\phi)} \sum_{n=0}^{\infty} (\lambda\phi)^n n^{\gamma(d-1)+1} = \begin{cases} \rho(\phi \leq 1) & \text{for } 0 < \phi \leq 1, \gamma(1-d) > 2 \\ \infty & \text{if } \phi > 1 \end{cases} , \tag{6.7}$$

where the convergence of ρ_{gen} depends on both γ and d. The same can be applied to the second moment, where n^2 is summed over instead of n. The second moment converges for

$$\sigma^2_{\text{gen}}(\phi > 0) = \begin{cases} < \infty & \text{for } \gamma(1-d) > 3, \phi \leq 1 \\ \infty & \text{if } \phi > 1 \end{cases} . \tag{6.8}$$

In the case $\rho > \rho(\phi = 1)$, the system experiences a phase transition where particles are divided into a fluid state and a condensate. This result is confirmed in the numerical evaluation of critical density ρ_c and critical second moment σ_c^2 against d in Fig. 6.1. Note that γ is fixed at $\gamma = 6$ in these cases. Similar to the plot in Fig. 3.8, two results are obtained by numerically evaluating $W(n)$ with different range of n. From (6.7), there is divergence at $d \to 2/3$ for the density. Similarly, there is be a divergence for second moment at $d \to 1/2$ from (6.8). Both of these cases can be shown on Fig. 6.1.

6.1.2 Condensation in the symmetric case

Explosive condensation is observed in the symmetric case; $\sigma^2(t)$ is plotted in Fig. 6.2 for the case $\gamma = 5$ and varying values for L. Despite showing signs of nucleation and rapid condensation, the time to condensation increases with system size, which is different from the condensation behaviour for the model with rates (4.1) and (4.2). It is unclear whether this is caused by a different timescale during the nucleation phase or other factors.

We extend our numerical study to the totally asymmetric case, which does not satisfy the criteria in Theorem (2.2.1). Explosive condensation that resembles the results in Chapter 4 is observed. Cases that display condensation are plotted in Fig. 6.3. From Fig. 6.3 it implies explosive condensation but it is dependent on both the choice of γ and $d \sim O(1)$. The exact scaling of $\langle T_{\text{SS}} \rangle$ is unclear. Insights on the scaling of $\langle T_{\text{SS}} \rangle$ might be obtained through further heuristic studies, where timescale approximations can be approximated using cluster interactions.

6.2 Vanishing diffusivity

The parameter d is regarded as system diffusivity, which controls the rate of particle drift when particle interactions do not exists. The choice of $d \sim O(1)$ is used nominally throughout the heuristic analysis in Chapter 4. In terms of the choice of parameters that lead to

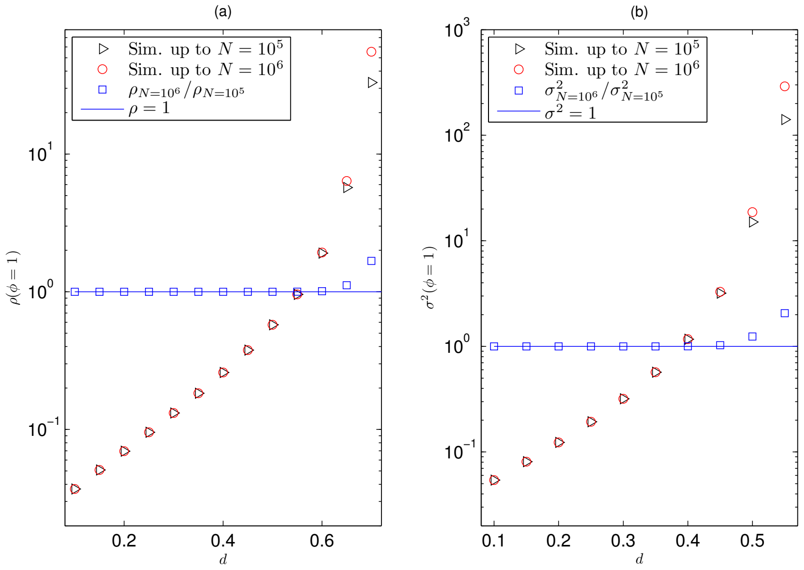

Figure 6.1: For $\gamma_1 = \gamma_2 = \gamma = 6$ and the model with rates (6.1). (a) $\rho(\phi = 1)$ is plotted against d, and (b) $\sigma^2(\phi = 1)$ is plotted against d. Black markers indicate when the solution is numerically obtained by evaluating (2.14) and (2.17) from $n = 0$ to $n = 10^5$, and the red marker is obtained by evaluating the respective partition functions from $n = 0$ to $n = 10^6$. The blue marker is the division of the two results. The blue marker will remain at 1 unless the numerical results diverges.

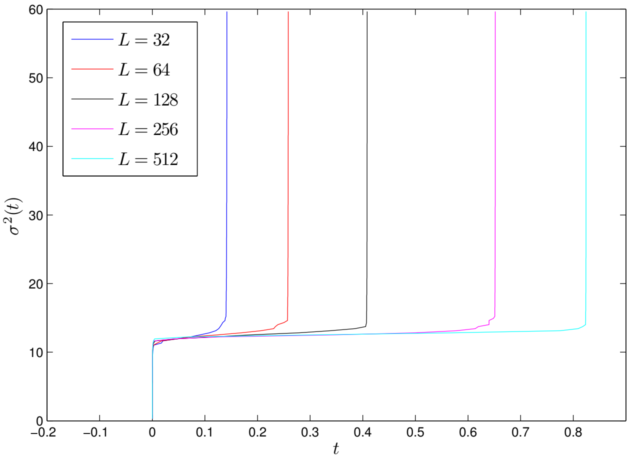

Figure 6.2: $\sigma^2(t)$ against t, for $\gamma = 5$, $d = 0.1$ on a symmetric graph. Only the beginning part of the condensation is plotted.

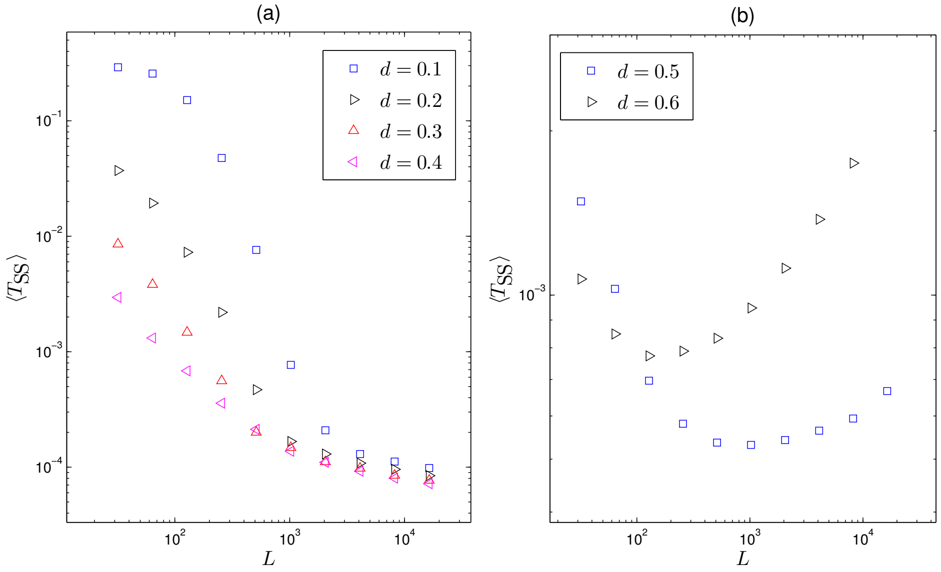

Figure 6.3: $\langle T_{SS} \rangle$ against L for $\gamma = 5$, model with rates (6.1) for the totally asymmetric case. As d enter the stationary weights as depicted in (6.7) and (6.8), different range of d results in the scaling of critical density and second moment. For (a) $d = 0.1 - 0.4$, where both critical density and second moment converges. This is in contrast with (b) $d = 0.5 - 0.6$, where the critical density converges but the critical second moment diverges. This case has similar stationary weights scaling as Sec. 4.5

condensation, the range of d is irrelevant as the diffusive terms are negligible in the case $\gamma_1 = \gamma_2$ for the stationary weights (3.24) and (3.33).

However, the heuristic arguments of models studied in Chapter 4 with vanishing diffusivity may have different results. This is implied in the study of Inclusion Process [54], where condensation does not exist for $d \sim O(1)$, but condensation is observed for $d < 1/N$. In Chapter 4, we have focused on the case $d \sim O(1)$ because we are interested in the heuristic arguments for explosive condensation. However, as we can see from the following arguments the coarsening time is strongly dependent on the choice of d, and condensation without explosion is observed.

For the model characterized by rates (4.1), the coarsening time (4.38) requires taking into account that clusters move with speed $v(m) \sim d^{-\gamma} m^{\gamma-1}$. For this model, the time for coarsening to finish is revised as

$$T_{\text{Co}}^{\text{sym}} \sim d^{-\gamma} L^{3-\gamma} \tag{6.9}$$

for the symmetric case. Similarly, the coarsening time for the totally asymmetric case is

$$T_{\text{Co}}^{\text{asym}} \sim d^{-\gamma} L^{1-\gamma}. \tag{6.10}$$

For $d \to 0$ this clearly indicates that coarsening takes a much longer time to complete compared to the nucleation phase, providing that the critical occupation number is not reached. The critical occupation number for the symmetric case is given by

$$\frac{L^2}{d^\gamma m_c^{\gamma-1}} \ll 1 \,, \tag{6.11}$$

and for the totally asymmetric case,

$$\frac{L}{d^\gamma m_c^{\gamma}} \ll 1 \,. \tag{6.12}$$

For both cases, $m_c \gg L$ for $d \to 0$. Therefore, the nucleation can never reach the critical occupancy number. Therefore the system reaches its condensate from cluster coarsening. A numerical example of this result is shown in Fig. 6.4, which is accompanied by configuration plots at crucial times of the system.

In Fig. 6.4, coarsening behaviour continues towards reaching the condensate. As stationarity is reached, the system is still in a coarsening state. The second moment towards stationarity increases rapidly, followed by a short period of waiting time, which is characteristic of coarsening behaviour. The same heuristic arguments can be used for the system with rate (4.2), where the factor $d^{-\gamma}$ is replaced by d^{-1}, for (6.9) to (6.12). Insights to this case can be explored further by solving the exact evolution of σ^2 using heuristic arguments

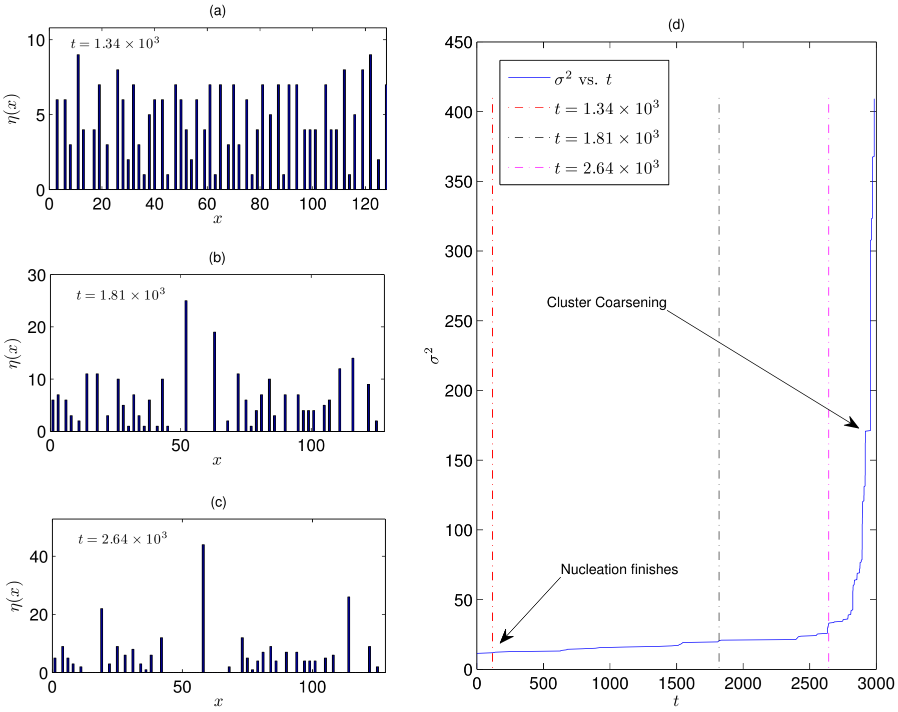

Figure 6.4: Schematic representation when $d \to 0$. For $\gamma = 5$, $d = 10^{-7}$, $\rho = 2$, $L = 128$, symmetric graph with rates (4.1). (a) Nucleation finishes at approximately this instant. Nucleation finishes with clusters at generally low occupancies to examples with higher d. (b) Coarsening process is a relatively lengthy process compared to the nucleation times. (c) Moment before reaching stationarity, and clusters of size $\sim O(L)$ are dominating. (d) Second moment vs. time for the process, with dashed line representing the three instances of which the complete configurations are plotted. The time when nucleation finishes and the characteristic coarsening increase in second moment are labelled.

similar to the ones used in Chapter 4.

6.3 Discussion

In this Chapter, two different variations to the models proposed in Chapter 4 are studied, where these two cases represent two different directions to proceed from the variants of the ECP models. It should be noted that for both cases, the number of particles in the system is conserved and the study is limited to the thermodynamic limit.

For the first case (see Sec. 6.1), the rates are chosen such that the weights of the stationary measure no longer scale with γ only, but also with d. It should be noted that this model only has stationary product measures for a specific choice of graph, as the general case of this model does not hold for condition 3 in Theorem 2.2.1. Interesting transition behaviours are observed, as the model condenses in different ranges of d. The model displays a surprisingly rich variety of behaviour, as both explosive condensation and non-explosive condensation is observed for different choice of d.

For the second case (see Sec. 6.2), we study the condensation behaviour for the variants of the ECP model when $d \to 0$. The motivation is that the IP [54] demonstrates interesting dynamical behaviour in this range. The IP is observed to have a phase transition only when $d \to 0$, and the microscopic dynamics study suggests that there is a clear separation between the nucleation and coarsening regime, which is not observed in ECP for $d \sim O(1)$. We observe a clearer distinction between nucleation and coarsening for ECP when $d \to 0$. The formation of the condensate is different from that studied in Chapter 4, and in particular there is no explosive condensation since the motion of clusters is slowed down.

Chapter 7

Conclusion and Outlook

In this chapter we summarise the main findings of the thesis and give a general outlook for future areas of study. A brief summary of each chapter is provided chronologically, and areas of studies will be found at the very end.

In this thesis, we considered several interacting particle models that demonstrate condensation behaviours. We are particularly interested in systems that are ergodic on finite systems on a homogeneous lattice. The long time behaviour of the system from arbitrary initial conditions to stationarity is characterized by the canonical stationary product measures. The criteria for the existence of stationary product measures for models with factorized hop rates are introduced. Large deviations of the maximum site occupation are discussed. Phase transitions from a homogeneous and uniformly distributed state to one that has a fraction of mass concentrated at a localized site are studied. Under this set up, condensation transitions for several models in the literature are reviewed, such as the zero-range process, inclusion process and the explosive condensation process. All three models have stationary product measures, but with very different dynamic condensation behaviours.

In Chapter 3, we introduce two models that have similar stationary product measures as the explosive condensation model. By studying the scaling of stationary weights, we are able to identify the choice of parameters that could lead to a phase transition. Identifying and isolating the super-exponential cases of the stationary weights, we focus on the case when $\gamma_1 = \gamma_2 = \gamma$ for models with rates (3.2) and (3.3). In this regime, finite system moments exist only for a certain range of γ. The characteristics of explosive condensation are introduced schematically. Dynamics towards the formation of a condensate are seemingly dominated by distinctive phases. We attempted to solve for exact observable solutions for these models, but this proves difficult.

In Chapter 4, we use a microscopic approach to study the formation of condensates for the models introduced in Chapter 3. Several stages of the dynamics are identified.

The formation of condensates depend on a mixture of distinctive nucleation and coarsening effects, and the system enters an "explosive condensation" stage when some critical occupancy number is reached by the biggest cluster in the system. We provide a detailed study on the physical properties of clusters. The speed of cluster movement and the stochasticity property of the exchange of particles are discussed. Understanding the cluster dynamics is pivotal to heuristic analysis of the timescales of the distinctive stages mentioned above. This is also useful in the numerical efficiencies, which are discussed in Chapter 5. Two different paths to condensation are outlined. For both cases the initial distribution of particles is important for the general scaling of the time to condensation $\langle T_{\mathrm{SS}} \rangle$. Instantaneous condensation as $L \to \infty$ is observed for both symmetric and totally asymmetric cases, and the scaling of $\langle T_{\mathrm{SS}} \rangle$ is derived. These results are supported by numerical results for $L > 10^4$ for both symmetric and totally asymmetric cases.

In Chapter 5, we discuss the issues of costs of numerical simulations, and propose improvements for numerical simulation for systems that demonstrates explosive condensation. An algorithm is proposed, that simplifies the simulation of a moving cluster yet preserves stochasticity of particle interactions. The limitations of these methods are discussed. These methods are shown to be stable for $d \sim O(1)$ and $\gamma > 3$, and are used for simulating the main results with explosive condensation in Chapter 4. A brief explanation for averaging monotonically increasing observables in explosive condensation is also discussed.

In Chapter 6, we briefly discuss variations for the models studied in this thesis. This includes the case $d \to 0, \gamma_1 = \gamma_2 = \gamma$ for the two models introduced in Chapter 3. This case demonstrates condensation, but the formation of condensate is different in the microscopic perspective. We also look into a model that is similar to ECP models but with no canonical stationary product measures. This model is of interest, because for its symmetric case, explosive condensation is observed and is dependent on both γ and d.

Several interesting and important open questions follow directly from the work in this thesis. The natural progression of the study is extending the explosive condensation to inhomogeneous graphs, and observe how phase separation of the fluid state and the condensate would manifest in such cases. Also interesting is to study cases where mass of the system might not be conserved, e.g. in systems with open boundaries. From Chapter 6, the condensation of the toy model from a microscopic perspective can be studied further, as it provides insights to condensation where no stationary product measures exists. It is also particularly interesting to consider the explosive condensation models on wealth distribution. This is because the set up of explosive condensation system is particularly suitable for interacting rules in agrarian economies, where total wealth is conserved. This would be different from the conventional econophysics approach, where the stochasticity of IPS would provide better insights on topics such as information economics.

Appendix A

Criteria for stationary product measures

Here, we proof that Theorem (2.2.1) is true, the full derivation can be found in Sec. 2 of [23]. We have to show for expected values w.r.t. ν_ϕ that

$$\nu_\phi^\Lambda(\mathcal{L}f) = \sum_{\eta\in X^\Lambda} \sum_{x,y\in\Lambda} p(x,y)u(\eta_x)v(\eta_y)(f(\eta^{xy}) - f(\eta))\nu_\phi^\Lambda(\eta) = 0 \tag{A.1}$$

for all local observables f. For fixed x, y the change in variable leads to

$$\sum_{\eta\in X^\Lambda} u(\eta_x)v(\eta_y)f(\eta^{xy})\nu_\phi^\Lambda(\eta) = \sum_{\eta\in X^\Lambda} u(\eta_x + 1)v(\eta_y - 1)f(\eta^{yx})\nu_\phi^\Lambda(\eta)\,. \tag{A.2}$$

From the partition function derivations in Sec. 2.2.3, the marginals imply that for all $x, y \in \Lambda$ and $n \geq 0$, $k \geq 1$

$$\nu_\phi(n+1)\mu_\phi(k-1)u(n+1)v(k-1) = \nu_\phi(n)\mu_\phi(k)u(k)v(n) \tag{A.3}$$

Plugging this into (A.1),

$$\sum_{\eta\in X^\Lambda} f(\eta)\nu_\phi^\Lambda(\eta) = \sum_{x,y\in\Lambda} p(x,y)\,(u(\eta)v(\eta)) \tag{A.4}$$

and exchanging the summation variables $x \leftrightarrow y$ in the first part of the equation leads to

$$\nu_\phi^\Lambda(\mathcal{L}f) = \sum_{\eta\in X^\Lambda} f(\eta)\nu_\phi(\eta) \sum_{x\in\Lambda} u(\eta_x) \sum_{y\in\Lambda} v(\eta_y)(p(y,x)) - p(x,y))\,. \tag{A.5}$$

This clearly vanishes in the first two cases and analogously to the above argument one can show that in the second case, detailed balance implies

$$\nu_\phi^\Lambda(f\mathcal{L}g) = \nu_\phi^\Lambda(g\mathcal{L}f) \quad \text{for local functions } f, g \quad , \tag{A.6}$$

therefore ν_ϕ^Λ is reversible. For the homogeneous case 3, we get

$$\nu_\phi^\Lambda(\mathcal{L}f) = \sum_{\eta\in X^\Lambda} f(\eta)\nu_\phi(\eta) \sum_{x\in\Lambda} u(\eta_x) \sum_{y\in\Lambda} (p(y,x) - p(x,y)) \, , \tag{A.7}$$

which vanishes due to condition 3 in (2.2.1).

Appendix B

Computational Methods

In this section, we provide supplementary materials for Chapter 5, which summarises the numerical methods used for computing the results in Chapter 3, 4 and 6. This section is comprised of two parts.

Firstly we outline the standard approach to simulate continuous-time Markov processes. This includes the supplementary materials to the Gillespie algorithm and the binary tree method that is used in obtaining the numerical results in this thesis. This corresponds to the explanation of numerical methods presented in Sec. 5.2.

Secondly, the details of the new algorithm as mentioned in Sec. 5.3 is provided. The new algorithm is a three-stage process that shortens simulation time by providing an accurate estimation of cluster speed. Essentially, all three stages uses the standard Gillespie method, but each stage uses a different set of rates and graph. The interchange between these stages are controlled by specific cut-off conditions as elaborated in Sec. 5.3. The implementation of this new algorithm ensures improved numerical efficiencies for simulating EPS, and also preserves key stochastic properties of cluster mass exchange. This method is first developed in this study, and has been subsequently used in other IPS research [54].

B.1 Gillespie Algorithm

The Gillespie algorithm [75] (also called the Doob-Gillespie algorithm) is the standard numerical method to simulate the sample path of a continuous time Markov chain. If $(c_i)_i = 1^L$ are the rates of possible transitions out of the current state, the system waits for an exponentially distributed time with rate $C_L = \sum_i c_i$, and then performs a transition i chosen with probability c_i/C. The detail workings are presented in Algorithm 1.

Algorithm 1 Basic Gillespie Algorithm for totally asymmetric inclusion process

```
Require: List of the $L$ jumps rates at each site in the current state $(c_i)_{i=1}^L$
Require: The partial sums $C_L = \sum_{i=1}^L c_i$ and $C_0 = 0$
  { Sample time increment from exp($C_L$) }
  $dt \leftarrow$ Exponentially distributed random number with mean $1/C_L$
  $t \leftarrow t + dt$
  {Choose to move particle of site $x$ with probability $c_x/C_L$ }
  $r \leftarrow$ Uniform random number on $[0, C_L)$
  Perform a binary search for $x$ such that $C_{x-1} \leq C_x$
  $\eta_x \leftarrow \eta_x - 1$
  $\eta_{x+1} \leftarrow \eta_x + 1$
  {Updating rates and partial sums}
  Update rates $c_x$ and $c_{x+1}$
  Update partial sum $C_n \mathrm{for} n \in \{\min\{c_x, c_{x+i-1}, ..., L\}\}$
```

B.2 Binary Search Tree

For large systems, searching through rates of all possible jumps can be numerically expensive. A binary search tree is used to improve the efficiencies of this process, which is described in Sec. 5. For a complete graph, a single search will take $\sim L^2$ steps using linear search methods. The same process will take $\sim \log(L^2)$ steps to complete on a binary search tree. The computational complexity will be $\frac{L\ln(2)}{2\ln(L)}$. The detail workings of this method are presented in Algorithm 2.

Algorithm 2 Binary search tree for general IPS models

```
  {Preparing how rates are organised in a binary search tree}
Require: A list $B^l_j$ such that $l \in \{0, 1, 2, ...K\}$, $K = \lceil \frac{2\ln(L)}{\ln(2)} \rceil$.
Require: Letting $B^0_j = r_j$
  for $l = 1, l++, l = K$ do
    $B^l_j = B^{l-1}_{2j} + B^{l-1}_{2j+1}$
  end for
  $r \leftarrow$ uniform random number $\in [0, B^K_0)$.
  {Search through the binary search tree }
  $j \leftarrow 0$
  for $l = K, l--, l = 1$ do
    If $\{B^{l-1}_{2j} \geq \rho\}$
    $j \leftarrow 2j$
    Else
    $j \leftarrow 2j + 1$
    $\rho \leftarrow \rho - B^{l-1}_{2j}$
  end for
  Update $\eta$ according to jump $j$
  Update $r_j$
```

B.3 Cluster dynamics simplification

Algorithm 3 describes the numerical simplification that is introduced in Chapter 5. In a nutshell, there are three stages.

1. In the beginning it uses the same Monte Carlo method in the original algorithm, where rates are stored in a binary tree. The initial stages of the dynamics are equivalent to the conventional IPS numerical method, which is elaborated in Algorithm 1 and 2. This is terminated when the strict cut-off condition $\sum_{x\in\Lambda}\eta_x\eta_{x+1} = 0$ between the nucleation and coarsening stage is reached.
2. When clusters are all separated by empty spaces, the dynamics are simplified by considering the movement of entire clusters as one single step. Therefore, another separate set of Monte Carlo interactions are simulated using the Gillespie method based on the cluster interaction rates q_i's. Entire clusters will be moved after each step, unless the clusters are perceived to be moving to a site shared by another cluster. In such a scenario, the stochasticity of cluster-cluster interaction has to be considered and another mechanism is temporarily introduced, as explained in the third stage.
3. To preserve the stochasticity of mass exchange between clusters, a random walk on a triangle lattice is introduced. The triangle lattice is elaborated in detail in Fig. 5.2. If the system meets the exit conditions of the random walk (boundaries of the triangle), then this will revert back to the previous step.

Algorithm 3 Adopted Algorithm for simulating symmetric nearest neighbour ECP

```
Require: List of occupancies $(\eta_i)_{i=1}^{L}$ and temporary list $(\eta'_i)_{i=1}^{L}$
Require: Compute list of rates $(c_i)_{i=1}^{2L}$ and partial sums $C_n = \sum_{i=1}^{n} c_i$ up to $n = 2L$
  {The first stage: conventional numerical method}
  while $\sum_{x\in\Lambda}^{L} \eta_x \eta_{x+1} > 0$ do
    $r \leftarrow$ uniform random number on $[0, C_{2L})$
    Perform a binary search for $x$ such that $C_{x-1} \leq r \leq C_x$
    Updating respective occupancies in $\eta'$ (not $\eta$)
    $dt \leftarrow$ Exponentially distributed random number with mean $1/C_L$
  end while
  {Second stage: cluster-cluster interactions}
  Compute list of rates $(s_i)_{i=1}^{2L}$ such that $S_n = \sum_{i=1}^{n} s_i$, where $s_i$'s are computed by cluster rates
  $r' \leftarrow$ uniform random number on $[0, S_{2L})$
  Perform search for $x'$ such that $S_{x'-1} \leq r' < S'_x$
  if For after $\eta' \leftarrow \eta^{xy}$ and $\sum_{x\in\Lambda}^{L} \eta'_x \eta'_{x+1} = 0$ then
    {Cluster moving on empty space }
    $\eta_{x+1} \leftarrow \eta_{x+1} + \eta_x$
    $\eta_x \leftarrow 0$
  else
    {Third stage: random walk on triangle lattice}
    $a_1 \leftarrow \eta'_x$ and $a_2 \leftarrow \eta'_{x+1}$ and $A \leftarrow a_1 + a_2$
    while $a_1 + a_2 \neq A$ and $a_1 + a_2 \neq 0$ do
      Compute list of rates $(q_j)_{j=1}^{4}$ for a particle to random walk
      Compute $Q_n = \sum_{i=1}^{n} q_i$
      $r'' \leftarrow$ uniform random number on $[0, Q_n)$
      Perform a search for $x''$ such that $Q_{x''-1} \leq r'' < Q_{x''}$
      Update $a_1$ or $a_2$ depending on the index associated with $x''$
    end while
    $\eta'_x \leftarrow a_1$ and $\eta'_{x+1} \leftarrow a_2$
    $\eta_x \leftarrow \eta'_x$ and $\eta_{x+1} \leftarrow \eta'_{x+1}$
  end if
  $dt \leftarrow$ Exponentially distributed random number with mean $1/\eta_x^{\gamma-1}$
  $t \leftarrow t + dt$
```

Appendix C

Solution for time to steady state by Waclaw and Evans

The following is a reproduction of the argument for explosive condensation in [6]. After the original period of exchange, $k = N/m$ piles of clusters are formed, where N is the total mass of the system and m is the average mass of one cluster. For a totally asymmetric lattice, clusters move in the same direction with varying speed and gains mass as collision occurs. Eventually, a condensate forms as one cluster gains enough mass to move significantly faster than other clusters.

Each cluster has a respective time to dominance $T_1, T_2, T_3 \ldots T_k$. The time to condensate T_{SS} is therefore the minimal time

$$T_{\mathrm{SS}} = \min\{T_1, \ldots, T_k\} \,. \tag{C.1}$$

In the process of mass gaining, a cluster with mass m gains Δm in successive steps. The mass of the cluster at the n^{th} step is therefore

$$m_n = m_{n-1} + \Delta m_n \,, \tag{C.2}$$

and the corresponding time for successive steps is given by

$$t_n = t_{n-1} + \Delta t_n \,. \tag{C.3}$$

The Δt_n 's are exponentially distributed and is given by

$$p_n(\Delta t_n) = \lambda_n e^{-\lambda_n \Delta t_n} \,. \tag{C.4}$$

Note that $\lambda_n \sim 1/\langle \Delta t_n \rangle$ is the rate for the distribution of waiting times Δt_n. The estimation

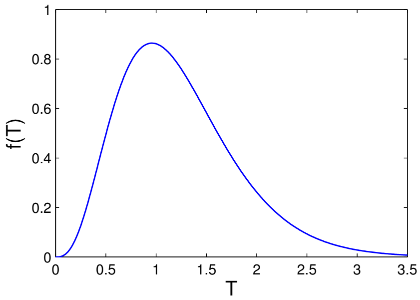

Figure C.1: $f(T)$

of λ_n by Waclaw and Evans is based on the assumption that each cluster evolves independently, and that distances between clusters are negligible. This is often true in certain ranges of parameters in the totally asymmetric graph and over some parameters for the symmetric case. Fluctuations are ignored. And from this assumption, $\lambda_n^{\text{asym}} \propto m_n^{\gamma}$, which is the reciprocal of the waiting time for one cluster to move one space on the lattice. Note that Δm_n increases mostly linearly for the totally asymmetric case, as explained in Sec. 4.2.2, therefore $m_n \sim n$, and $\lambda_n^{\text{asym}} \propto n^{\gamma}$.

The probability distribution $f(T)$, which $T = \Delta t_1 + \Delta t_2 + ...$ can be calculated as T is assumed to be a sum of independent exponential random variables. $f(T)$ is hypothesized as having the shape given in Fig. C.1. $f(T)$ is therefore given as

$$f(T) = \frac{1}{2\pi} \int_{\infty}^{\infty} d\omega e^{i\omega T} \bar{f}(\omega) \,, \tag{C.5}$$

where $\bar{f}(\omega)$ is the product of characteristic functions of the exponential distribution Eq. (C.4)

$$\bar{f}(\omega) = \prod_{n=1}^{\infty} \bar{p}_n(\omega) = \prod_{n=1}^{\infty} \frac{1}{1 - i\omega/\lambda_n} \,. \tag{C.6}$$

From Eq. (C.6), the large ω behaviour can be found using the saddle point approximation and the large T behaviour can be recovered using the Fourier transform. Then, using the definition of T_{SS} in Eq. (C.1) and extreme value statistics, the distribution of T_{SS} can be obtained, and solved for $\langle T_{\text{SS}} \rangle$. The details of this derivation can be found in [6] and the supplementary material to [59]. The time to steady state $\langle T_{\text{SS}} \rangle$ is estimated as

$$\langle T_{\text{SS}} \rangle_{\text{asym}} = c_2 (c_3 + \ln(L))^{1-\gamma} \,, \tag{C.7}$$

where c_2 and c_3 are real positive constants, and c_3 can be dependent on the fluctuation of the distribution.

The same derivation can be applied to competing clusters on a symmetric graph but with a cautious consideration on the choice of λ_n^{sym}. Assuming particles move through a largely intact background density without clusters surrounded by empty sites, then $\lambda_n^{\text{sym}} \sim m_n^{\gamma-1}$. From Fig. 4.9, it is established that $\Delta m \propto m$. Clusters exchange a proportion of their own mass in each collision. For each collision there are $k\rho L$ particles exchanged, where constant k represents the average fraction of the particles exchanged. Therefore at the n^{th} collision, there are $m_n \propto nk\rho L$. This gives $\lambda_n \propto (nk\rho L)^{1-\gamma}$. Using the same arguments for the derivation of $P(T_{\text{SS}})$, $\langle T_{\text{SS}} \rangle$ is obtained

$$\langle T_{\text{SS}} \rangle_{\text{sym}} = c_2(c_3 + \ln(L))^{2-\gamma} \,. \tag{C.8}$$

However, as explained in previous sections, clusters are likely to be separated by empty sites in the coarsening regime. The derivation of λ_n is determined from the average collision time for the totally asymmetric and the symmetric case respectively. Such that: $\lambda_n^{\text{asym}} = m_n^{\gamma-1}\rho \sim m_n^{\gamma-1}$ for the totally asymmetric case and $\lambda_n^{\text{sym}} = m_n^{\gamma-3}\rho^2 \sim m_n^{\gamma-3}$ for the symmetric case.

While $m_n \sim n$ for both the totally asymmetric case and symmetric cases, as explained previously. The reciprocal of the waiting times after n collision for the totally asymmetric case is given by

$$\lambda_n^{\text{asym}}\rho \sim n^{\gamma-1} \,,$$

and for the symmetric case

$$\lambda_n^{\text{sym}} \sim n^{\gamma-2} \,.$$

The $\langle T_{\text{SS}} \rangle$ scaling for the totally asymmetric case is therefore given by

$$\langle T'_{\text{SS}} \rangle_{\text{sym}} = c_2(c_3 + \ln(L))^{2-\gamma} \,, \tag{C.9}$$

and for the symmetric case this is given by

$$\langle T'_{\text{SS}} \rangle_{\text{sym}} = c_2(c_3 + \ln(L))^{3-\gamma} \,. \tag{C.10}$$

The limitation of this method is that, while mass in the entire system is conserved, clusters at the later stages do not evolve independently. While Waclaw and Evans focused on the totally asymmetric graph, the same principles can be applied to the symmetric case. From Eq. (4.18), the speed of a cluster in symmetric graph scales as $v(m) \propto m^{\gamma-1}$.

Since λ_n is the normalization term for the distribution of waiting times before successive collisions up to n steps, both the growth of m_n and distance travelled before hitting another cluster should be considered.

Comparison to Waclaw and Evans' $\langle T_{\text{SS}} \rangle$ scaling

Waclaw and Evans provided a scaling for the time for the whole model to reach the steady state $\langle T_{\text{SS}} \rangle$ [6] and is given in Eq. (C.7). While this provides an accurate description to the totally asymmetric model that was presented in the original model, this might not hold for the symmetric graph. The alternative scaling properties are introduced in Eq. (C.8), (C.9) and (C.10) are used to compare with numerical results in Chapter 4 for $\langle T_{\text{SS}} \rangle$ for the model characterized by (3.3) in the symmetric graph. From the results presented in Chapter 4, the scaling properties of Eq. (C.7), Eq. (C.8),Eq. (C.9) and (C.10) may not be easily distinguishable from numerical data.

Appendix D

Critical densities and second moment

The critical densities ρ_c and the corresponding second moment $\sigma^2_\infty(\phi = 1)$ of the interacting particle system can be numerically evaluated in Eq. (2.16) and Eq. (2.18), as explained in Sec. 2.2.3.

Below are tables outlining the critical densities and second moment of some of the parameters for simulated results throughout this thesis. While only some of the results are used in simulations presented in this study, other values are provided for comparison. Critical density diverges at $\gamma \searrow 2$ and the finite critical second moment diverges at $\gamma \searrow 3$.

For all the simulations in this thesis, densities are typical chosen such that $\rho > \rho_c$. It is also worth mentioning that as $d \to 0$, the rates of (4.1) and (4.2) coincide, and this leads to the same critical densities and critical second moment.

d/γ	2.25	2.5	2.75	3	4	4.5	5	6	7
10^{-7}	1.99	0.943	0.557	0.368	0.111	0.0683	0.0438	0.0193	0.00892
0.01	2.02	0.958	0.567	0.372	0.112	0.0690	0.0442	0.0194	0.00901
0.05	2.15	1.02	0.607	0.386	0.116	0.0716	0.0459	0.0202	0.00936
0.1	2.31	1.10	0.659	0.403	0.121	0.0749	0.0480	0.0211	0.00980
0.2	2.65	1.27	0.766	0.437	0.132	0.0814	0.0523	0.0230	0.0107
0.3	3.00	1.45	0.877	0.471	0.142	0.0879	0.0565	0.0249	0.0116
0.4	3.38	1.64	0.994	0.505	0.152	0.0943	0.0607	0.0268	0.0125
0.5	3.78	1.83	1.12	0.538	0.162	0.101	0.0648	0.0287	0.0133
1	6.15	2.97	1.81	0.700	0.212	0.132	0.0854	0.0380	0.0177

Table D.1: Critical density for the model characterized by rates Eq. (3.2).

d/γ	2.25	2.5	2.75	3	4	4.5	5	6	7
10^{-7}	1.99	0.943	0.557	0.368	0.111	0.0683	0.0438	0.0193	0.00892
0.01	2.01	0.952	0.562	0.375	0.113	0.0700	0.0450	0.0199	0.00925
0.05	2.09	0.988	0.583	0.404	0.124	0.0772	0.0500	0.0225	0.0106
0.1	2.20	1.03	0.610	0.440	0.137	0.0865	0.0566	0.0259	0.0125
0.2	2.40	1.13	0.662	0.515	0.166	0.107	0.0710	0.0337	0.0169
0.3	2.60	1.22	0.714	0.594	0.197	0.128	0.0868	0.0425	0.0220
0.4	2.81	1.31	0.766	0.677	0.230	0.152	0.104	0.0523	0.0278
0.5	3.01	1.40	0.817	0.763	0.265	0.177	0.122	0.0631	0.0344
1	4.03	1.84	1.07	1.25	0.460	0.319	0.230	0.129	0.0772

Table D.2: Critical density for the model characterized by rates Eq. (3.3).

d/γ	4	4.5	5	6	7
10^{-7}	0.286	0.131	0.0698	0.0250	0.0104
0.01	0.289	0.132	0.0704	0.0252	0.0105
0.05	0.300	0.137	0.0731	0.0262	0.0109
0.1	0.313	0.143	0.0764	0.0274	0.0114
0.2	0.340	0.155	0.0830	0.0298	0.0125
0.3	0.366	0.167	0.0896	0.0323	0.0135
0.4	0.392	0.179	0.0961	0.0347	0.0145
0.5	0.418	0.191	0.102	0.0370	0.0155
1	0.543	0.249	0.134	0.0488	0.0206

Table D.3: Finite critical second moment $\sigma^2(\phi = 1)$ for the model characterized by rates Eq. (3.2).

d/γ	4	4.5	5	6	7
10^{-7}	0.286	0.131	0.0698	0.0250	0.0104
0.01	0.295	0.135	0.0720	0.0259	0.0108
0.05	0.329	0.151	0.0811	0.0295	0.0125
0.1	0.374	0.173	0.0935	0.0345	0.0149
0.2	0.476	0.222	0.121	0.0460	0.0205
0.3	0.592	0.278	0.153	0.0595	0.0271
0.4	0.723	0.341	0.190	0.0750	0.0350
0.5	0.868	0.412	0.231	0.0926	0.0440
1	1.84	0.882	0.504	0.213	0.108

Table D.4: Finite critical second moment $\sigma^2(\phi = 1)$ for the model characterized by rates Eq. (3.3).

γ/d	0.1	0.2	0.3	0.4	0.5	0.6
5	0.0789	0.1422	0.264	0.534	1.40	9.20
6	0.0371	0.0696	0.132	0.259	0.575	1.91

Table D.5: Critical density for the model characterized by rates Eq. (6.1).

γ/d	0.1	0.2	0.3	0.4	0.5
5	0.155	0.388	1.36	13.6	N/A
6	0.0542	0.123	0.319	1.17	15.1

Table D.6: Critical second moment for the model characterized by rates Eq. (6.1).

Bibliography

[1] Yu-Xi Chau, Colm Connaughton, and Stefan Grosskinsky. Explosive condensation in symmetric mass transport models. *Journal of Statistical Mechanics: Theory and Experiment*, 2015(11):P11031, 2015.
1 citation(s) on 1 page(s): v,

[2] K Huang. *Statistical Mechanics*. Wiley, 1987.
1 citation(s) on 1 page(s): 2,

[3] David Ruelle. *Statistical Mechanics: Rigorous results*. World Scientific, 1969.
1 citation(s) on 1 page(s): 2,

[4] Hans-Otto Georgii. *Gibbs measures and phase transitions*, volume 9. Walter de Gruyter, 2011.
1 citation(s) on 1 page(s): 2,

[5] Martin R Evans and Tom Hanney. Nonequilibrium statistical mechanics of the zero-range process and related models. *Journal of Physics A: Mathematical and General*, 38(19):R195, 2005.
6 citation(s) on 5 page(s): 2, 4, 13 (2), 17, and 43,

[6] Bartłomiej Waclaw and Martin R. Evans. Explosive condensation in a mass transport model. *Phys. Rev. Lett.*, 108:070601, Feb 2012.
28 citation(s) on 21 page(s): 2, 3, 20 (2), 23 (2), 24, 28 (2), 30, 41, 43, 44, 47, 52, 58 (3), 68, 69, 90 (3), 91, 95, 120, 121, and 123,

[7] Thomas Piketty and Gabriel Zucman. Capital is back: Wealth-income ratios in rich countries, 1700-2010. 2013.
1 citation(s) on 1 page(s): 3,

[8] Peter Turchin and Sergey A Nefedov. *Secular cycles*. Princeton University Press, 2009.
1 citation(s) on 1 page(s): 3,

[9] Frank Spitzer. Interaction of markov processes. *Advances in Mathematics*, 5(2):246–290, 1970.
4 citation(s) on 3 page(s): 4, 13 (2), and 15,

[10] Thomas M Liggett. An infinite particle system with zero range interactions. *The Annals of Probability*, pages 240–253, 1973.
5 citation(s) on 5 page(s): 4, 5, 6, 8, and 13,

[11] Roland L'vovich Dobrushin. Gibbsian random fields for lattice systems with pairwise interactions. *Functional Analysis and its applications*, 2(4):292–301, 1968.
2 citation(s) on 1 page(s): 4 (2),

[12] Roland L'vovich Dobrushin. Markov processes with a large number of locally interacting components: existence of a limit process and its ergodicity. *Problemy peredachi informatsii*, 7(2):70–87, 1971.
1 citation(s) on 1 page(s): 4,

[13] Thomas M. Liggett. *Interacting Particle Systems*. Springer Berlin Heidelberg, 1985.
3 citation(s) on 3 page(s): 4, 5, and 16,

[14] David Griffeath. Frank spitzer's pioneering work on interacting particle systems. *The Annals of Probability*, pages 608–621, 1993.
1 citation(s) on 1 page(s): 4,

[15] Stephan Luckhaus and Livio Triolo. The continuum reaction-diffusion limit of a stochastic cellular growth model. *Rend. Mat. Acc. Lincei*, 15:215–223, 2004.
1 citation(s) on 1 page(s): 4,

[16] Simon A Levin and R Durrett. From individuals to epidemics. *Philosophical Transactions of the Royal Society of London. Series B: Biological Sciences*, 351(1347):1615–1621, 1996.
1 citation(s) on 1 page(s): 4,

[17] John Angle. The inequality process as a wealth maximizing process. *Physica A: Statistical Mechanics and Its Applications*, 367:388–414, 2006.
1 citation(s) on 1 page(s): 4,

[18] J Kaupužs, R Mahnke, and RJ Harris. Zero-range model of traffic flow. *Physical Review E*, 72(5):056125, 2005.
3 citation(s) on 3 page(s): 4, 14, and 22,

[19] Kai Nagel, Peter Wagner, and Richard Woesler. Still flowing: Approaches to traffic flow and traffic jam modeling. *Operations research*, 51(5):681–710, 2003.
2 citation(s) on 2 page(s): 4 and 22,

[20] MG Smolik, S Dullinger, F Essl, I Kleinbauer, M Leitner, J Peterseil, L-M Stadler, and G Vogl. Integrating species distribution models and interacting particle systems to predict the spread of an invasive alien plant. *Journal of Biogeography*, 37(3):411–422, 2010.
1 citation(s) on 1 page(s): 4,

[21] Daniela Morale, Vincenzo Capasso, and Karl Oelschläger. An interacting particle system modelling aggregation behavior: from individuals to populations. *Journal of mathematical biology*, 50(1):49–66, 2005.
1 citation(s) on 1 page(s): 4,

[22] Eric Bouvier, Eyal Cohen, and Laurent Najman. From crowd simulation to airbag deployment: particle systems, a new paradigm of simulation. *Journal of Electronic imaging*, 6(1):94–107, 1997.
1 citation(s) on 1 page(s): 4,

[23] Paul Chleboun and Stefan Grosskinsky. Condensation in stochastic particle systems with stationary product measures. *Journal of Statistical Physics*, 154(1-2):432–465, 2014.
7 citation(s) on 7 page(s): 5, 6, 12, 17, 18, 90, and 113,

[24] Stefan Großkinsky, Gunter M Schütz, and Herbert Spohn. Condensation in the zero range process: stationary and dynamical properties. *Journal of statistical physics*, 113(3-4):389–410, 2003.
8 citation(s) on 6 page(s): 5, 11 (2), 15 (2), 17, 43, and 90,

[25] Inés Armendáriz and Michail Loulakis. Thermodynamic limit for the invariant measures in supercritical zero range processes. *Probability theory and related fields*, 145(1-2):175–188, 2009.
2 citation(s) on 2 page(s): 11 and 15,

[26] Intae Jeon, Peter March, and Boris Pittel. Size of the largest cluster under zero-range invariant measures. *Annals of probability*, pages 1162–1194, 2000.
3 citation(s) on 3 page(s): 11, 15, and 90,

[27] C Godreche. From urn models to zero-range processes: statics and dynamics. In *Ageing and the Glass Transition*, pages 261–294. Springer, 2007.

2 citation(s) on 2 page(s): 12 and 17,

[28] MR Evans, Satya N Majumdar, and RKP Zia. Canonical analysis of condensation in factorised steady states. *Journal of statistical physics*, 123(2):357–390, 2006.
2 citation(s) on 2 page(s): 12 and 22,

[29] Christiane Cocozza-Thivent. Processus des misanthropes. *Zeitschrift für Wahrscheinlichkeitstheorie und verwandte Gebiete*, 70(4):509–523, 1985.
1 citation(s) on 1 page(s): 12,

[30] JM Luck and C Godrèche. Structure of the stationary state of the asymmetric target process. *Journal of Statistical Mechanics: Theory and Experiment*, 2007(08):P08005, 2007.
1 citation(s) on 1 page(s): 12,

[31] Enrique Daniel Andjel. Invariant measures for the zero range process. *The Annals of Probability*, pages 525–547, 1982.
3 citation(s) on 2 page(s): 13 (2) and 15,

[32] Claude Kipnis and Claudio Landim. *Scaling limits of interacting particle systems*, volume 320. Springer, 1999.
1 citation(s) on 1 page(s): 13,

[33] Stefan Grosskinsky, Frank Redig, and Kiamars Vafayi. Condensation in the inclusion process and related models. *Journal of Statistical Physics*, 142(5):952–974, 2011.
5 citation(s) on 4 page(s): 13, 17 (2), 18, and 19,

[34] Ed Waymire. Zero-range interaction at bose-einstein speeds under a positive recurrent single particle law. *The Annals of Probability*, pages 441–450, 1980.
1 citation(s) on 1 page(s): 13,

[35] Paul Chleboun and Stefan Grosskinsky. Finite size effects and metastability in zero-range condensation. *Journal of Statistical Physics*, 140(5):846–872, 2010.
1 citation(s) on 1 page(s): 13,

[36] MR Evans. Phase transitions in one-dimensional nonequilibrium systems. *Brazilian Journal of Physics*, 30(1):42–57, 2000.
6 citation(s) on 5 page(s): 13, 15 (2), 17, 23, and 43,

[37] Sang-Woo Kim, Joongul Lee, and Jae Dong Noh. Particle condensation in pair exclusion process. *Physical Review E*, 81(5):051120, 2010.
1 citation(s) on 1 page(s): 13,

[38] Yonathan Schwarzkopf, MR Evans, and David Mukamel. Zero-range processes with multiple condensates: statics and dynamics. *Journal of Physics A: Mathematical and Theoretical*, 41(20):205001, 2008.
1 citation(s) on 1 page(s): 13,

[39] AG Thompson, J Tailleur, ME Cates, and RA Blythe. Zero-range processes with saturated condensation: the steady state and dynamics. *Journal of Statistical Mechanics: Theory and Experiment*, 2010(02):P02013, 2010.
1 citation(s) on 1 page(s): 13,

[40] Ori Hirschberg, David Mukamel, and Gunter M Schütz. Condensation in temporally correlated zero-range dynamics. *Physical review letters*, 103(9):090602, 2009.
1 citation(s) on 1 page(s): 13,

[41] JMJ Van Leeuwen and A Kooiman. The drift velocity in the rubinsteinâduke model for electrophoresis. *Physica A: Statistical Mechanics and its Applications*, 184(1):79–97, 1992.
1 citation(s) on 1 page(s): 13,

[42] JM Carlson, ER Grannan, and GH Swindle. Self-organizing systems at finite driving rates. *Physical Review E*, 47(1):93, 1993.
1 citation(s) on 1 page(s): 13,

[43] Felix Ritort. Glassiness in a model without energy barriers. *Physical review letters*, 75(6):1190, 1995.
1 citation(s) on 1 page(s): 13,

[44] Kamal K Bardhan, Bikas K Chakrabarti, and Alex Hansen. Non-linearity and breakdown in soft condensed matter. In *Non-linearity and Breakdown in Soft Condensed Matter*, volume 437, 1994.
1 citation(s) on 1 page(s): 14,

[45] Joachim Krug and Martin Schimschak. Metastability of step flow growth in 1+ 1 dimensions. *Journal de Physique I*, 5(8):1065–1086, 1995.
1 citation(s) on 1 page(s): 14,

[46] Vladimir Privman. *Nonequilibrium statistical mechanics in one dimension*. Cambridge University Press, 2005.
1 citation(s) on 1 page(s): 14,

[47] R Kutner, KW Kehr, W Renz, and R Przenioslo. Diffusion in a one-dimensional bosonic lattice gas. *Journal of Physics A: Mathematical and General*, 28(4):923, 1995.
2 citation(s) on 1 page(s): 14 (2),

[48] C Godreche. Dynamics of condensation in zero-range processes. *Journal of Physics A: Mathematical and General*, 36(23):6313, 2003.
3 citation(s) on 3 page(s): 15, 17, and 43,

[49] C Godreche and JM Luck. Dynamics of the condensate in zero-range processes. *Journal of Physics A: Mathematical and General*, 38(33):7215, 2005.
3 citation(s) on 3 page(s): 15, 17, and 43,

[50] Cristian Giardina, Jorge Kurchan, and Frank Redig. Duality and exact correlations for a model of heat conduction. *Journal of mathematical physics*, 48(3):033301, 2007.
3 citation(s) on 2 page(s): 17 (2) and 18,

[51] Cristian Giardiná, Jorge Kurchan, Frank Redig, and Kiamars Vafayi. Duality and hidden symmetries in interacting particle systems. *Journal of Statistical Physics*, 135(1):25–55, 2009.
4 citation(s) on 3 page(s): 17 (2), 18, and 22,

[52] C. Giardiná, F. Redig, and K. Vafayi. Correlation inequalities for interacting particle systems with duality. *Journal of Statistical Physics*, 141(2):242–263, 2010.
2 citation(s) on 1 page(s): 17 (2),

[53] Shlomi Reuveni, Iddo Eliazar, and Uri Yechiali. Asymmetric inclusion process as a showcase of complexity. *Phys. Rev. Lett.*, 109:020603, Jul 2012.
1 citation(s) on 1 page(s): 17,

[54] Jiarui Cao, Paul Chleboun, and Stefan Grosskinsky. Dynamics of condensation in the totally asymmetric inclusion process. *Journal of Statistical Physics*, 155(3):523–543, 2014.
9 citation(s) on 9 page(s): 17, 32, 44, 66, 90, 92, 107, 109, and 115,

[55] C Godreche and JM Luck. Nonequilibrium dynamics of the zeta urn model. *The European Physical Journal B-Condensed Matter and Complex Systems*, 23(4):473–486, 2001.
1 citation(s) on 1 page(s): 17,

[56] Luca Ferretti and Ginestra Bianconi. Dynamics of condensation in growing complex networks. *Physical Review E*, 78(5):056102, 2008.

1 citation(s) on 1 page(s): 17,

[57] Stefan Grosskinsky, Frank Redig, and Kiamars Vafayi. Dynamics of condensation in the symmetric inclusion process. *Electron. J. Probab*, 18(66):1–23, 2013.
3 citation(s) on 3 page(s): 17, 32, and 90,

[58] Paul Chleboun. *Large Deviations and Metastability in Condensing Stochastic Particle Systems*. PhD thesis, University of Warwick, October 2011.
1 citation(s) on 1 page(s): 19,

[59] M R Evans and B Waclaw. Condensation in stochastic mass transport models: beyond the zero-range process. *Journal of Physics A: Mathematical and Theoretical*, 47(9):095001, 2014.
14 citation(s) on 11 page(s): 20 (3), 23, 30, 43, 44, 52, 58, 90 (2), 95, 96, and 121,

[60] MR Evans, SN Majumdar, I Pagonabarraga, and E Trizac. Condensation transition in polydisperse hard rods. *THE JOURNAL OF CHEMICAL PHYSICS*, 132:014102, 2010.
1 citation(s) on 1 page(s): 22,

[61] Paul L Krapivsky, Sidney Redner, and Francois Leyvraz. Connectivity of growing random networks. *Physical review letters*, 85(21):4629, 2000.
1 citation(s) on 1 page(s): 22,

[62] Piotr Bialas and Zdzislaw Burda. Collapse of 4d random geometries. *Physics Letters B*, 416(3):281–285, 1998.
1 citation(s) on 1 page(s): 22,

[63] Zdzislaw Burda, D Johnston, Jerzy Jurkiewicz, M Kamiński, Maciej A Nowak, Gabor Papp, and Ismail Zahed. Wealth condensation in pareto macroeconomies. *Physical Review E*, 65(2):026102, 2002.
1 citation(s) on 1 page(s): 22,

[64] T Hanney. Factorized steady states for multi-species mass transfer models. *Journal of Statistical Mechanics: Theory and Experiment*, 2006(12):P12006, 2006.
1 citation(s) on 1 page(s): 22,

[65] MR Evans. Bose-einstein condensation in disordered exclusion models and relation to traffic flow. *EPL (Europhysics Letters)*, 36(1):13, 1996.
1 citation(s) on 1 page(s): 23,

[66] Joachim Krug and Pablo A Ferrari. Phase transitions in driven diffusive systems with random rates. *Journal of Physics A: Mathematical and General*, 29(18):L465, 1996.
1 citation(s) on 1 page(s): 23,

[67] C Landim. Hydrodynamical limit for space inhomogeneous one-dimensional totally asymmetric zero-range processes. *The Annals of Probability*, pages 599–638, 1996.
2 citation(s) on 1 page(s): 23 (2),

[68] I Benjamini, PA Ferrari, and C Landim. Asymmetric conservative processes with random rates. *Stochastic processes and their applications*, 61(2):181–204, 1996.
2 citation(s) on 1 page(s): 23 (2),

[69] JM Drouffe, C Godreche, and F Camia. A simple stochastic model for the dynamics of condensation. *Journal of Physics A: Mathematical and General*, 31(1):L19, 1998.
2 citation(s) on 2 page(s): 23 and 90,

[70] Enrique D Andjel, Pablo A Ferrari, Herve Guiol, et al. Convergence to the maximal invariant measure for a zero-range process with random rates. *Stochastic processes and their applications*, 90(1):67–81, 2000.
1 citation(s) on 1 page(s): 23,

[71] Paul Erdos and Alfred Rényi. On the evolution of random graphs. *Bull. Inst. Internat. Statist*, 38(4):343–347, 1961.
1 citation(s) on 1 page(s): 34,

[72] G. Grimmett and D. Stirzaker. *Probability and Random Processes*. Probability and Random Processes. OUP Oxford, 2001.
1 citation(s) on 1 page(s): 67,

[73] OJ Oâloan, MR Evans, and ME Cates. Jamming transition in a homogeneous one-dimensional system: The bus route model. *Physical Review E*, 58(2):1404, 1998.
1 citation(s) on 1 page(s): 90,

[74] C Godrèche and JM Luck. Condensation in the inhomogeneous zero-range process: an interplay between interaction and diffusion disorder. *Journal of Statistical Mechanics: Theory and Experiment*, 2012(12):P12013, 2012.
1 citation(s) on 1 page(s): 90,

[75] Daniel T Gillespie. Exact stochastic simulation of coupled chemical reactions. *The Journal of Physical Chemistry*, 81(25):2340–2361, 1977.
3 citation(s) on 3 page(s): 92, 93, and 116,

[76] Daniel T Gillespie. Stochastic simulation of chemical kinetics. *Annu. Rev. Phys. Chem.*, 58:35–55, 2007.
1 citation(s) on 1 page(s): 92,

[77] Mutsuo Saito and Makoto Matsumoto. Simd-oriented fast mersenne twister: a 128-bit pseudorandom number generator. In *Monte Carlo and Quasi-Monte Carlo Methods 2006*, pages 607–622. Springer, 2008.
1 citation(s) on 1 page(s): 92,

[78] Makoto Matsumoto and Takuji Nishimura. Mersenne twister: a 623-dimensionally equidistributed uniform pseudo-random number generator. *ACM Transactions on Modeling and Computer Simulation (TOMACS)*, 8(1):3–30, 1998.
1 citation(s) on 1 page(s): 92,

[79] Alfred B Bortz, Malvin H Kalos, and Joel L Lebowitz. A new algorithm for monte carlo simulation of ising spin systems. *Journal of Computational Physics*, 17(1):10–18, 1975.
1 citation(s) on 1 page(s): 93,